Effect of Combined Nanoparticle and Polymeric Dispersions on Critical Heat Flux, Nucleate Boiling Heat Transfer Coefficient, and Coating Adhesion

By

Bronwyn K. Edwards

Submitted to the Department of Nuclear Science and Engineering in Partial Fulfillment of the Requirements for the Degrees of Bachelor of Science in Nuclear Science and Engineering and Master of Science in Nuclear Science and Engineering

at the

Massachusetts Institute of Technology

June 2009

Signature of Author_____
Bronwyn K. Edwards
Department of Nuclear Science and Engineering
8 May 2009

Certified by_____
Lin-wen Hu
Associate Director, Nuclear Reactor Laboratory
Thesis Supervisor

Certified by_____
Jacopo Buongiorno
Associate Professor of Nuclear Science and Engineering
Thesis Co-Supervisor

Certified by_____
Thomas McKrell
Research Scientist, Department of Nuclear Science and Engineering
Thesis Reader

Accepted by_____
Jacquelyn C. Yanch
Professor of Nuclear Science and Engineering
Chair, Department Committee on Graduate Students

Effect of Combined Nanoparticle and Polymeric Dispersions on Critical Heat Flux, Nucleate Boiling Heat Transfer Coefficient, and Coating Adhesion

by

Bronwyn K. Edwards

Submitted to the Department of Nuclear Science and Engineering
on May 8, 2009 in partial fulfillment of the requirements for the
Degrees of Bachelor of Science in Nuclear Science and
Engineering and Master of Science in Nuclear Science and
Engineering

Abstract

An experimental study was performed to determine thermal performance and adhesion effects of a combined nanoparticle and polymeric dispersion coating. The critical heat flux (CHF) values and nucleate boiling heat transfer coefficients (HTC) of nickel wires pre-coated using 1.0% alumina, 0.1% alumina, 500ppm polyallylamine hydrochloride (PAH), and 0.1% alumina combined with 500ppm PAH dispersions were determined using the pool-boiling method. The adhesion of 0.1% alumina and combined 0.1% alumina and 500ppm PAH coatings was evaluated using the tape and modified bend test methods.

Results of the pool boiling experiments showed that the wire heaters pre-coated with combined 0.1% alumina and 500ppm PAH dispersion increase the CHF in water by ~40% compared to bare wire heaters, compared to an enhancement of ~37% with a 0.1% alumina coating. The combined 0.1% alumina and 500ppm PAH dispersion degrades the wire HTC by less than 1%, compared to a degradation of over 26% with a 0.1% alumina coating. Results from the tape test indicate qualitatively that the combined 0.1% alumina and 500ppm PAH dispersion coating adheres better than the 0.1% alumina nanoparticle coating. Results from the modified bend test showed that the combined 0.1% alumina and 500ppm PAH dispersion coating did not fail at the failure strain of the 0.1% alumina nanoparticle coating (8.108×10^{-4}).

The addition of PAH to alumina nanofluid for creating a nanoparticle coating through boiling deposition was found to improve both coating thermal performance and adhesion over the pure alumina nanofluid.

Thesis Supervisor: Lin-wen Hu
Title: Associate Director, Nuclear Reactor Laboratory
Thesis Co-Supervisor: Jacopo Buongiorno
Title: Associate Professor of Nuclear Science and Engineering
Thesis Reader: Thomas McKrell
Title: Research Scientist, Department of Nuclear Science and Engineering

Acknowledgements

I would especially like to thank my supervisor, Dr. Lin-wen Hu, co-supervisor, Professor Jacopo Buongiorno, reader, Dr. Thomas McKrell, and mentor, Bao Truong, for their continual support. My thanks also go to the Nanofluids Research Group, especially Eric Forrest, for their advice, encouragement, and vast stores of knowledge.

This work is dedicated to my fiancé, Zachary Clifford, and especially to my parents, Andrew and Cherrie Edwards.

Table of Contents

Abstract 2

Acknowledgements 3

Table of Contents 4

Table of Figures 6

List of Tables 10

1 Introduction 11
- **1.1 Previous Work** 11
- **1.2 Thesis Objective** 16
  - 1.2.1 Thesis Statement 16
  - 1.2.2 Pool-boiling Experiments 17
  - 1.2.3 Adhesion Testing 20

2 Deionized Water and Alumina Nanofluid Experiments 26
- **2.1 Deionized Water Boiling HTC and CHF Baseline** 26
  - 2.1.1 Experimental Procedure 26
  - 2.1.2 Results 26
  - 2.1.3 Analysis 29
- **2.2 Effects of Alumina Nanoparticle Coating on Boiling HTC and CHF** 32
  - 2.2.1 Experimental Procedure 32
  - 2.2.2 Results 33
  - 2.2.3 Analysis 41

3 Alumina + PAH Experiments 51
- **3.1 Alumina and PAH Mixture Interactions** 51
  - 3.1.1 Experimental Procedure 51
  - 3.1.2 Results 52
- **3.2 Effects of Alumina Nanoparticles and PAH Coating on Boiling HTC and CHF** 53
  - 3.2.1 Experimental Procedure 54
  - 3.2.2 Results 54
  - 3.2.3 Analysis 60
- **3.3 Effects of PAH Coating on Boiling HTC and CHF** 64
  - 3.3.1 Experimental Procedure 64
  - 3.3.2 Results 65
  - 3.3.3 Analysis 70

4 Comparison of Alumina, PAH, and Alumina + PAH Coating Heat Transfer Performance 75

5 Adhesion Tests 78
- 5.1 Experimental Procedure 78
- 5.2 Results 82
- 5.3 Analysis 95

6 Conclusions 100

Appendix A- Error Analysis and Propagation 102
- **A.1 - Experimental (Instrumentation) Error** 102

A.2 - Error Propagation **104**
A.3 - Statistical Uncertainty **107**
Appendix B- CHF and HTC Test Results **108**
7 References **123**

Table of Figures

Figure 1: Schematic of a typical pool-boiling curve. 12
Figure 2: Basic representation of the contact angle at the liquid-surface interface (adapted from Ref. [1]). 14
Figure 3: Experimental setup for pool-boiling facility. 17
Figure 4: Simplified tape test (adapted from Ref. [14]). 21
Figure 5: Three-point bending (left) and tensile (right) tests (adapted from Ref. [11]). 22
Figure 6: Laser shock adhesion test (adapted from Ref. [14]). 23
Figure 7: Modified bend test. 24
Figure 8: Boiling curve for bare nickel wire in deionized water, 02/02 test 1. CHF occurred at 1.079 MW/m^2. 27
Figure 9: Boiling curve for bare nickel wire in deionized water, 02/02 test 2. CHF occurred at 0.906 MW/m^2. 28
Figure 10: Boiling curve for bare nickel wire in deionized water, 02/02 test 3. CHF occurred at 1.153 MW/m^2. 28
Figure 11: Boiling curves for bare nickel wire in deionized water. 29
Figure 12: Heat transfer coefficients versus heat flux for bare nickel wire in deionized water. The average HTC stops at the lowest CHF point of the curves used to generate the average. 31
Figure 13: Boiling curve for 1.0% alumina-pre-coated nickel wire in deionized water, 11/18 test 1. CHF occurred at 1.271 MW/m^2. 34
Figure 14: Boiling curve for 1.0% alumina-pre-coated nickel wire in deionized water, 01/05 test 1. CHF occurred at 1.242 MW/m^2. 34
Figure 15: Boiling curve for 1.0% alumina-pre-coated nickel wire in deionized water, 01/06 test 1. CHF occurred at 1.229 MW/m^2. 35
Figure 16: Boiling curve for 1.0% alumina-pre-coated nickel wire in deionized water, 02/03 test 1. CHF occurred at 2.115 MW/m^2. 36
Figure 17: Boiling curve for 0.1% alumina-pre-coated nickel wire in deionized water, 02/05 test 1. CHF occurred at 1.552 MW/m^2. 36
Figure 18: Boiling curve for 0.1% alumina-pre-coated nickel wire in deionized water, 02/06 test 1. CHF occurred at 1.142 MW/m^2. 37
Figure 19: Boiling curve for 0.1% alumina-pre-coated nickel wire in deionized water, 02/06 test 2. CHF occurred at 1.469 MW/m^2. 38
Figure 20: Boiling curve for 0.1% alumina-pre-coated nickel wire in deionized water, 02/09 test 1. CHF occurred at 1.516 MW/m^2. 38
Figure 21: Boiling curve for 0.1% alumina-pre-coated nickel wire in deionized water, 02/10 test 1. CHF occurred at 1.280 MW/m^2. 39
Figure 22: Boiling curve for 0.1% alumina-pre-coated nickel wire in deionized water, 02/11 test 1. CHF occurred at 1.685 MW/m^2. 40
Figure 23: Boiling curve for 0.1% alumina-pre-coated nickel wire in deionized water, 02/13 test 1. CHF occurred at 1.362 MW/m^2. 40
Figure 24: Boiling curves for 1.0% alumina-pre-coated nickel wire in deionized water. 41
Figure 25: Heat transfer coefficients versus heat flux for 1.0% alumina-pre-coated nickel wire in deionized water. Please note that only 2 tests were included in the HTC analysis as explained in Appendix B.2. 43
Figure 26: Ratio of 1.0% alumina-pre-coated nickel wire heat transfer coefficients to the average bare wire heat transfer coefficients. 44
Figure 27: 1.0% alumina-pre-coated wire surface morphology and material composition. Clockwise from top left: 250x, 1000x, 5000x, and EDS data taken after 5000x SEM. 45
Figure 28: Boiling curves for 0.1% alumina-pre-coated nickel wire in deionized water. 46
Figure 29: Heat transfer coefficients versus heat flux for 0.1% alumina-pre-coated nickel wire in deionized water. 47
Figure 30: Ratio of 0.1% alumina-pre-coated nickel wire heat transfer coefficients to the average bare wire heat transfer coefficients. 48
Figure 31: 1.0% alumina-pre-coated wire surface morphology and material composition. Clockwise from top left: 250x, 1000x, 5000x, and EDS data taken after 5000x SEM. 49

Figure 32: Heat transfer coefficient ratio to bare wire for 1.0% and 0.1% alumina nanofluid concentrations. 50
Figure 33: SEM images of 1.0% (left) and 0.1% (right) alumina-pre-coated nickel wires. 50
Figure 34: Alumina and PAH mixtures 3 months after initial preparation. As can be seen, no agglomeration, settling, or discoloration has occurred in these samples. 53
Figure 35: Boiling curve for alumina + PAH-pre-coated nickel wire in deionized water, 01/07 test 1. CHF occurred at 1.634 MW/m^2. 55
Figure 36: Boiling curve for alumina + PAH-pre-coated nickel wire in deionized water, 01/08 test 1. CHF occurred at 1.405 MW/m^2. 56
Figure 37: Boiling curve for alumina + PAH-pre-coated nickel wire in deionized water, 01/08 test 2. CHF occurred at 1.404 MW/m^2. 57
Figure 38: Boiling curve for alumina + PAH-pre-coated nickel wire in deionized water, 01/09 test 1. CHF occurred at 1.619 MW/m^2. 58
Figure 39: Boiling curve for alumina + PAH-pre-coated nickel wire in deionized water, 01/12 test 1. CHF occurred at 1.359 MW/m^2. 59
Figure 40: Boiling curve for alumina + PAH-pre-coated nickel wire in deionized water, 01/14 test 1. CHF occurred at 1.310 MW/m^2. 59
Figure 41: Boiling curves for alumina + PAH-pre-coated nickel wire in deionized water. 60
Figure 42: Heat transfer coefficients versus heat flux for alumina + PAH-pre-coated nickel wire in deionized water. 62
Figure 43: Ratio of alumina + PAH-pre-coated nickel wire heat transfer coefficients to the average bare wire heat transfer coefficients. 63
Figure 44: Alumina + PAH-pre-coated wire surface morphology and material composition. Clockwise from top left: 250x, 1000x, 5000x, and EDS data taken after 1000x SEM. 64
Figure 45: Boiling curve for PAH-pre-coated nickel wire in deionized water, 01/20 test 1. CHF occurred at 0.980 MW/m^2. 66
Figure 46: Boiling curve for PAH-pre-coated nickel wire in deionized water, 01/22 test 1. CHF occurred at 0.967 MW/m^2. 66
Figure 47: Boiling curve for PAH-pre-coated nickel wire in deionized water, 01/22 test 2. CHF occurred at 1.109 MW/m^2. 67
Figure 48: Boiling curve for PAH-pre-coated nickel wire in deionized water, 01/23 test 1. CHF occurred at 1.242 MW/m^2. 68
Figure 49: Boiling curve for PAH-pre-coated nickel wire in deionized water, 02/19 test 1. CHF occurred at 1.254 MW/m^2. 68
Figure 50: Boiling curve for PAH-pre-coated nickel wire in deionized water, 02/24 test 1. CHF occurred at 1.263 MW/m^2. 69
Figure 51: Boiling curve for PAH-pre-coated nickel wire in deionized water, 03/03 test 1. CHF occurred at 0.846 MW/m^2. 69
Figure 52: Boiling curve for PAH-pre-coated nickel wire in deionized water, 03/03 test 2. CHF occurred at 1.030 MW/m^2. 70
Figure 53: Boiling curves for PAH-pre-coated nickel wire in deionized water. 71
Figure 54: Heat transfer coefficients versus heat flux for PAH-pre-coated nickel wire in deionized water. 72
Figure 55: Ratio of PAH-pre-coated nickel wire heat transfer coefficients to the average bare wire heat transfer coefficients. 73
Figure 56: 500ppm PAH-pre-coated wire surface morphology and material composition. Clockwise from top left: 250x, 1000x, 5000x, and EDS data taken after 5000x SEM. The EDS indicates the wire is not completely coated with PAH. 74
Figure 57: Average heat transfer coefficients for bare and coated wires. 76
Figure 58: Average heat transfer coefficient ratios to bare wire for various coatings. The red line indicates a ratio of one to the bare wire HTC. 77
Figure 59: SEM image of 0.1% alumina pre-coated nickel wire at 250x. 81
Figure 60: SEM image of alumina + PAH pre-coated nickel wire at 250x. 82
Figure 61: 0.1% alumina-pre-coated wire surface morphology after preliminary tape test. These figures show two different regions of the 0.1% alumina-pre-coated wire at 100x magnification. 83

Figure 62: Alumina + PAH-pre-coated wire surface morphology after preliminary tape test. These figures show two different regions of the alumina + PAH-pre-coated wire at 100x magnification. **83**
Figure 63: 500ppm PAH-pre-coated wire surface morphology after preliminary tape test. **84**
Figure 64: 0.1% alumina-pre-coated wire surface morphology after final tape test. These figures show the same region of the 0.1% alumina-pre-coated wire at 100x (left) and 250x (right) magnifications. **85**
Figure 65: Alumina + PAH-pre-coated wire surface morphology after final tape test. These figures show the same region of the alumina + PAH-pre-coated wire at 100x (left) and 250x (right) magnifications. **86**
Figure 66: Alumina + PAH-pre-coated wire surface morphology after final tape test. These figures show the same region of the alumina + PAH-pre-coated wire at 100x (left) and 250x (right) magnifications. **86**
Figure 67: 0.1% alumina-pre-coated wire surface morphology after 3 1/2" rod diameter bend test. These figures show regions of the 0.1% alumina-pre-coated wire at (clockwise from upper left): 100x, 250x, 250x, and 250x magnifications. **87**
Figure 68: 0.1% alumina-pre-coated wire surface morphology after 10 11/32" rod diameter bend test. These figures show the same region of the 0.1% alumina-pre-coated wire at 100x (left) and 250x (right) magnifications. Note that a visible amount of coating has fallen onto the mounting tape. **88**
Figure 69: 0.1% alumina-pre-coated wire surface morphology after 10 11/32" rod diameter bend test. These figures show the same region of the 0.1% alumina-pre-coated wire at 100x (left) and 250x (right) magnifications. Note that a visible amount of coating has fallen onto the mounting tape. **88**
Figure 70: 0.1% alumina-pre-coated wire surface morphology after 11 11/32" rod diameter bend test. These figures show the same region of the 0.1% alumina-pre-coated wire at 100x (left) and 250x (right) magnifications. **89**
Figure 71: 0.1% alumina-pre-coated wire surface morphology after 11 11/32" rod diameter bend test. These figures show the same region of the 0.1% alumina-pre-coated wire at 100x (left) and 250x (right) magnifications. **89**
Figure 72: 0.1% alumina-pre-coated wire (4/2) surface morphology after 10 11/32" rod diameter bend test. These figures show the same region of the 0.1% alumina-pre-coated wire at 100x (left) and 250x (right) magnifications. **90**
Figure 73: 0.1% alumina-pre-coated wire (4/2) surface morphology after 10 11/32" rod diameter bend test. These figures show the same region of the 0.1% alumina-pre-coated wire at 100x (left) and 250x (right) magnifications. **90**
Figure 74: 0.1% alumina-pre-coated wire (3/31) surface morphology after 10 11/32" rod diameter bend test. These figures show the same region of the 0.1% alumina-pre-coated wire at 100x (left) and 250x (right) magnifications. **91**
Figure 75: 0.1% alumina-pre-coated wire (3/31) surface morphology after 10 11/32" rod diameter bend test. These figures show the same region of the 0.1% alumina-pre-coated wire at 100x (left) and 250x (right) magnifications. **91**
Figure 76: Alumina and PAH-pre-coated wire (3/19) surface morphology after 10 11/32" rod diameter bend test. These figures show the same region of the alumina + PAH-pre-coated wire at 100x (left) and 250x (right) magnifications. The striated lines are due to the wire orientation. **92**
Figure 77: Alumina and PAH-pre-coated wire (4/2) surface morphology after 10 11/32" rod diameter bend test. These figures show the same region of the alumina + PAH-pre-coated wire at 100x (left) and 250x (right) magnifications. **92**
Figure 78: 0.1% alumina-pre-coated wire (3/31) surface morphology after 11 11/32" rod diameter bend test. These figures show the same region of the 0.1% alumina-pre-coated wire at 100x (left) and 250x (right) magnifications. **93**
Figure 79: 0.1% alumina-pre-coated wire (3/31) surface morphology after 11 11/32" rod diameter bend test. These figures show the same region of the 0.1% alumina-pre-coated wire at 100x (left) and 250x (right) magnifications. **93**
Figure 80: 0.1% alumina-pre-coated wire (4/2) surface morphology after 11 11/32" rod diameter bend test. These figures show the same region of the 0.1% alumina-pre-coated wire at 100x (left) and 250x (right) magnifications. **94**
Figure 81: 0.1% alumina-pre-coated wire (4/2) surface morphology after 11 11/32" rod diameter bend test. These figures show the same region of the 0.1% alumina-pre-coated wire at 100x (left) and 250x (right) magnifications. **94**

Figure 82: Alumina and PAH-pre-coated wire (3/19) surface morphology after 11 11/32" rod diameter bend test. These figures show the same region of the alumina + PAH-pre-coated wire at 100x (left) and 250x (right) magnifications. **95**
Figure 83: Alumina and PAH-pre-coated wire (4/2) surface morphology after 11 11/32" rod diameter bend test. These figures show the same region of the alumina + PAH-pre-coated wire at 100x (left) and 250x (right) magnifications. **95**

List of Tables

Table 1: CHF values for bare nickel wire in deionized water. **29**
Table 2: Alumina nanofluid composition. **32**
Table 3: Silica nanofluid composition (using Sigma-Aldrich LUDOX TMA colloidal silica, 34wt.% in deionized water). **32**
Table 4: CHF values for 1.0% alumina-pre-coated nickel wire in deionized water. **42**
Table 5: CHF values for 0.1% alumina-pre-coated nickel wire in deionized water. **46**
Table 6: PAH fluid composition. **51**
Table 7: Alumina and PAH mixture compositions. **51**
Table 8: Alumina + PAH mixture compositions and observations. **52**
Table 9: Alumina + PAH mixture concentrations and CHF data. **61**
Table 10: CHF values for alumina + PAH-pre-coated wire in deionized water. **61**
Table 11: PAH nanofluid composition. **65**
Table 12: CHF values for PAH-pre-coated wire in deionized water. **71**
Table 13: Average CHF values and CHF ratio to bare wire for various coatings. **75**
Table 14: Average HTC ratios of various coatings to bare wire. **77**
Table 15: Mechanical properties for alumina and annealed nickel [31]. **79**
Table 16: Strain and stress on alumina corresponding to rod radii used in bend tests. **81**

1 Introduction

Nanofluids are colloids containing nanoparticles of various materials, such as metal oxides, metals, graphite, and have been investigated to address some of the limitations on heat transfer performance, most notably the critical heat flux (CHF). CHF is defined as the point at which a poorly conducting vapor blanket deteriorates boiling heat transfer from a heated surface to coolant. This poor heat transfer causes overheating, which ultimately damages the heated surface (for example, a wire can break at CHF). Nanofluids have been found to enhance CHF through deposition of nanoparticles on the surface, which can potentially improve thermal performance of energy systems.

While most experimental research agrees that nanofluids enhance CHF performance, previous studies have been unable to reach a consensus about what effect nanoparticle deposition has on the nucleate boiling heat transfer coefficient (HTC). The onset of nucleate boiling is defined as the point at which bubbles form on the heated surface. These bubbles eventually separate from the surface, allowing more coolant to come into contact with the surface. Nucleate boiling is a very effective heat transfer mode up to the CHF point. Both CHF and HTC have been closely linked to characteristics of the heated surface.

Adhesion of the nanoparticles to a surface is also a concern in thermal performance. If a nanoparticle coating can easily be removed from a surface by flow-induced erosion, for example, the corresponding CHF enhancement is also removed. For long-term thermal performance enhancement, the nanoparticle coating must be resilient to erosion.

1.1 Previous Work

As mentioned above, CHF is defined as the heat flux at which a material fails by fracturing. CHF occurs at the peak between nucleate boiling and transition boiling as depicted in the qualitative boiling curve in Figure 1. The boiling curve illustrates the relationship between

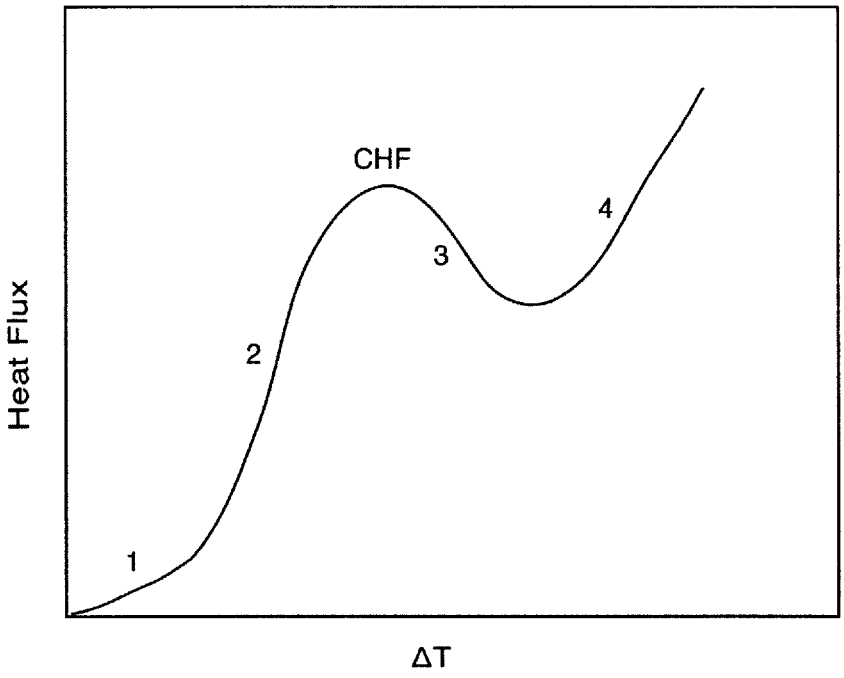

Figure 1: Schematic of a typical pool-boiling curve.

the heat flux through a wire heater, q″ (MW/m^2), and the difference between the wire heater temperature, T_w (°C or K), and saturation temperature for water, T_{sat} (°C or K, e.g. 100°C at atmospheric pressure), which is defined as the wall superheat, or ΔT (°C or K). There are four distinct regions on the pool-boiling curve: natural or free convection, nucleate boiling, transition boiling, and film boiling. These regions are labeled as 1, 2, 3, and 4 respectively in Figure 1. During nucleate boiling, bubbles at first leave the heated surface discretely and leave in columns or jets at higher wall superheat. As the wall superheat increases beyond CHF, the bubble jets merge and form a vapor layer, resulting in film boiling. Transition boiling is only observed in experiments with ΔT as the controlled variable. In experiments with q″ controlled, the boiling regime transitions directly from nucleate to film boiling.

A correlation commonly used to predict pool boiling CHF is based on the hydrodynamic instability theory:

$$q''_{CHF} = C \cdot h_{fg} \cdot \left(\frac{\sigma \cdot [\rho_f - \rho_g] \cdot g}{\rho_g^2} \right)^{1/4} \quad (1)$$

where h_{fg} is latent heat of vaporization (J/kg), σ is the fluid surface tension (Nm), ρ_f is the fluid density (kg/m^3), ρ_g is the vapor density (kg/m^3), and g is gravitational acceleration (m/s^2). C is an empirical constant that is dependent on heater geometry. C has been estimated using theories developed by Zuber, Kutateladze, and Lienhard and is typically around 0.15 [12,13].

The heat transfer coefficient of a fluid is a measurement of the heat (energy) removal rate from a surface under certain conditions. The heat transfer coefficient of a particular surface-fluid pair can be found from the slope of a region on the boiling curve, since Newton's law of cooling states that

$$q'' = h \cdot (T_W - T_{sat}) \quad (2)$$

with T_w equal to the surface temperature (K), T_f equal to the fluid temperature at a given pressure (K), and h equal to the heat transfer coefficient in that region (W/m^2-K) [12, 13].

The effect of nanoparticle depositions on CHF has been well documented by several research groups [1, 2, 3, 4, 5]. Previous research has found that nanofluids improve CHF performance by altering surface characteristics [1, 3, 4, 5]. In particular, nanoparticle deposition increases the surface roughness and reduces the surface energy, which in turn increases surface wettability. Increased surface wettability was found to enhance CHF due to better rewetting of the heated surface. The mechanism for increased surface wettability has been well documented [1, 4, 6, 7] and can be determined by the liquid-surface contact angle, illustrated in Figure 2. The apparent contact angle, θ (degrees or radians), depends on the surface roughness factor, γ, as

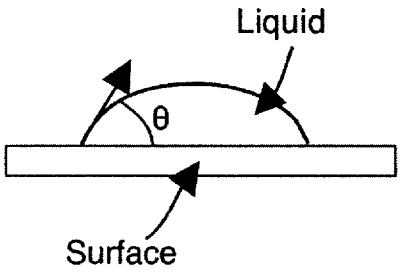

Figure 2: Basic representation of the contact angle at the liquid-surface interface (adapted from Ref. [1]).

described in the modified Young's equation [1, 5]. In Young's equation, the contact angle depends on the surface tension, adhesion tension, and surface roughness with the following relationship:

$$\cos(\theta) = r\frac{\gamma_{SV} - \gamma_{SL}}{\sigma} \tag{3}$$

where r is the roughness factor, γ_{sv} is the surface free energy between the solid and vapor (J/m^2), and γ_{sl} is the surface free energy between the solid and liquid (J/m^2) [1, 5]. The difference between γ_{sv} and γ_{sl} is defined as the adhesion tension. As γ_{sv}-γ_{sl} and/or r increase, θ decreases and the liquid droplet wettability increases. As mentioned previously, nanoparticle depositions affect both the adhesion tension and roughness factor of the heated surface and allow for increased wettability. It has been well established that increased wettability due to nanoparticle deposition is responsible for increased CHF performance. Another correlation, based on the hot/ dry spot theory, relates the contact angle to CHF in the following way:

$$q''_{cr} = \left(1 - \frac{\sin\theta}{2} - \frac{\pi/2 - \theta}{2\cos\theta}\right)^{1/4} \rho_g h_{fg} \left[\frac{\sigma(\rho_f - \rho_g)g}{\rho_g^2}\right]^{1/4}, \tag{4}$$

with h_{fg} equal to the latent heat of vaporization (J/kg), σ equal to the fluid surface tension (Nm), ρ_f equal to the fluid density (kg/m^3), ρ_g equal to the vapor density (kg/m^3), and g equal to gravity (m/s^2) [5]. As expected, a decrease in the contact angle results in an overall increase of the CHF.

Porous coatings have also been found to enhance CHF [32, 33]. Several mechanisms for this enhancement have been proposed, including: altered surface characteristics, hydrodynamic instabilities, and surface and particle geometries [32]. Porous coatings reduce the surface-liquid contact angle and allow for improved surface wettability because the surface arteries and pores trap liquid, making the surface hydrophilic [33]. Porous coatings also have a higher nucleation site density resulting in more, but smaller, bubble columns [32, 33]. Chen theorized that, due to the increased number of vapor columns appearing on a porous surface, higher vapor velocity is needed to maintain Helmholtz stability (and avoid vapor column collapse) [32]. The size of the pores on the surface offers a trade-off between capillary force and fluid flow since smaller pores allow for a higher capillary force but decrease fluid flow [32, 33]. Similarly, the coating thickness offers a trade-off between hydrodynamic instability (thin film) and the capillary force limit (thick film) [32]. Finally, larger particles supply fluid to the surface through the meniscus (water trapped between the particle's curvature and the surface) [32].

In addition to using nanofluids directly as coolants, surfaces pre-coated with nanoparticles have shown significant CHF enhancement in water. Previous experiments have shown that pre-coating a surface with nanoparticles can improve CHF performance by up to 160% [1]. Surfaces can be pre-coated with nanoparticles using either boiling deposition or Layer-by-Layer (LbL) methods. An LbL method that utilizes a polymeric-nanoparticle dispersion (polyallylamine hydrochloride, or PAH) with SiO_2 or TiO_2 nanoparticles has been proven to produce a durable coating with superhydrophilic property through a multi-layer dip coating process [36]. However, this method may not be practical in real-life applications because it requires an intensive chemical process that would be both expensive and difficult to perform on a large scale. Another method for applying a thin nanoparticle coating is boiling

deposition through a single-step process. In this method, a heated surface is exposed to a nanofluid and nanoparticles are deposited on the surface during boiling. Although this nanoparticle deposition is less uniform than that obtained using the LbL method, boiling deposition may be more practical for in-situ applications in large systems because it can be performed during routine operation.

Even though nanoparticle deposition has been proven to enhance CHF, its effect on the boiling heat transfer coefficient has not been established conclusively. Although increased surface wettability enhances CHF, it tends to degrade HTC. Wang hypothesizes that an increase in surface wettability decreases the number of nucleation sites available, which in turn decreases the number of bubbles that can contribute to nucleate boiling [3]. Although nanoparticles may potentially degrade HTC, their enhancement in CHF may compensate for lower HTC during nucleate boiling in real-life applications.

Another concern for nanoparticle-treated systems is that the nanoparticle depositions may re-disperse in the coolant from the heated surface, therefore negating any CHF enhancement due to the coating. Previous experiments have shown that nanoparticle deposits can be flaky and may not adhere well to surfaces after initial coating [33]. Therefore, methods to ensure long-term nanoparticle coating adhesion should be exploited for practical applications.

1.2 Thesis Objective

1.2.1 Thesis Statement

Despite extensive research into how nanoparticles affect thermal performance, several areas for further study still exist. For example, using two types of nanoparticles of different chemical properties a heated surface may produce a composite/ heterogeneous coating with further enhance thermal performance as well as improved adhesion. To assess this concept, we

selected alumina nanoparticle and PAH dispersion for this study.

The main objective of this thesis is to examine how the addition of polymeric dispersion alumina nanofluid for heated surface pre-conditioning will affect the boiling heat transfer and CHF performance as well as the long-term adhesion of nanoparticle deposits to surfaces. The pool boiling method, which is used to determine CHF and HTC of bare and pre-coated wire heaters, and adhesion testing methods are outlined below.

1.2.2 Pool-boiling Experiments

Pool boiling is one of the simplest approaches to determining the critical heat flux (CHF) and nucleate boiling heat transfer coefficient (HTC) of a material in a fluid. In pool boiling, a material (wire or heater surface) is placed between two electrodes and immersed in stagnant water [12, 13]. Figure 3 illustrates a schematic of the typical pool-boiling experimental

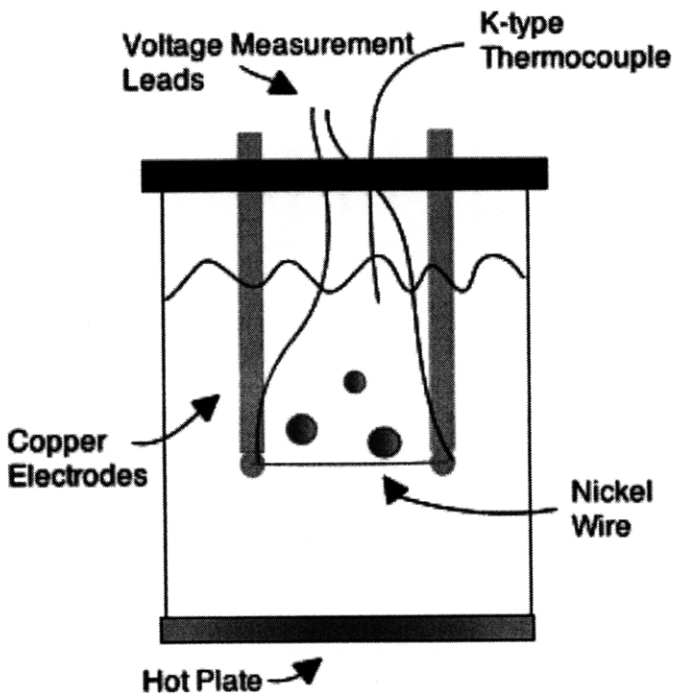

Figure 3: Experimental setup for pool-boiling facility.

set-up. The heat flux through the wire heater, as shown in Figure 3, is calculated from the power through the electrodes using the following relationship:

$$q'' = \frac{I \cdot V}{A}, \tag{5}$$

with I equal to the current (amps), V equal to the voltage (V), and A equal to the cross-sectional surface area of the material (m). Typically, the current and voltage through the electrodes (and therefore through the wire) are controlled by an external power supply. For the purpose of this thesis, the generated boiling curves will only include data up to the critical heat flux.

The wire pool-boiling method has been used in several nanofluid experiments to date at MIT [1, 5, 3]. This method can be used to coat a wire or heater with nanoparticles and to determine the boiling HTC and CHF of the bare or coated wire. To create a nanoparticle coating, a wire is placed between two electrodes and is exposed to a constant heat flux sufficient to induce nucleate boiling. The heat flux chosen for this set of experiments was 0.5MW/m^2 based on results from previous experiments [1]. As the nanofluid boils, nanoparticles are deposited on the wire surface. Images of these surface depositions can be found in Ref. [1, 6] and Sections 2 and 3.

The boiling HTC and critical heat flux can be obtained using the wire pool-boiling method. To measure the boiling curve, a bare or pre-coated wire is placed between two electrodes in deionized water [1, 5]. The heat flux through the wire is gradually increased until the wire reaches CHF. For this series of experiments, 99.98% nickel wire with a diameter of 0.22mm was used as the wire heater.[1] A wire length of 6.2 ± 0.5cm was used in all successful experiments. This wire was purchased from Alfa Aesar, stock #43131, lot #B015027 for

[1] Use of nickel wire is explained in Appendix A.

experiments conducted through 02/03/09 and experiment conducted on 02/24/09. Wire from lot #D12S002 was used in all other experiments.

A basic schematic of the wire pool-boiling facility that was used for this thesis can be found in Figure 3. When used to pre-coat a wire, the vessel contained a nanofluid. When used to determine the boiling HTC and CHF, the vessel contained deionized water. The fluid vessel was rinsed with deionized water at least twice between wire pre-coating with a nanofluid and the CHF test. A K-type thermocouple was used to determine the temperature of fluid in the vessel. The electrodes, thermal couple, and voltage measurement leads are referred to collectively as the lid assembly. For these experiments, the liquid in the vessel was heated to maintain a constant temperature (saturation temperature) with a hot plate. Both the Solid State Magnetic Stirrer with Hot Plate Model No. 4812 manufactured by Cole-Palmer of Chicago and the PC-420D manufactured by Corning were used. The external power supply for this experiment was the SRL 20-25 manufactured by Sorenson Power Supplies. The data acquisition system used in this series of experiments was the Multifunction Switch/ Measure Unit, model 34980A manufactured by Agilent Technologies. Data was recorded using the BenchLink Data Logger for 34980A, version 1.10.00, also manufactured by Agilent Technologies.

Four sets of pool-boiling experiments were conducted using deionized water, including: bare wire control experiments, pre-coated wires with alumina nanofluid (Nyacol AL20DW), alumina nanofluid + PAH (Aldrich Poly(allylamine) hydrochloride Part #283223), and PAH. The deionized water and alumina nanofluid experiments provided base cases for comparison with the alumina nanofluid + PAH and PAH experiments. The experimental procedures and results for these four tests are discussed in detail in Sections 2 and 3. Boiling curves shown in Sections 2 and 3 were generated from successful experimental data. Unsuccessful experimental

data and justification for omission from CHF and HTC calculations are included in Appendix B.

1.2.3 Adhesion Testing

Adhesion is the attractive force that holds two bodies together at their interface. In adhesion testing, a know force is applied to the interface and the stress at which separation occurs is recorded. This stress is then used as a quantitative measure of the adhesive force. This force could vary if the applied force is shear, normal, torsional, or some combination of these relative to the interface. The coating on a substrate will crack only if the attractive force (interfacial bonds) is strong enough to transfer an applied strain to the coating. If a coating fails by cracking without spallation because the tensile stress exceeds the ultimate tensile strength (UTS), then the adhesion strength is very high. A discussion of some adhesion tests follows below.

Historically, adhesion tests have been qualitative due to intrinsic differences between samples of the same surface and coating materials [19]. Intrinsic differences can result from surface impurities or non-uniform coating due to imprecise coating techniques. Currently, there are four main methods for determining coating adhesion: tape tests [20], scratch tests [15], bend/ tensile tests [11], and laser shock adhesion tests [14]. Variations of these methods are included in the American Society for Testing and Materials (ASTM) published standards for coating adhesion. Tape, scratch, and laser shock adhesion tests determine the amount of stress required to remove a coating from the material, whereas bend/ tensile tests measure the difference between the elastic modulus of the coated material and the elastic modulus of the bare material.

Tape tests measure how much coating a piece of tape with known application pressure removes when it is removed from the surface. A schematic of a simple tape test can be seen in Figure 4. Like many of the other adhesion test methods, the tape test is qualitative. The area

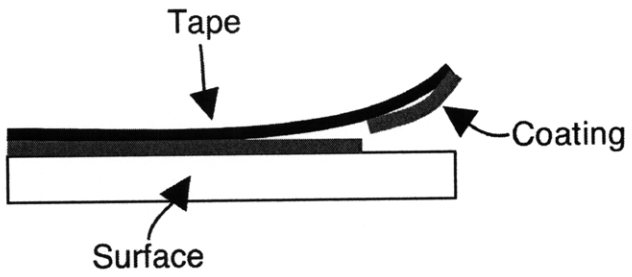

Figure 4: Simplified tape test (adapted from Ref. [14]).

of coating that the tape removes is used as a measurement of the adhesion between the coating and surface.

The scratch test determines the critical stress, or point at which detachment occurs, of the coating. In a scratch test, a stylus (typically made of diamond) is drawn across a surface with increasing load until failure occurs [15]. Failure can have several definitions, but these generally fall into the categories of cracking (in which the coating cracks superficially but is not removed from the surface), chipping or buckling (in which the coating cracks through to the surface and can be removed), and spallation [15, 17, 19]. These failure modes are identified visually and provide a mostly qualitative idea of the coating adhesion especially since different coating and substrate combinations require different stress estimations [19]. However, there have been several attempts to quantify the scratch test. According to Xie et. al., for example, the critical compressive stress for buckling is given by

$$\sigma_C = \frac{K \cdot E}{1-\nu^2} \cdot \left(\frac{t}{b}\right)^2 \qquad (6)$$

with K equal to a constant, E equal to the Young's modulus of the coating, ν equal to the Poisson ratio of the coating, t equal to the coating thickness, and b equal to the radius of the detached coating [17]. The energy release due to detachment is given by

$$W = L\sigma^2 t \cdot \frac{1-\nu^2}{E} \tag{7}$$

with L equal to a constant [17]. The difference between the measured σ (calculated from W, which is directly related to the applied load) and σ_C gives a 'quantitative' measurement of the coating to substrate adhesion.

Three-point bending and tensile tests determine the elastic modulus and detachment force, respectively, of the coating [11]. A depiction of a three-point bending or tensile test is shown in Figure 5. In the three-point bend test, the coated surface is subjected to three loads

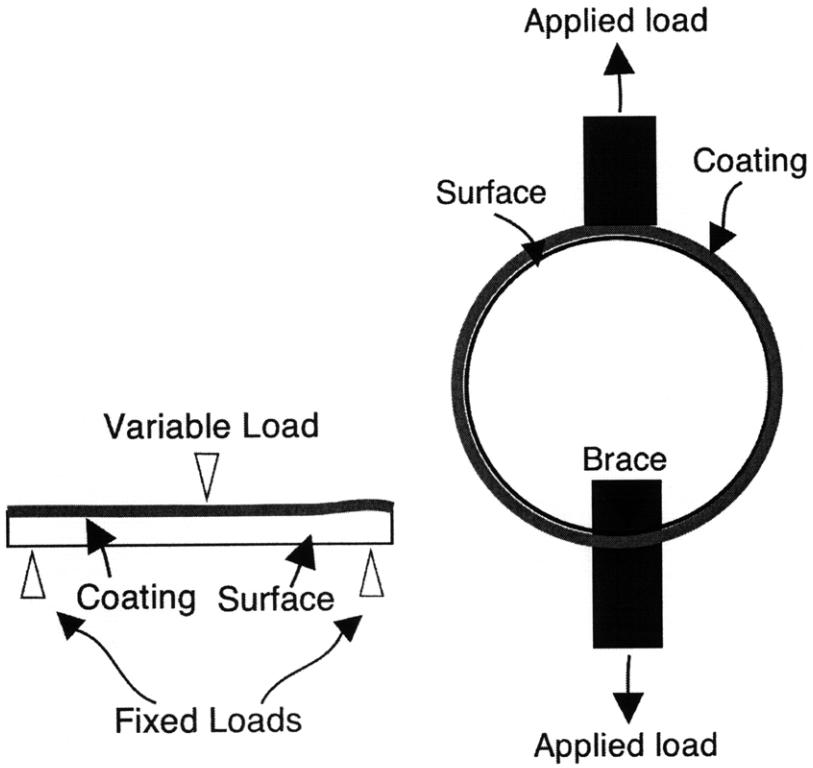

Figure 5: Three-point bending (left) and tensile (right) tests (adapted from Ref. [11]).

as depicted in Figure 5. The variable load is gradually increased until failure occurs, meaning the material fractures or, in this case, the coating cracks. In the tensile test, the material is subjected to two loads pulling in opposite directions [11]. Again, these loads are gradually increased until the coating detaches from the surface. The simplest bend test for coating

adhesion identifies the bending angle at which the coating begins to detach from the surface. This angle can then be used to find the elastic modulus of the coating. The tensile test is also relatively simple, since the load at which the coating begins to detach from the surface is a direct measurement of the adhesion strength.

Laser shock adhesion tests determine the laser loading at which the coating detaches from the surface. Figure 6 shows a simplified schematic of the concept behind the laser shock

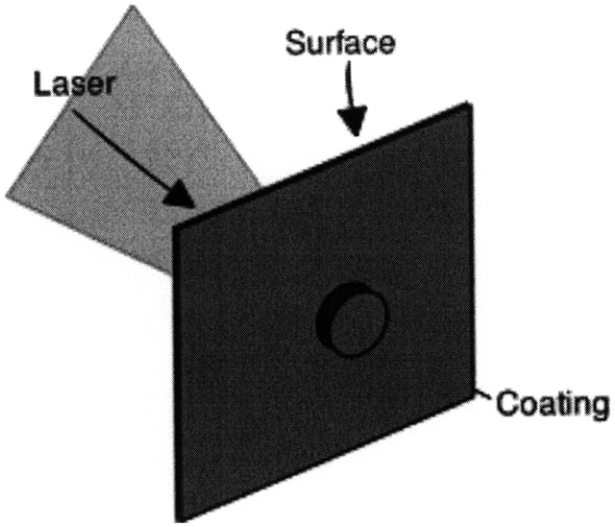

Figure 6: Laser shock adhesion test (adapted from Ref. [14]).

adhesion test. In this test, the coated surface is exposed to a laser with increasing load until defined failure occurs, meaning the coating cracks or detaches from the surface [14, 18]. The laser does not damage the coating or surface but weakens the interface between the two, causing the coating to spall off. As in the tensile test, the laser load at which the coating fails is a direct measurement of the adhesion strength.

As mentioned previously, these four basic adhesion test methods are very qualitative. However, variations on these tests exist that provide a more quantitative measurement of adhesion. The scratch and bending/ tensile tests are well-established measurements of adhesion strength, but equipment for these tests is typically not designed for the small scales that this

experimental work requires. The laser shock adhesion test has been used to measure thin metal film coating adhesion, but it requires complicated equipment and has not been well established as an adhesion test method [18]. The tape test was considered too qualitative for the purpose of this thesis. Therefore, a modified bend test was used to determine coating adhesion (this is a variation on the Mandrel test discussed in Ref. [25]). In this test, the coated surface was bent over rods of several different diameters. When the coated surface is bent, the coating experiences tensile and compressive forces as depicted in Figure 7.

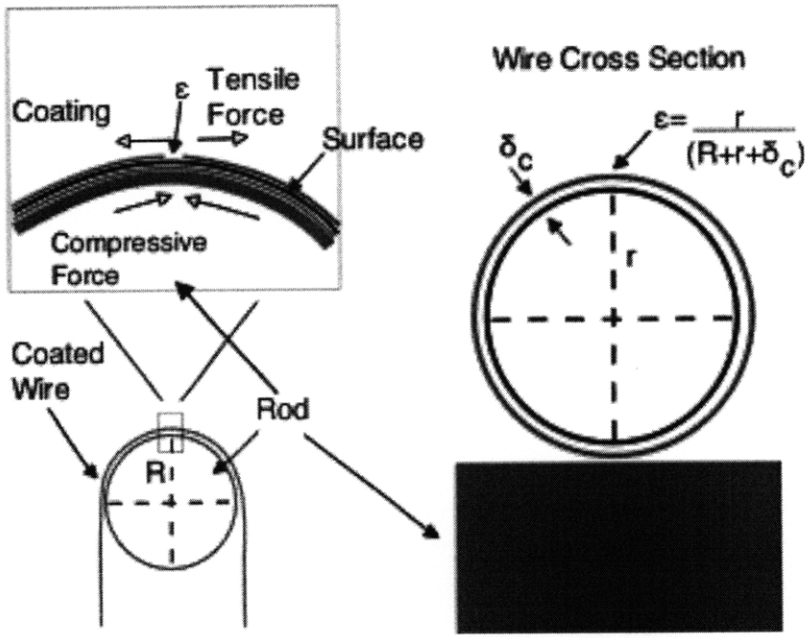

Figure 7: Modified bend test. The strain at 90° from the horizontal (labeled with ε) is calculated to determine coating adhesion (Equation 8).

Failure occurs when the tensile stress is high enough that the coating cracks or spalls from the surface due to tensile forces as described by the following equations (interfacial tensile strain and stress, respectively):

$$\varepsilon = \frac{r}{R + r + \delta_c}, \text{ and} \tag{8}$$

$$\sigma = E \cdot \varepsilon, \tag{9}$$

with r equal to the radius (wire) or thickness (plate) of the bare or coated surface (m), R equal to the rod radius (radius of curvature, m), δ_c equal to the coating thickness (assuming a uniform coating of ~5μm), E equal to the Young's modulus of the coating (N/m^2), and σ equal to the stress on the coating (N/m^2) [22, 24, 26, 30]. The rod radius that induces cracking and/or spallation is used to determine the failure stress of the coating. This failure stress provides a more quantitative measurement of the coating adhesion. The experimental procedures and results for these tests are discussed in detail in Section 5.

The adhesive strength of PAH is expected to be greater than for the alumina nanoparticles due to the difference in bonding mechanisms. The covalent bonds in a molecule of alumina do not allow for additional bonds to a surface, whereas the bonds in a polymer are weak and tend to allow for reconfiguration to create bonds to a surface. The mechanism for interfacial bonding determines the adhesion strength between the substrate and coating, and explains why PAH has better adhesion compared to alumina. Also, since PAH is a polymer, it has a greater allowable deformation before failure than alumina, which is a brittle material (discussed in Section 5). For these reasons, the PAH and combined PAH and alumina coatings are expected to show improved adhesion over a pure alumina coating.

2 Deionized Water and Alumina Nanofluid Experiments

2.1 Deionized Water Boiling HTC and CHF Baseline

The goal of this experiment was to determine the typical boiling HTC and CHF values for bare nickel wire in deionized water. The value of CHF found using deionized water provides a metric for the improvement in CHF using nanofluids. In total, three successful experiments with bare nickel wire in deionized water were conducted. Errors for CHF and HTC values were found by propagating corresponding instrumentation errors as discussed in Appendix A.

2.1.1 Experimental Procedure

- Fill inner vessel with deionized water. Heat water to saturation.
- Wire preparation: sand wire with 600-grid sandpaper 6 times and wipe down with acetone. Solder wire ends to electrodes in lid assembly. Solder voltage measurement leads to electrodes.
- Replace lid assembly with bare wire attached.
- Attach current source to electrodes.
- Connect thermocouple and current source monitoring leads to data acquisition system.
- Increase current through the wire by increments, waiting 3 minutes between each increase. For all experiments, current increments were as follows (in amps): 2, 6, 8, 10, 12, and 13 to CHF in steps of 0.5.
- Determine when CHF occurs (wire breaks).

2.1.2 Results

Figure 8 shows the boiling curve from the first deionized water experiment conducted on 02/02. In this experiment, the wire broke near the solder. A CHF value of 1.079 ± 0.072

MW/m^2 was observed.

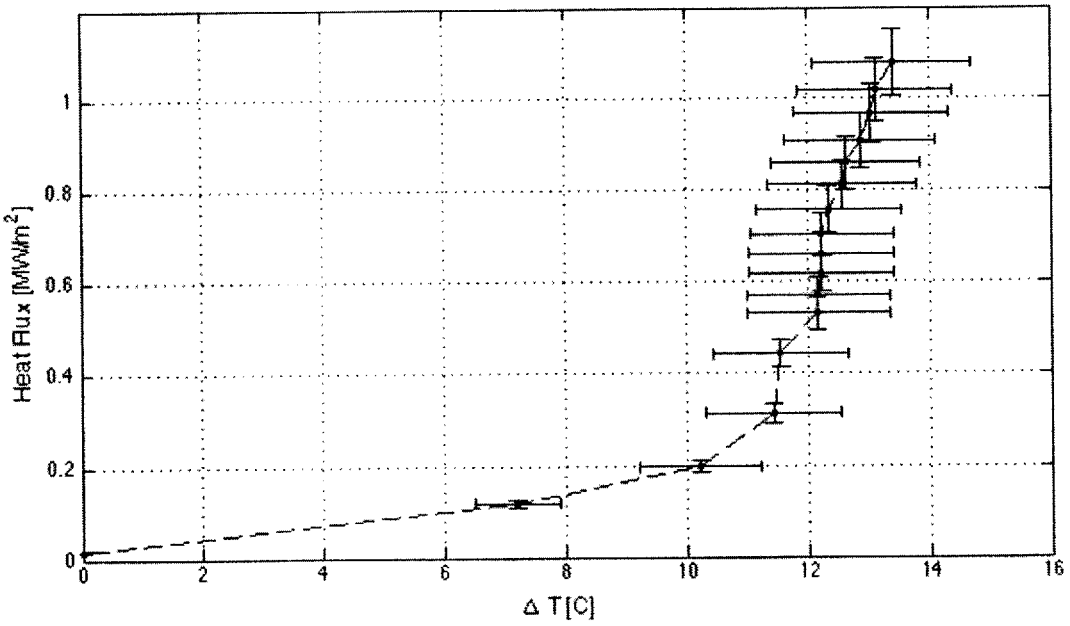

Figure 8: Boiling curve for bare nickel wire in deionized water, 02/02 test 1. CHF occurred at 1.079 MW/m^2.[2]

Figure 9 shows the boiling curve from the second deionized water experiment conducted on 02/02. In this experiment, the wire broke near the solder. A CHF value of 0.906 ± 0.061 MW/m^2 was observed.

[2] Note that error bars in all boiling curves represent instrumentation error, and do not show statistical error. Statistical error is discussed in Appendix A.3.

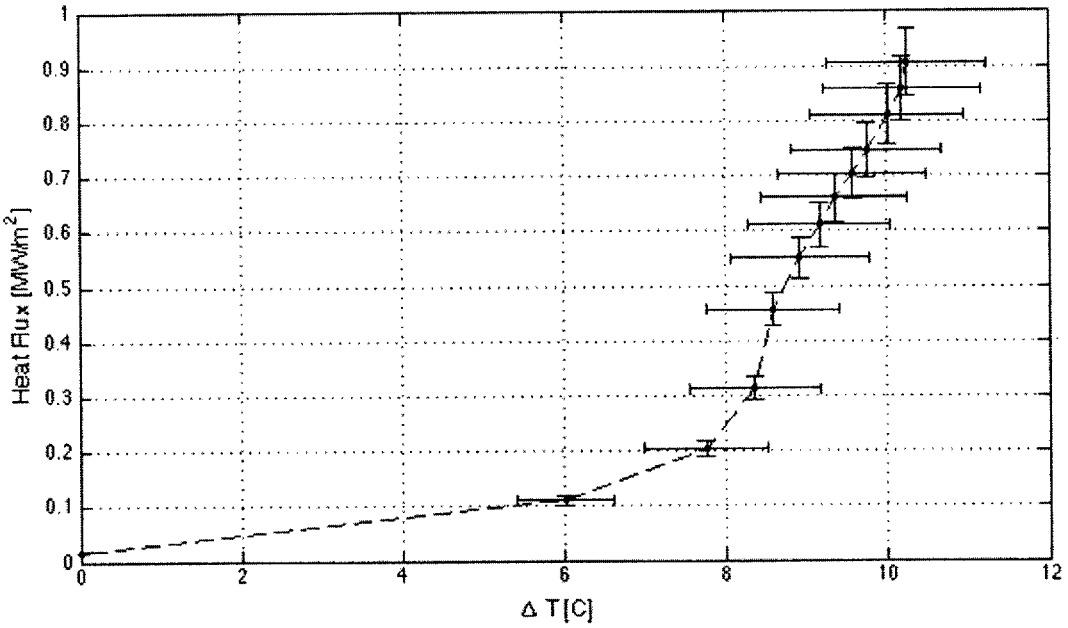

Figure 9: Boiling curve for bare nickel wire in deionized water, 02/02 test 2. CHF occurred at 0.906 MW/m^2.

Figure 10 shows the boiling curve from the third deionized water experiment conducted on 02/02. In this experiment, the wire broke near the solder. A CHF value of 1.153 ± 0.077 MW/m^2 was observed.

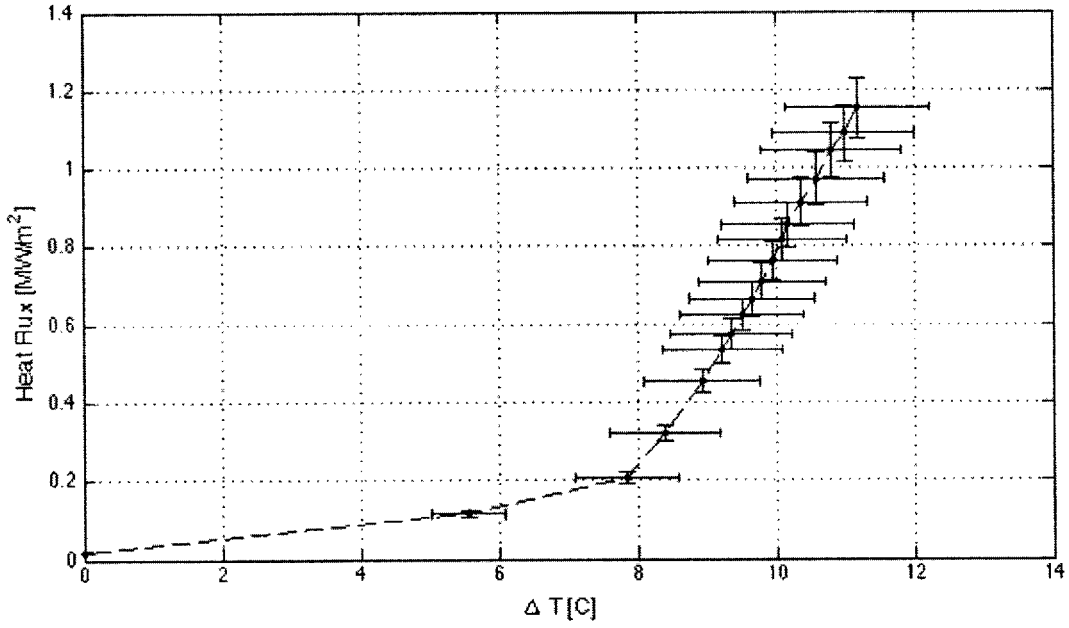

Figure 10: Boiling curve for bare nickel wire in deionized water, 02/02 test 3. CHF occurred at 1.153 MW/m^2.

2.1.3 Analysis

Figure 11 shows the boiling curves for all bare nickel wire experiments in deionized water. As can be seen in Figure 11, the CHF values for all experiments are widely distributed. The experiments also cover a wide range of temperature differences beyond the free convection region (region 1 in Figure 1). The heat transfer coefficients, which are equal to q″/ΔT, in the nucleate boiling region also vary. All CHF and HTC calculations were performed using data from 02/02 experiments 1, 2, and 3.

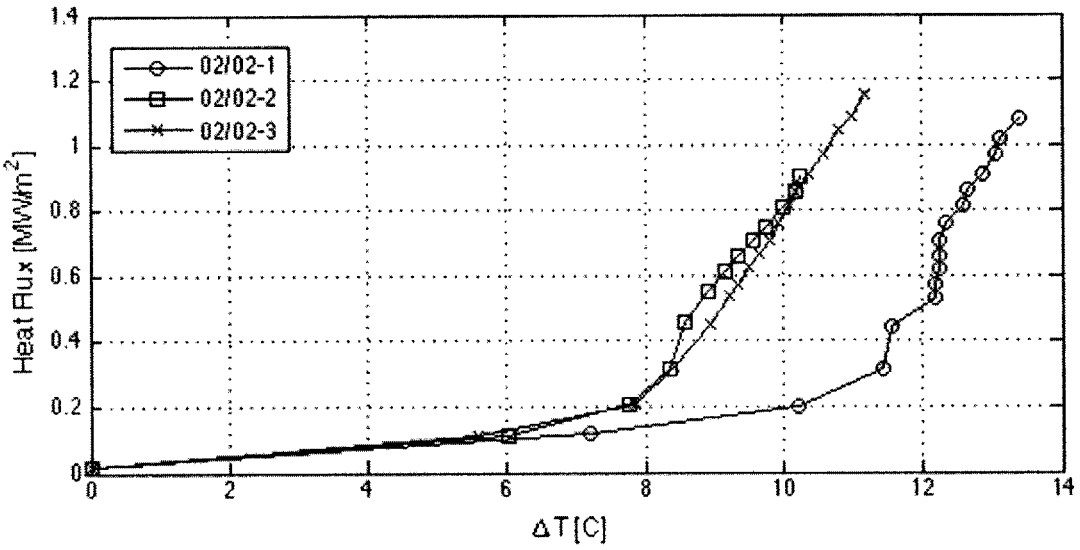

Figure 11: Boiling curves for bare nickel wire in deionized water.

Table 1 contains CHF values for the successful experiments conducted on 02/02. As can be seen, the CHF values for these experiments are within 27% of one another and have fairly close agreement. The average CHF value is also within 15% of the successful experiments.

Table 1: CHF values for bare nickel wire in deionized water.

Experiment	*CHF (MW/m^2)*	*Error (MW/m^2)*
02/02 Test 1	1.079	0.072
02/02 Test 2	0.906	0.061
02/02 Test 3	1.153	0.077
Average	1.046	0.041

According to Zuber, the critical heat flux for an infinite horizontal plate can be found with the hydrodynamic instability model:

$$q''_{max,Z} \equiv 0.131\rho_g^{1/2}h_{fg}\sqrt[4]{g(\rho_f-\rho_g)\sigma}, \tag{10}$$

with all variables defined in Section 1 [12]. This equation is modified for different geometries with the following:

$$\frac{q''_{max}}{q''_{max,Z}} = fn(R'), \tag{11}$$

with fn(R′) defined for the heater geometry [12]. R′ can be found using:

$$R' = \frac{R}{\sqrt{\sigma/g(\rho_f-\rho_g)}}. \tag{12}$$

For a horizontal cylinder of radius R, CHF can be found using [12]:

$$\frac{q''_{max}}{q''_{max,Z}} = 0.89 + 2.27e^{-3.44\sqrt{R'}}, 0.15 \leq R' \tag{13}$$

For a small horizontal cylinder of radius R, CHF can be found using [12]:

$$\frac{q''_{max}}{q''_{max,Z}} = \frac{0.94}{(R')^{1/4}}, 0.15 \leq R' \leq 4.26 \tag{14}$$

For the wire used in these experiments (R equal to 0.11mm), R′ was found to be 0.044 using water properties at saturation, which is much less than the lower limit of 0.15 for Equations 13 and 14. The wire CHF is no longer governed by hydrodynamic instabilities at R′ values below 0.15. Therefore, Equations 13 and 14 are invalid for the heater geometry used in these experiments. In the transition region when R′ is between 0.01 and 0.15, values of $q''_{max}/q''_{max,Z}$ vary between 0.5 and 1.0 [37]. The CHF value calculated using this relationship lies anywhere from 0.554 MW/m^2 to 1.108 MW/m^2. The measured CHF value for bare nickel wire in deionized water of 1.046 MW/m^2 lies within this transition range. For comparison, the CHF value for a bare steel wire in deionized water was found experimentally in a previous study to be

~1 MW/m^2, which is consistent with the results obtained in this study [5].

Figure 12 shows the heat transfer coefficient as a function of heat flux for the three successful bare wire experiments. The values of the heat transfer coefficients are fairly consistent among the successful tests, and although error bars are omitted for visual clarity, all of the test values are within error range of the average values (see Figure B.1-9). The HTC was calculated using the measured heat flux and temperature data and therefore has some measurement uncertainty (explained in detail in Appendix A). The uncertainty values found for the heat flux and temperature data were propagated to the HTC values, but are not included in Figure 12 (they are included in Figure B.1-9). The average bare wire HTC values are used as comparison baseline for HTC values of the pre-coated wires as discussed in Sections 2.2, 3.2, and 3.3.

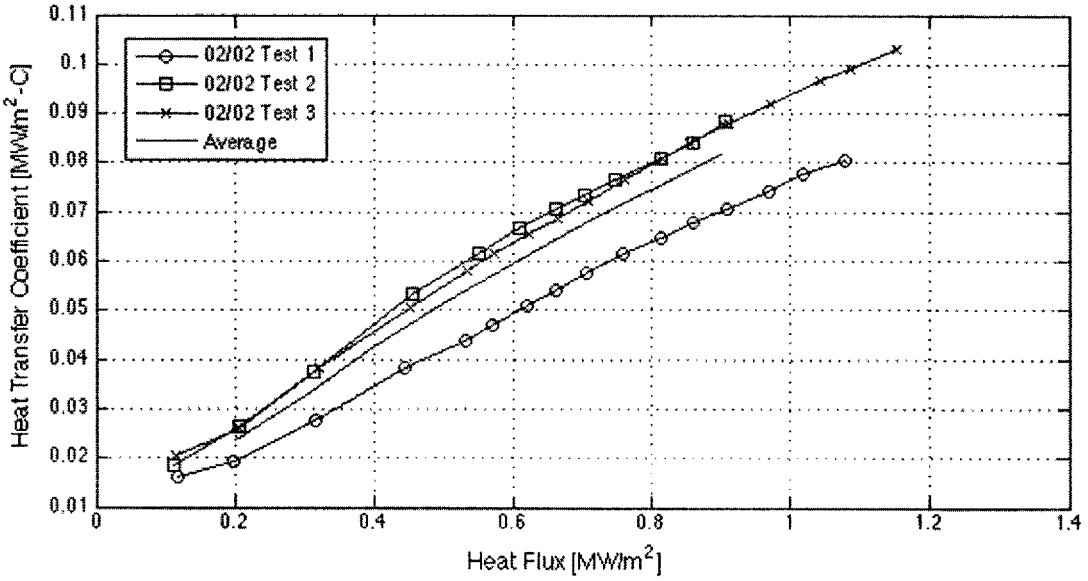

Figure 12: Heat transfer coefficients versus heat flux for bare nickel wire in deionized water. The average HTC stops at the lowest CHF point of the curves used to generate the average.

2.2 Effects of Alumina Nanoparticle Coating on Boiling HTC and CHF

The goal of this experiment was to determine what effect alumina coating has on the boiling HTC and CHF of nickel wire in deionized water. The addition of the alumina nanoparticles in water was expected to increase the CHF of the nickel wire by improved surface wettability as demonstrated and discussed in Ref. [1, 3, 5]. This experiment involved pre-coating wire and then conducting the boiling heat transfer tests in deionized water using the procedure outlined below. The nickel wire was pre-coated with 1.0% and 0.1% by volume alumina nanofluid (Nyacol AL20DW) and with 1.0% and 0.1% by volume silica nanofluid. In total, fourteen experiments were conducted with pre-coated nickel wires.

2.2.1 Experimental Procedure

- Preparation: sand wire with 600-grid sandpaper and wipe down with acetone. Solder wire ends to electrodes in lid assembly. Solder thermocouple to electrodes.
- Prepare 3500 mL nanofluid with the following composition:

Table 2: Alumina nanofluid composition.

Composition	*DI Water (mL)*	*Alumina Nanofluid (mL)*
0.1% by volume	3441	59
1.0% by volume	2804	696

Table 3: Silica nanofluid composition (using Sigma-Aldrich LUDOX TMA colloidal silica, 34wt.% in deionized water).

Composition	*DI Water (mL)*	*Silica Nanofluid (mL)*
0.1% by volume	3481	19
1.0% by volume	3305	195

The dilution of the nanofluid was done using the following relationship [38]:

$$f = n \cdot \frac{\left(\frac{1-y}{y}\right) - \left(\frac{1-x}{x}\right)\cdot\left(\frac{\rho_p}{\rho_w}\right)}{1+\left(\frac{1-x}{x}\right)\cdot\left(\frac{\rho_p}{\rho_w}\right)} \qquad (15)$$

with x equal to the weight percent of the original nanofluid from the vendor, y equal to the desired volume percent of the fluid, n equal to the amount of x w% nanofluid (mL), f equal to the amount of water required for dilution (mL), and ρ_p and ρ_w equal to the density of the nanoparticle and water (g/mL), respectively. The density of alumina and silica nanoparticles is assumed to be that of bulk alumina and silica, which is 3.90 g/mL and 2.22 g/mL, respectively.

- Put lid assembly into inner vessel filled with boiling prepared nanofluid.
- Attach current source to electrodes.
- Connect thermocouple and voltage measurement leads to data acquisition system.
- Set heat flux to 0.5MW/m^2. Keep wire at this heat flux in boiling nanofluid for 30 minutes.
- Visually inspect if coating exists to affect CHF performance.
- Follow procedure outlined in Section 2.1 to determine CHF.

2.2.2 Results

1.0% Alumina

Figure 13 shows the boiling curve from the alumina-pre-coated experiment conducted on 11/18. In this experiment, the wire broke near the solder. A CHF value of 1.271 ± 0.085 MW/m^2 was observed.

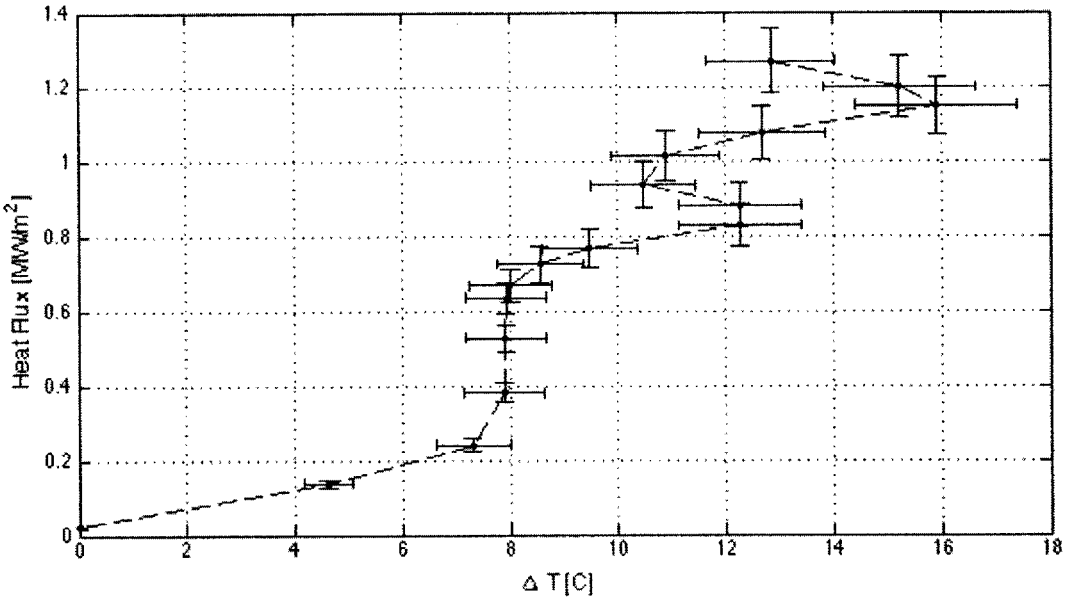

Figure 13: Boiling curve for 1.0% alumina-pre-coated nickel wire in deionized water, 11/18 test 1. CHF occurred at 1.271 MW/m^2.

Figure 14 shows the boiling curve from the alumina-pre-coated experiment conducted on 01/05. In this experiment, the wire broke near the solder. A CHF value of 1.242 ± 0.083 MW/m^2 was observed.

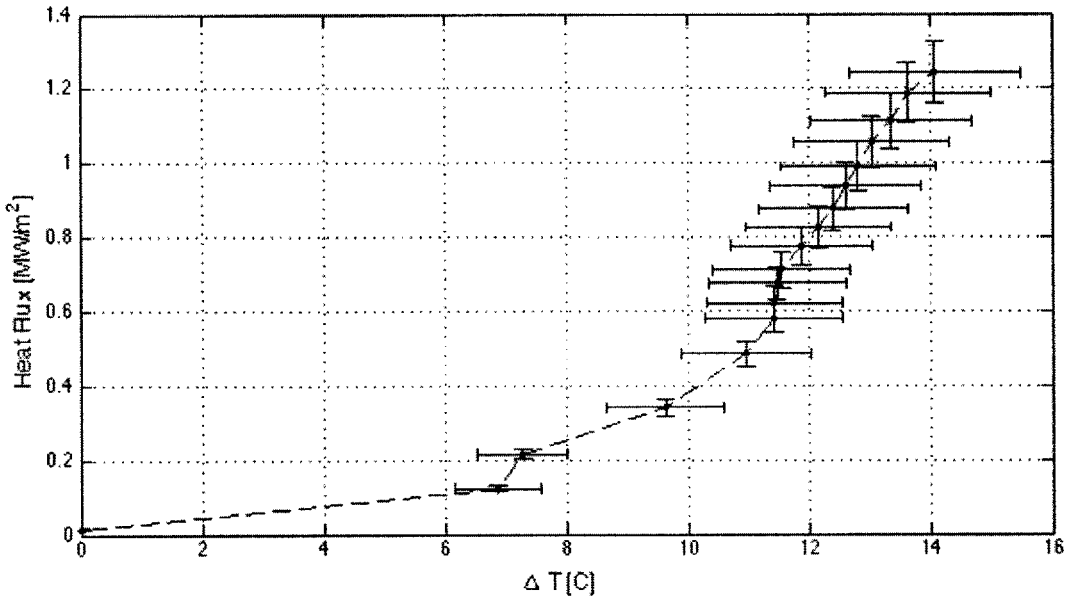

Figure 14: Boiling curve for 1.0% alumina-pre-coated nickel wire in deionized water, 01/05 test 1. CHF occurred at 1.242 MW/m^2.

Figure 15 shows the boiling curve from the alumina-pre-coated experiment conducted on 01/06. In this experiment, the wire radiated and broke near the solder. A CHF value of 1.229 ± 0.082 MW/m^2 was observed.

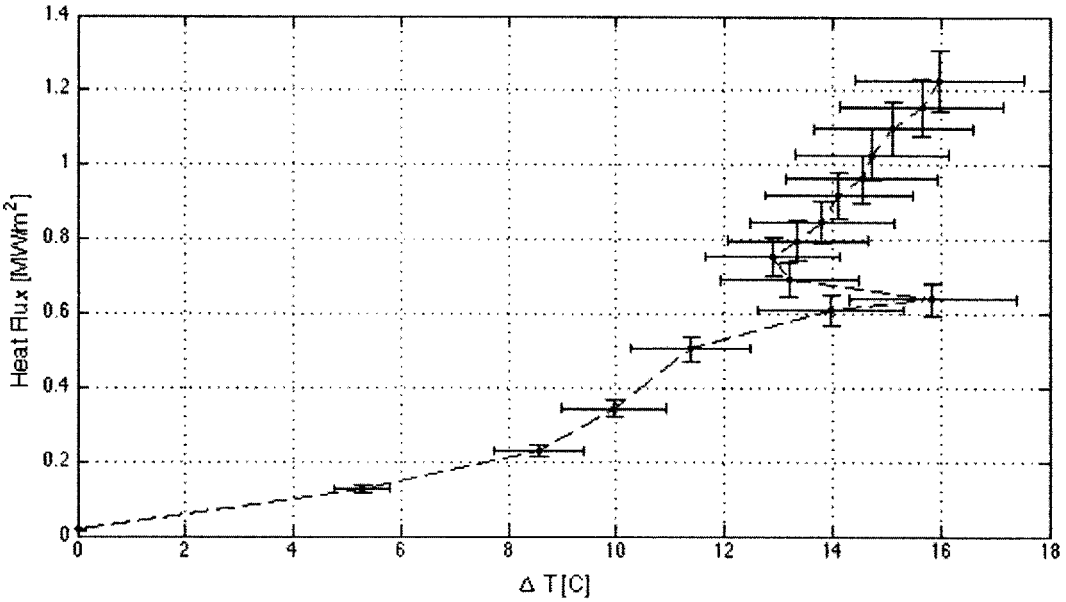

Figure 15: Boiling curve for 1.0% alumina-pre-coated nickel wire in deionized water, 01/06 test 1. CHF occurred at 1.229 MW/m^2.

Figure 16 shows the boiling curve from the alumina-pre-coated experiment conducted on 02/03. In this experiment, the wire broke near the solder. A CHF value of 2.115 ± 0.141 MW/m^2 was observed.

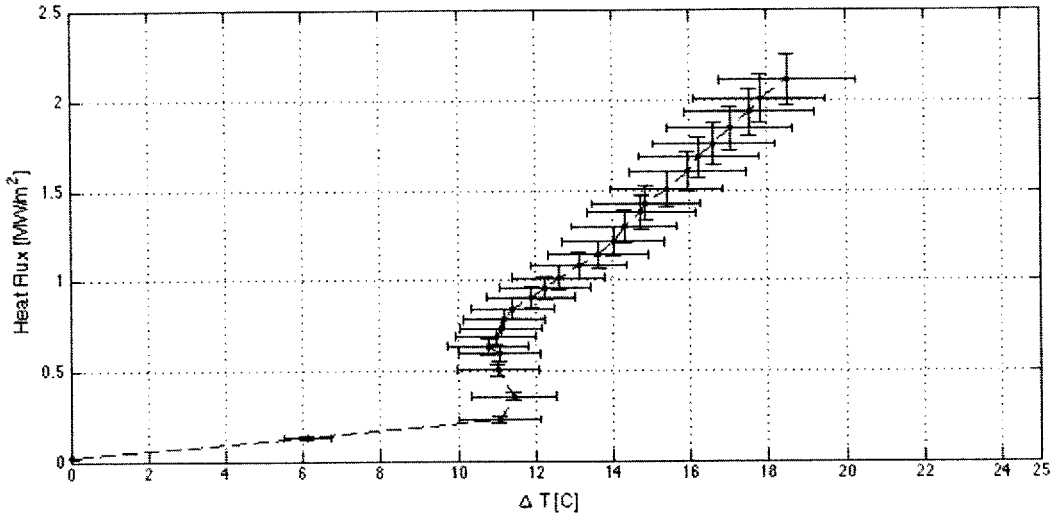

Figure 16: Boiling curve for 1.0% alumina-pre-coated nickel wire in deionized water, 02/03 test 1. CHF occurred at 2.115 MW/m^2.

0.1% Alumina

Figure 17 shows the boiling curve from the alumina-pre-coated experiment conducted on 02/05. In this experiment, the wire broke near the center. A CHF value of 1.552 ± 0.104 MW/m^2 was observed.

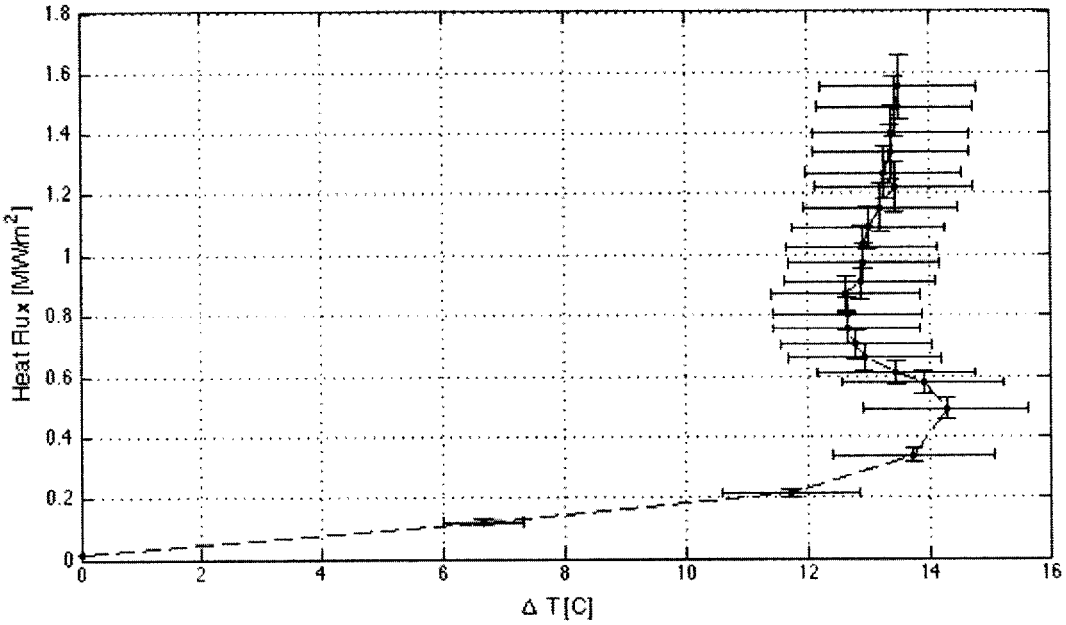

Figure 17: Boiling curve for 0.1% alumina-pre-coated nickel wire in deionized water, 02/05 test 1. CHF occurred at 1.552 MW/m^2.

Figure 18 shows the boiling curve from the first alumina-pre-coated experiment conducted on 02/06. In this experiment, the wire broke near the solder. A CHF value of 1.142 ± 0.076 MW/m^2 was observed.

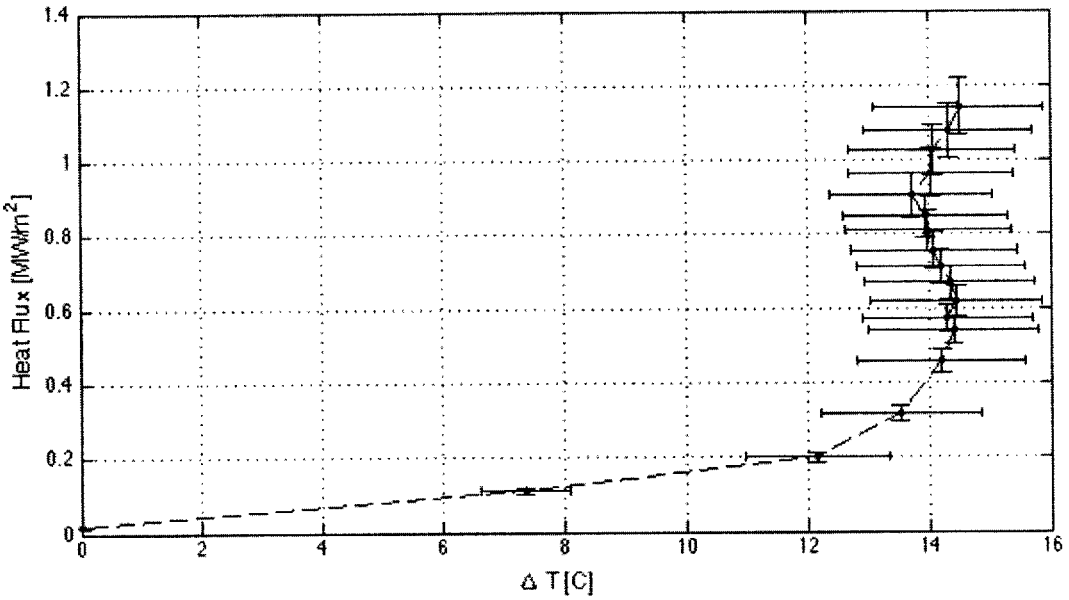

Figure 18: Boiling curve for 0.1% alumina-pre-coated nickel wire in deionized water, 02/06 test 1. CHF occurred at 1.142 MW/m^2.

Figure 19 shows the boiling curve from the second alumina-pre-coated experiment conducted on 02/06. In this experiment, the wire broke near the solder. A CHF value of 1.469 ± 0.098 MW/m^2 was observed.

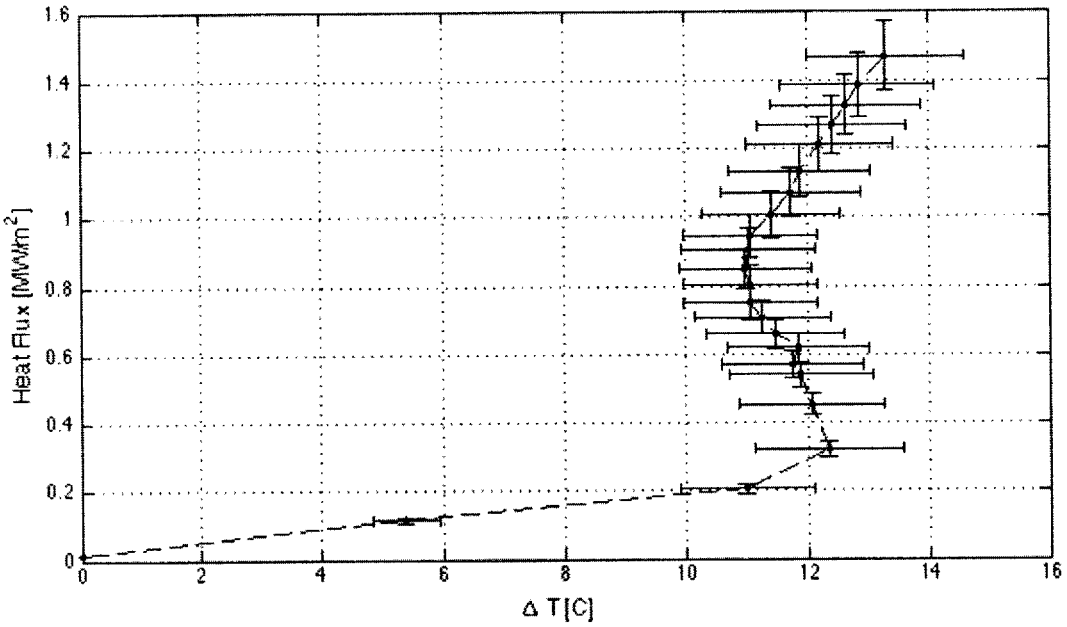

Figure 19: Boiling curve for 0.1% alumina-pre-coated nickel wire in deionized water, 02/06 test 2. CHF occurred at 1.469 MW/m^2.

Figure 20 shows the boiling curve from the alumina-pre-coated experiment conducted on 02/09. In this experiment, the wire broke near the solder. A CHF value of 1.516 ± 0.101 MW/m^2 was observed.

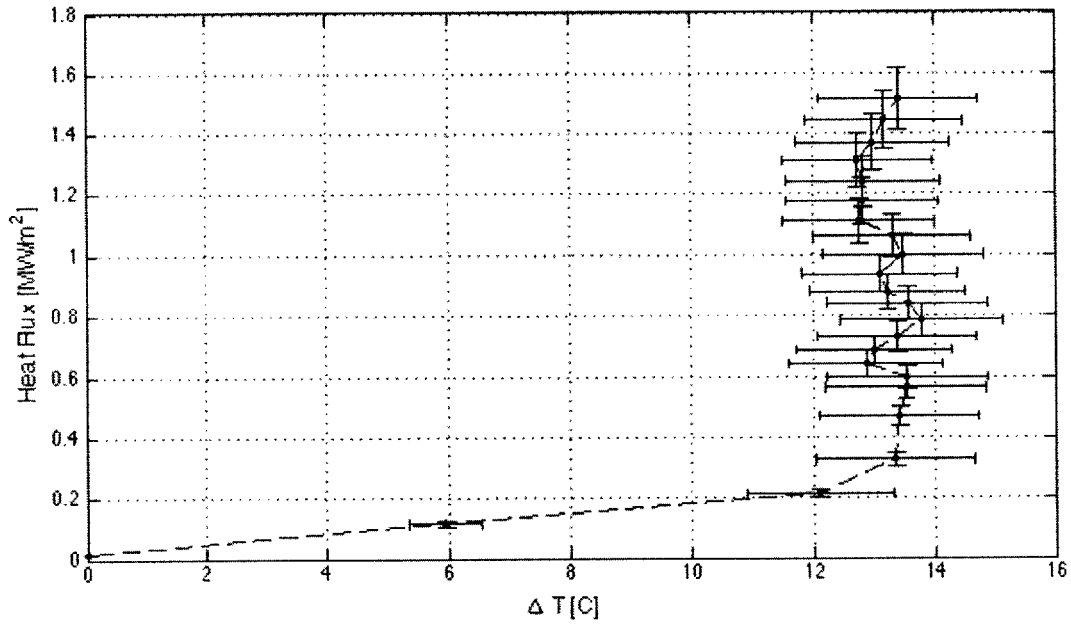

Figure 20: Boiling curve for 0.1% alumina-pre-coated nickel wire in deionized water, 02/09 test 1. CHF occurred at 1.516 MW/m^2.

Figure 21 shows the boiling curve from the alumina-pre-coated experiment conducted on 02/10. In this experiment, the wire broke near the solder. A CHF value of 1.280 ± 0.086 MW/m^2 was observed.

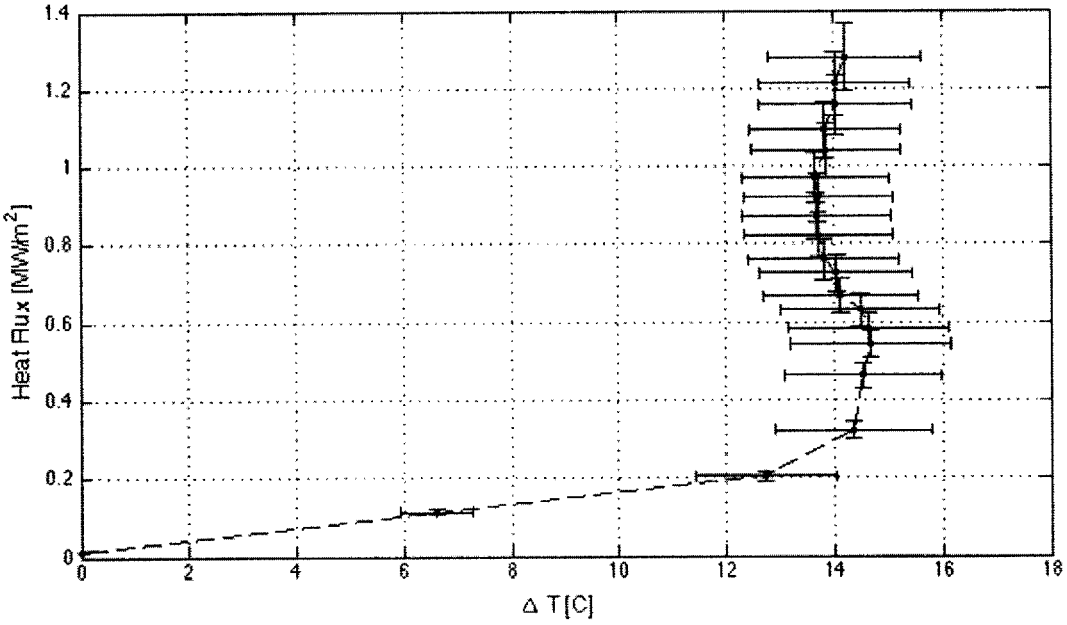

Figure 21: Boiling curve for 0.1% alumina-pre-coated nickel wire in deionized water, 02/10 test 1. CHF occurred at 1.280 MW/m^2.

Figure 22 shows the boiling curve from the alumina-pre-coated experiment conducted on 02/11. In this experiment, the wire broke near the solder. A CHF value of 1.685 ± 0.112 MW/m^2 was observed.

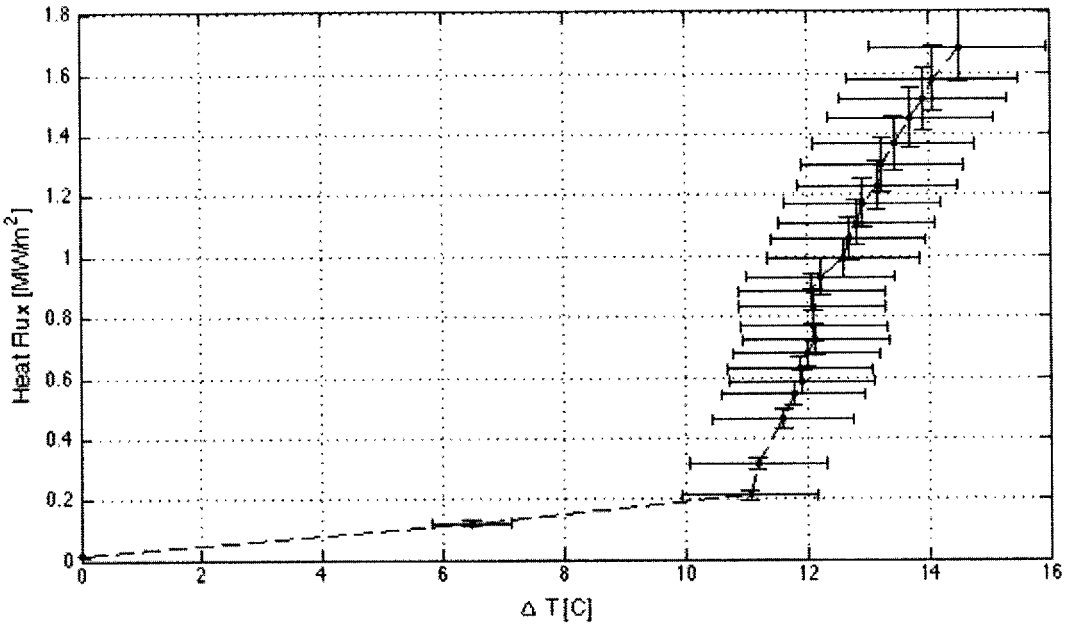

Figure 22: Boiling curve for 0.1% alumina-pre-coated nickel wire in deionized water, 02/11 test 1. CHF occurred at 1.685 MW/m^2.

Figure 23 shows the boiling curve from the alumina-pre-coated experiment conducted on 02/13. In this experiment, the wire broke near the solder. A CHF value of 1.362 ± 0.091 MW/m^2 was observed.

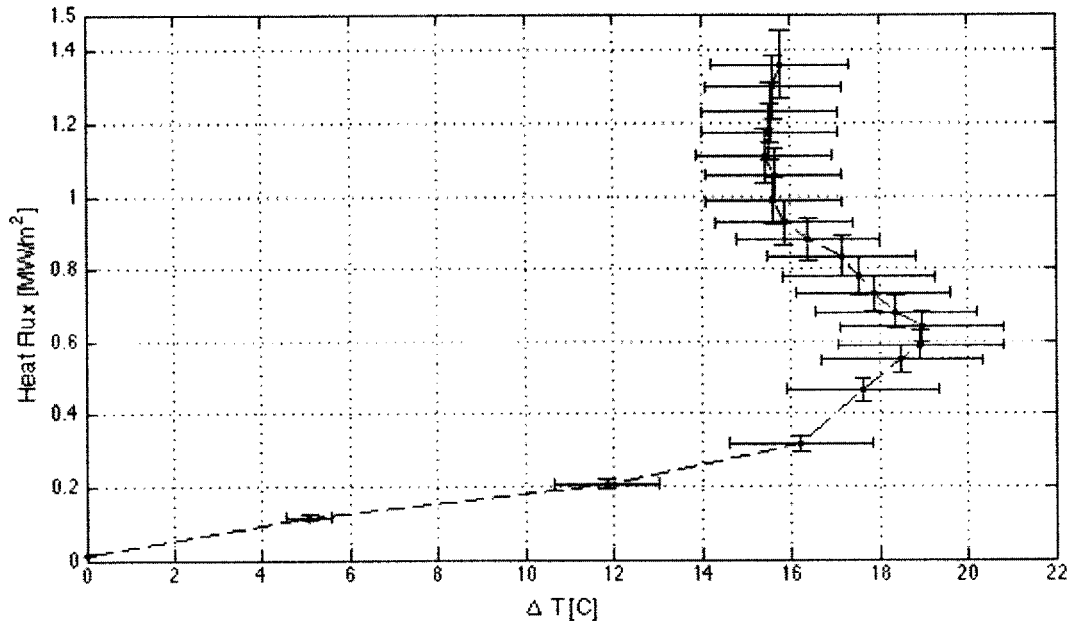

Figure 23: Boiling curve for 0.1% alumina-pre-coated nickel wire in deionized water, 02/13 test 1. CHF occurred at 1.362 MW/m^2.

2.2.3 Analysis

1.0% Alumina

Although CHF experiments were conducted with both 1.0% and 0.1% alumina nanofluids, this thesis focuses on the results from the 0.1% alumina CHF and HTC analyses. Therefore, CHF experiments on 1.0% alumina pre-coated wires were not rigorously conducted. A more complete examination of the effect of alumina pre-coating can be found in the next section, which discusses results from 0.1% alumina-pre-coated wires. Figure 24 shows the boiling curves for all 1.0% alumina-pre-coated nickel wire CHF experiments in deionized water. As can be seen in Figure 24, the CHF values for all experiments are relatively close. However, the experiments cover a wide range of temperature differences beyond the free convection region. The heat transfer coefficients, which are equal to $q''/\Delta T$, in the nucleate boiling region also vary.

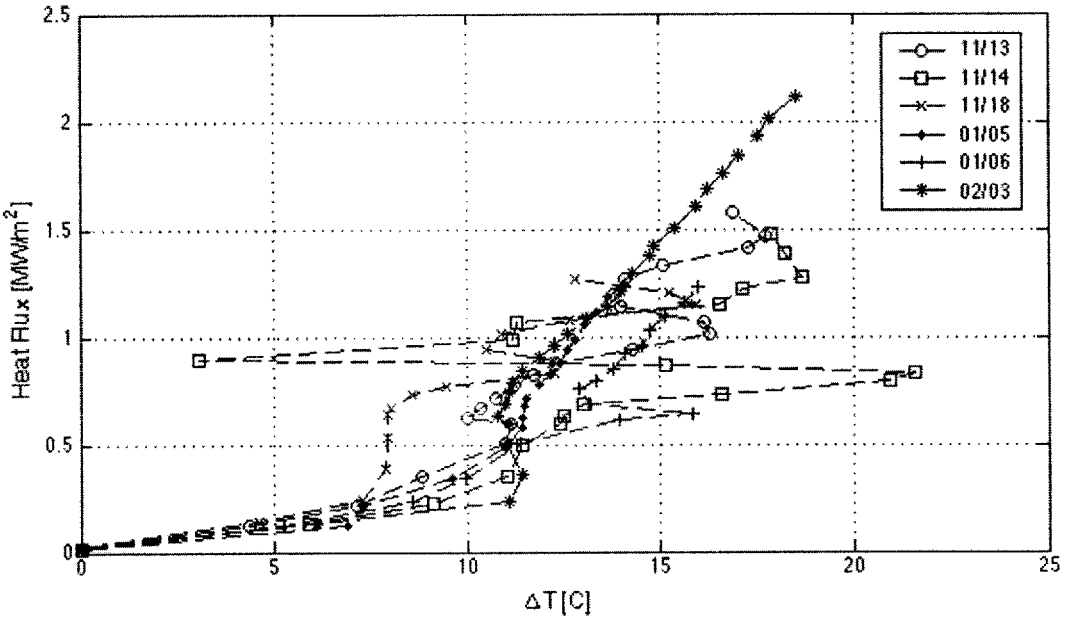

Figure 24: Boiling curves for 1.0% alumina-pre-coated nickel wire in deionized water.

Table 4 contains the CHF values for each experiment as well as the average CHF value

Table 4: CHF values for 1.0% alumina-pre-coated nickel wire in deionized water.

Test	*CHF* (MW/m^2)	*CHF Error* (MW/m^2)
11/14	1.474	0.098
11/18	1.271	0.085
01/05	1.242	0.083
Average*	1.329	0.051

*CHF results from 11/07, 11/13, 01/06, and 02/03 were omitted as explained in Appendix B.2.

for the successful experiments. As can be seen, the CHF values for the successful CHF experiments (11/14, 11/18, and 01/05) are within error range of one another and have fairly close agreement. The average CHF value is also within error range of the three successful CHF experiments. The average CHF ratio of the 1.0% alumina-pre-coated wire to bare wire is 1.271 ± 0.069.

Figure 25 shows the heat transfer coefficient as a function of heat flux for the successful 1.0% alumina pre-coated wire experiments. Note that successful CHF and successful HTC experiments are not necessarily the same due to the criteria outlined in Appendix B. The values of the heat transfer coefficients are fairly consistent among the successful tests, and although error bars are omitted for visual clarity, all of the test values are within error range of the average values (see Figure B.2-4).

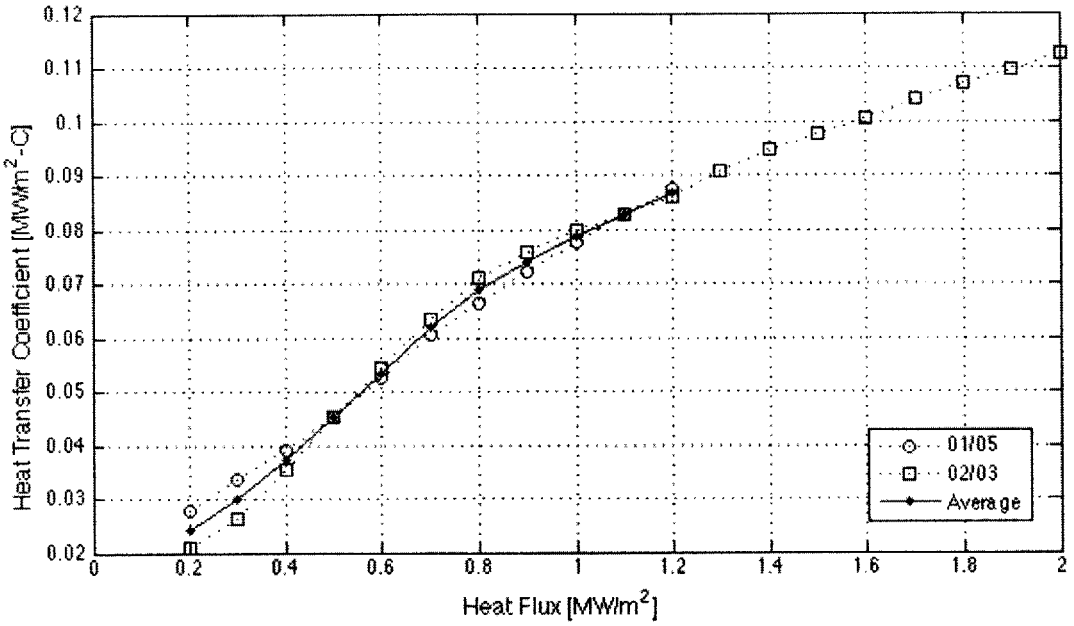

Figure 25: Heat transfer coefficients versus heat flux for 1.0% alumina-pre-coated nickel wire in deionized water. Please note that only 2 tests were included in the HTC analysis as explained in Appendix B.2.

Figure 26 shows the ratio of the 1.0% alumina-pre-coated nickel wire heat transfer coefficients to the average bare wire heat transfer coefficients at various heat fluxes. Although there is some variation in this ratio among the successful experiments, the ratio of the average alumina heat transfer coefficient values to the average bare wire HTC values is 0.917 ± 0.026.[3]

[3] This value and subsequent HTC ratios were found by taking the ratio of the coated wire heat transfer coefficient to the bare wire heat transfer coefficient at heat fluxes of 0 to 2 MW/m^2 in steps of 0.1 MW/m^2. The percentages were then averaged over the entire range of heat flux values.

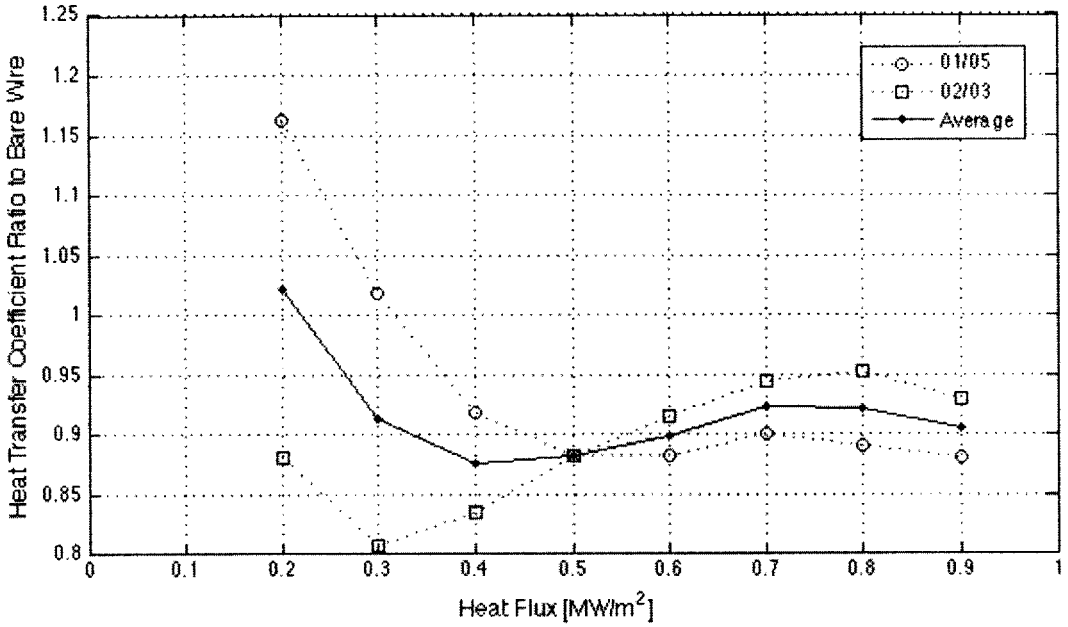

Figure 26: Ratio of 1.0% alumina-pre-coated nickel wire heat transfer coefficients to the average bare wire heat transfer coefficients.

Figure 27 illustrates the surface morphology of the 1.0% alumina-pre-coated nickel wire at 250, 1000, and 5000 times magnification using SEM imaging (clockwise from upper left). The fourth image shows the coating composition determined by energy dispersive spectroscopy (EDS). As can be seen from the EDS graph, the nickel wire is entirely coated in alumina. The copper contribution is most likely a contaminant from the copper electrodes used to coat the nickel wire.

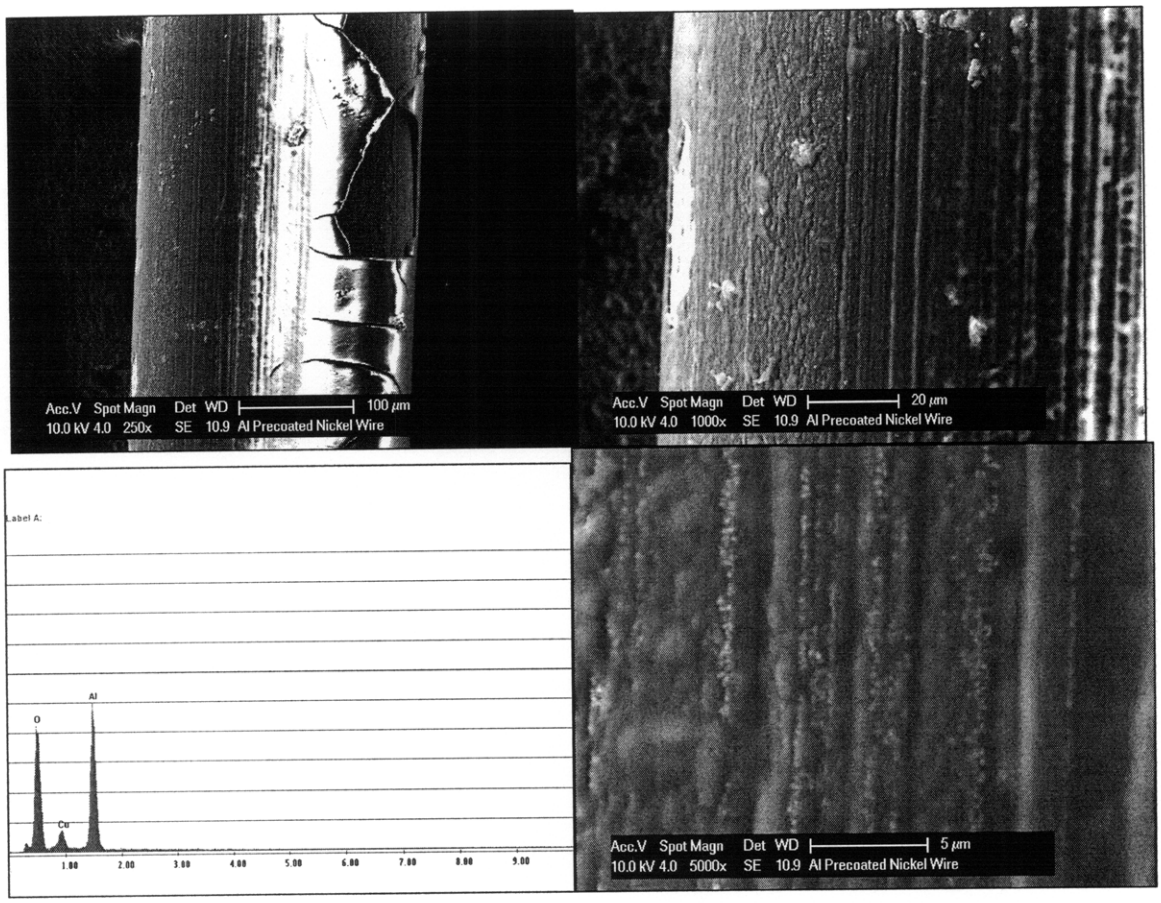

Figure 27: 1.0% alumina-pre-coated wire surface morphology and material composition. Clockwise from top left: 250x, 1000x, 5000x, and EDS data taken after 5000x SEM.

0.1% Alumina

Figure 28 shows the boiling curves for all 0.1% alumina-pre-coated nickel wire experiments in deionized water. As can be seen in Figure 28, the CHF values for all experiments are relatively close. However, the experiments cover a wide range of temperature differences beyond the free convection region. The heat transfer coefficients, which are equal to $q''/\Delta T$, in the nucleate boiling region also vary.

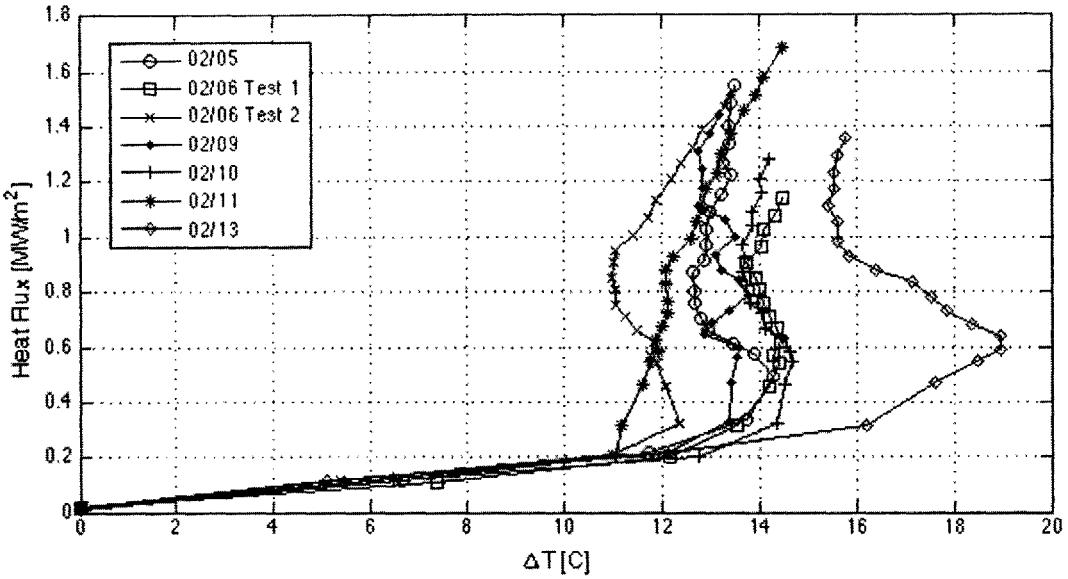

Figure 28: Boiling curves for 0.1% alumina-pre-coated nickel wire in deionized water.

Table 5 contains the CHF values for each experiment as well as the average CHF value for the successful experiments. As can be seen, the CHF values for the successful experiments (all experiments excluding that conducted on 02/11 and 02/06-1, which appear to be outliers) are within ~22% of one another, which is a fairly close agreement considering coating inconsistencies inherent in boiling deposition. The average CHF value is also within ~25% of these successful experiments. The average CHF ratio of the 0.1% alumina-pre-coated wire to bare wire is 1.366 ± 0.064.

Table 5: CHF values for 0.1% alumina-pre-coated nickel wire in deionized water.

Test	*CHF (MW/m2)*	*CHF Error (MW/m2)*
02/05	1.552	0.104
02/06-1	1.142	0.076
02/06-2	1.467	0.098
02/09	1.516	0.101
02/10	1.280	0.086
02/11	1.685	0.112
02/13	1.362	0.091
Average	1.429	0.036

Figure 29 shows the heat transfer coefficient as a function of heat flux for the successful 0.1% alumina-pre-coated wire experiments. The values of the heat transfer coefficients are fairly

consistent among the successful tests, and although error bars are omitted for visual clarity, all of the test values are within error range of the average values (see Figure B.3-2).

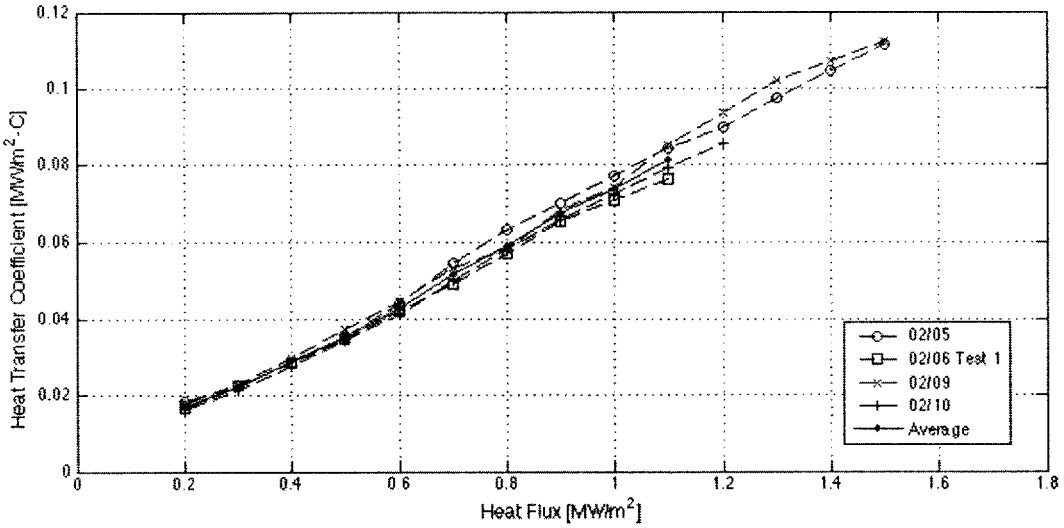

Figure 29: Heat transfer coefficients versus heat flux for 0.1% alumina-pre-coated nickel wire in deionized water.

Figure 30 shows the ratio of the 0.1% alumina-pre-coated nickel wire heat transfer coefficients to the average bare wire heat transfer coefficients at various heat fluxes. Although there is some variation in this ratio among the successful experiments, the ratio of the average 0.1% alumina heat transfer coefficient values to the average bare wire HTC values is 0.734 ± 0.019.

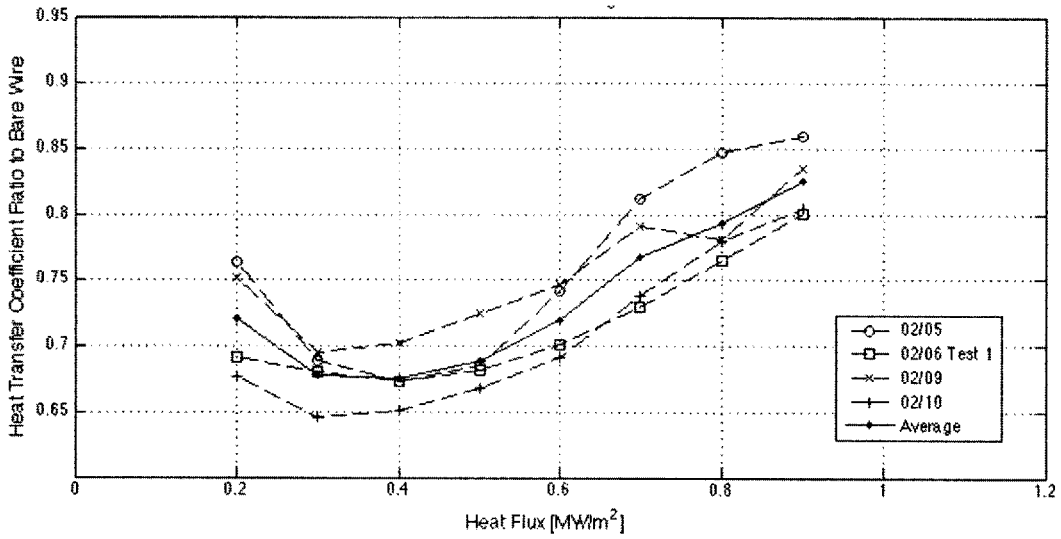

Figure 30: Ratio of 0.1% alumina-pre-coated nickel wire heat transfer coefficients to the average bare wire heat transfer coefficients.

Figure 31 illustrates the surface morphology of the 0.1% alumina-pre-coated nickel wire at 250, 1000, and 5000 times magnification using SEM imaging (clockwise from upper left). The fourth image shows the coating composition determined by EDS. As can be seen from the EDS graph, the nickel wire is only partially coated by the alumina.

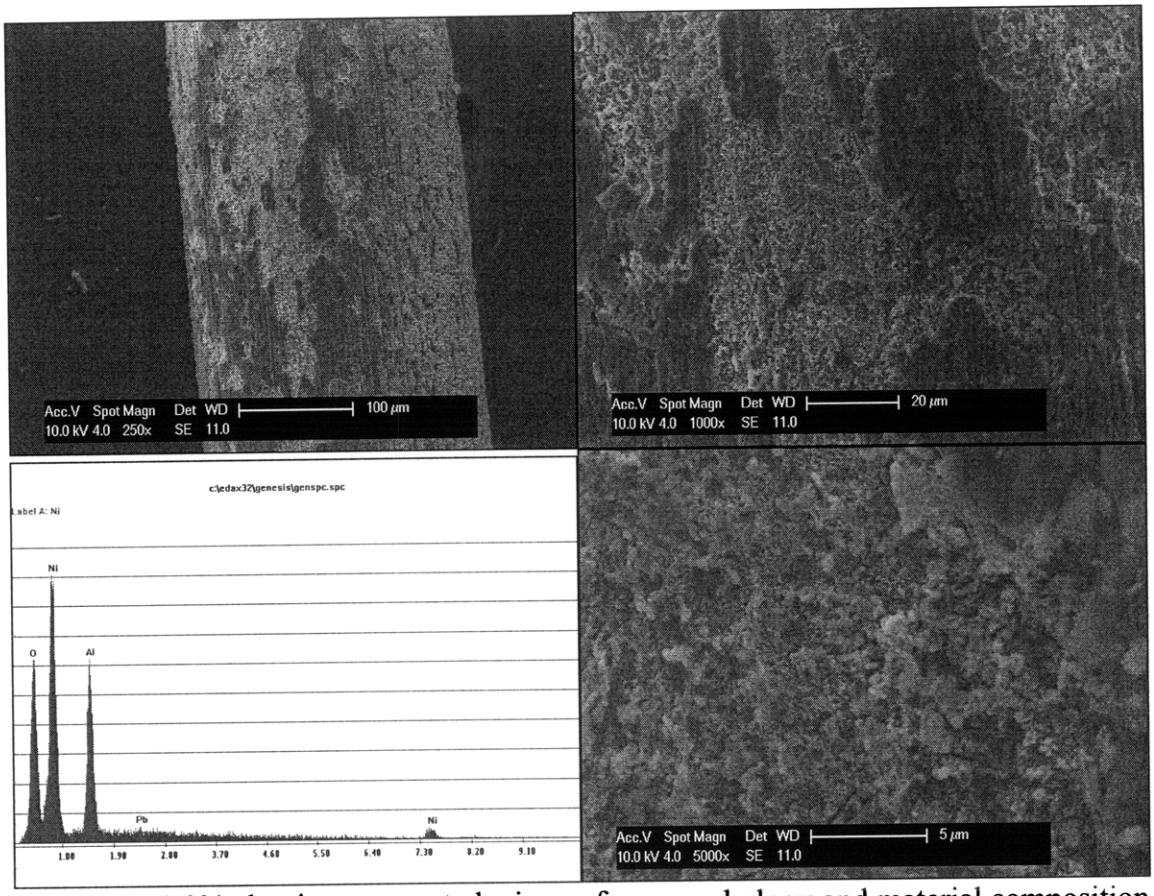

Figure 31: 1.0% alumina-pre-coated wire surface morphology and material composition. Clockwise from top left: 250x, 1000x, 5000x, and EDS data taken after 5000x SEM.

2.2.4 Comparison Between 1.0% and 0.1% Alumina pre-coated Wires

Figure 32 compares the average heat transfer coefficient ratio of 1.0% alumina and 0.1% alumina-pre-coated wires to bare wire. As can be seen, there is a significant difference between the 0.1% and 1.0% alumina-pre-coated heat transfer coefficients. Although the 0.1% alumina-pre-coated wires typically have a higher CHF than the 1.0% alumina-pre-coated wires, the average heat transfer coefficient is higher for 1.0% alumina-pre-coated than for the 0.1% alumina-pre-coated wire. This phenomenon is most likely due to the fundamental trade-off in surface wettability and nucleation site density (discussed in Section 1.1). Figure 33 compares the surface morphology of 1.0% alumina-pre-coated nickel wire (a) to 0.1% alumina-pre-coated nickel wire (b). At higher nanoparticle concentrations, the nickel wire has a significantly thicker

coating. Although the increased coating thickness likely results in higher nucleation site density [32, 33], which translates into higher HTC, it reduces the capillary force available to rewet the wire surface and leads to a lower CHF.

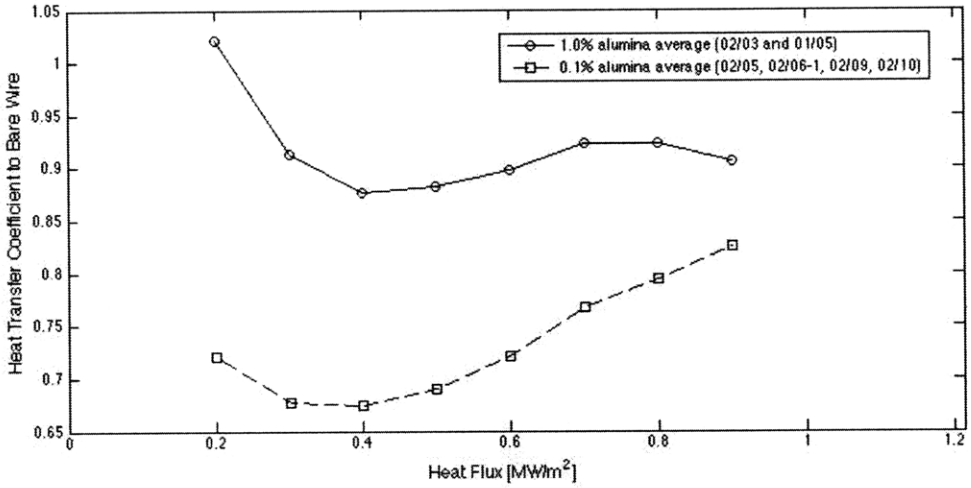

Figure 32: Heat transfer coefficient ratio to bare wire for 1.0% and 0.1% alumina nanofluid concentrations.

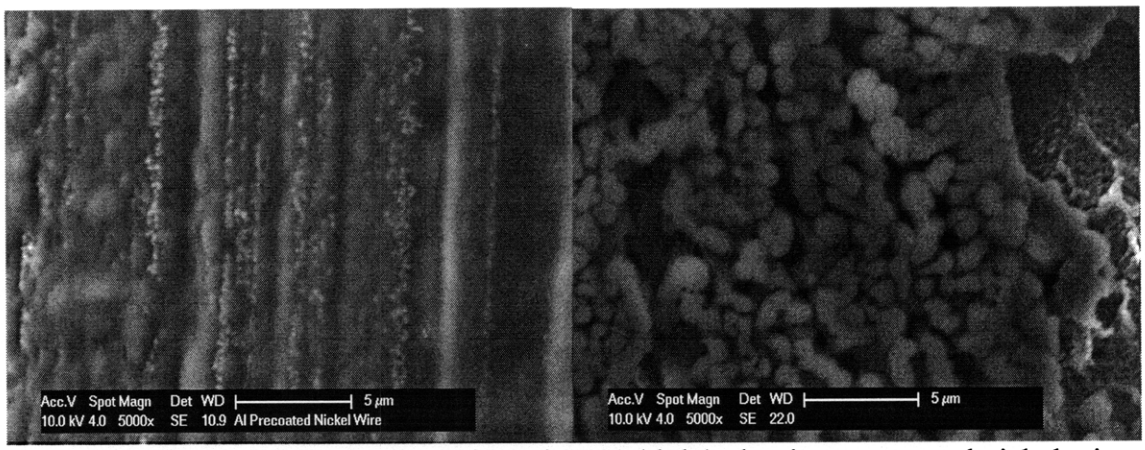

Figure 33: SEM images of 1.0% (left) and 0.1% (right) alumina-pre-coated nickel wires.

3 Alumina + PAH Experiments

3.1 Alumina and PAH Mixture Interactions

The goal of this experiment was to determine whether a mixture of alumina and PAH would be stable at room temperature and at water saturation temperature (100 °C). PAH is a polymer that was selected for the mixture experiments because of its stability with alumina nanofluid and its already extensive use in creating multilayer hydrophobic coatings. As a polymer, it was believed that PAH would improve adhesion between the alumina coating and nickel substrate. Although many thermal performance experiments have been performed using one type of nanoparticle, no published experiments to-date have used a mixture and it is therefore unclear how different types of nanoparticles interact. This experiment involved observing interactions between PAH and alumina in mixtures of various concentrations at room temperature and at water saturation temperature.

3.1.1 Experimental Procedure

- Prepare alumina nanofluid and PAH solution (0.1% and 1.0% by volume alumina nanofluid dilution procedures can be found in Table 2). Table 6 contains the PAH fluid composition for various concentrations.

Table 6: PAH fluid composition.

Concentration (ppm)	*PAH (g)*	*DI Water (mL)*
500	1	200
1000	2	200

- Prepare alumina and PAH mixtures according to Table 7.

Table 7: Alumina and PAH mixture compositions.

Sample	*1.0% Alumina (mL)*	*1000ppm PAH (mL)*
1	7.5	2.5
2	5	5
3	2.5	7.5

- Observe interactions at room temperature after approximately 1 day. This ensures long-term stability of the nanofluid mixture.
- Prepare PAH + alumina mixture using 100mL of 500ppm PAH and 300mL of 0.1% by volume alumina nanofluids.
- Heat to water saturation temperature (100 °C).
- Observe interactions.

3.1.2 Results

Table 8 contains the compositions and observations of various alumina and PAH mixtures. Visible settling did not occur in any of the samples. Similarly, agglomeration was not observed in the alumina + PAH mixture when heated to saturation temperature of 100 °C. The samples listed in Table 8 and an additional sample of 2.5mL 500ppm PAH and 7.5mL 0.1% alumina can be seen in Figure 34. It is therefore concluded that alumina nanofluids at 0.1 to 1.vol% are chemically compatible with PAH solutions from 500 to 1000ppm.

Table 8: Alumina + PAH mixture compositions and observations.

Sample	*1.0% Alumina (mL)*	*1000ppm PAH (mL)*	*Observations*
1	7.5	2.5	No visible settling
2	5.0	5.0	No visible settling
3	2.5	7.5	No visible settling

Figure 34: Alumina and PAH mixtures 3 months after initial preparation. As can be seen, no agglomeration, settling, or discoloration has occurred in these samples.

3.2 Effects of Alumina Nanoparticles and PAH Coating on Boiling HTC and CHF

The goal of this experiment was to determine how an alumina and PAH coating would affect the boiling HTC and CHF performance of the wire heater. As discussed previously, nanoparticle deposition significantly enhances CHF. However, it would be of interest to experimentally determine whether a composite coating with two materials of different chemical properties (i.e., metal oxide and polymer) would affect boiling heat transfer. This experiment involved pre-coating nickel wire with combined alumina and PAH dispersions using the boiling deposition method. Boiling deposition procedures are the same as those outlined in the previous section. The LbL method involves coating the wire surface with alternating layers of PAH and alumina nanoparticles. However, this method is relatively intensive and requires several steps,

which may not be practical for real-life situations. After pre-coating the wire, the CHF was found using the procedure outlined below.

3.2.1 Experimental Procedure

- Preparation: sand wire with 600-grid sandpaper and wipe down with acetone. Solder wire ends to electrodes in lid assembly. Solder voltage measurement leads to electrodes.
- Prepare alumina + PAH nanofluid with 200mL of 500ppm PAH and 600mL of 0.1% by volume alumina nanofluids.
- Put lid assembly into inner vessel filled with boiling prepared nanofluid.
- Attach current source to electrodes. Attach condenser to lid assembly.
- Connect thermocouple and voltage measurement leads to data acquisition system.
- Set heat flux to 0.5MW/m^2. Keep wire at this power in boiling nanofluid for 30 minutes.
- Visually inspect if coating exists.
- Follow procedure outlined in Section 2.1 to determine CHF.

3.2.2 Results

Figure 35 shows the boiling curve from the alumina + PAH-pre-coated wire experiment conducted on 01/07. In this experiment, the wire broke near the solder. A CHF value of 1.634 ± 0.109 MW/m^2 was observed.

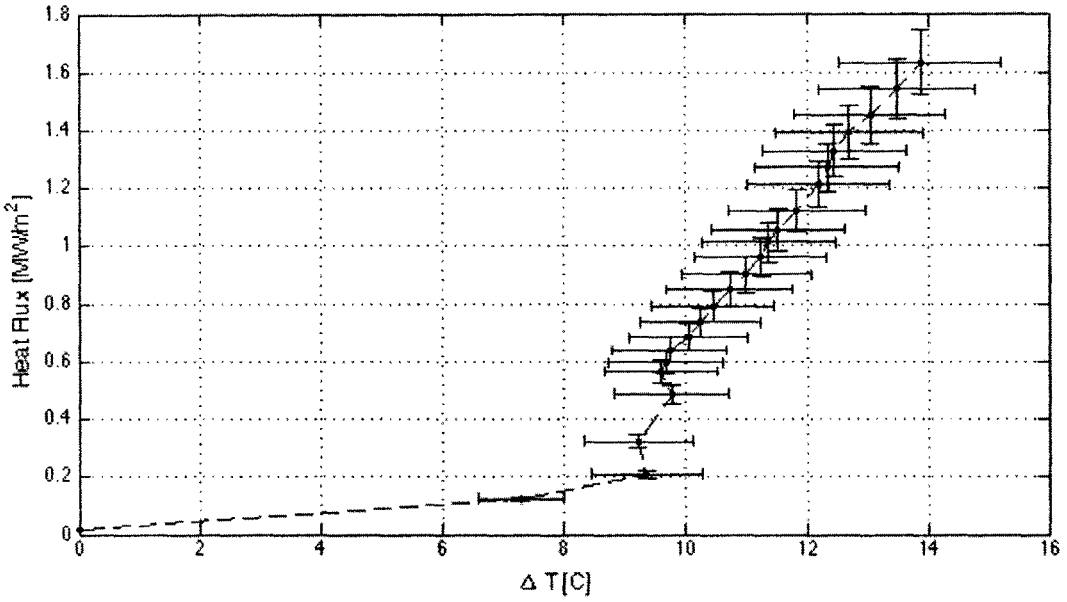

Figure 35: Boiling curve for alumina + PAH-pre-coated nickel wire in deionized water, 01/07 test 1. CHF occurred at 1.634 MW/m^2.

Figure 36 shows the boiling curve from the first alumina + PAH-pre-coated wire experiment conducted on 01/08. In this experiment, the wire broke near the solder. A CHF value of 1.405 ± 0.094 MW/m^2 was observed.

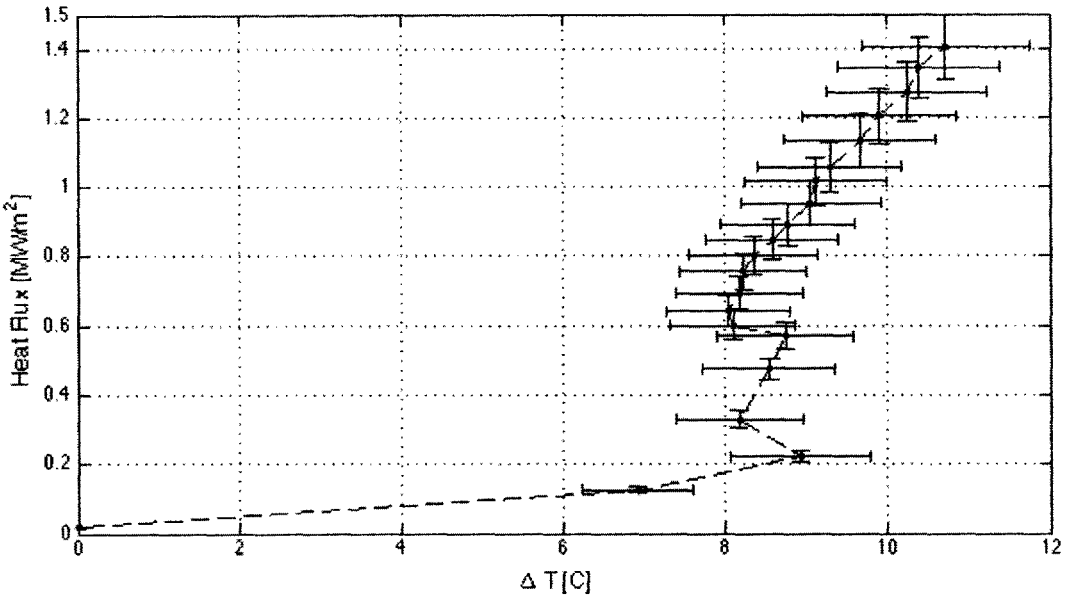

Figure 36: Boiling curve for alumina + PAH-pre-coated nickel wire in deionized water, 01/08 test 1. CHF occurred at 1.405 MW/m^2.

Figure 37 shows the boiling curve from the second alumina + PAH-pre-coated wire experiment conducted on 01/08. In this experiment, the wire broke at the solder. A CHF value of 1.404 ± 0.094 MW/m^2 was observed.

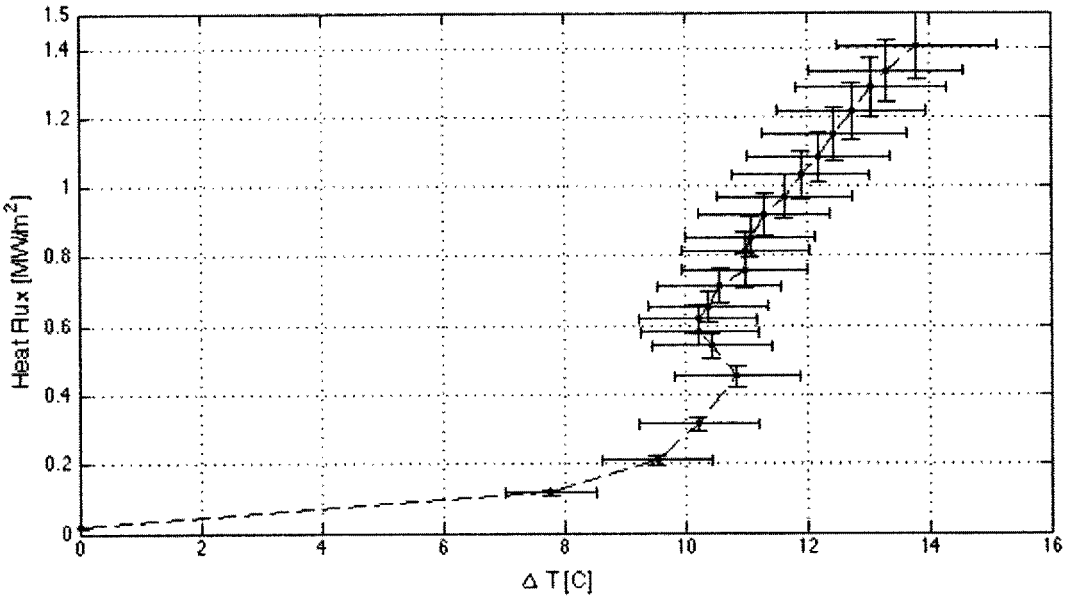

Figure 37: Boiling curve for alumina + PAH-pre-coated nickel wire in deionized water, 01/08 test 2. CHF occurred at 1.404 MW/m^2.

Figure 38 shows the boiling curve from the alumina + PAH-pre-coated wire experiment conducted on 01/09. In this experiment, the wire broke near the solder. A CHF value of 1.619 ± 0.108 MW/m^2 was observed.

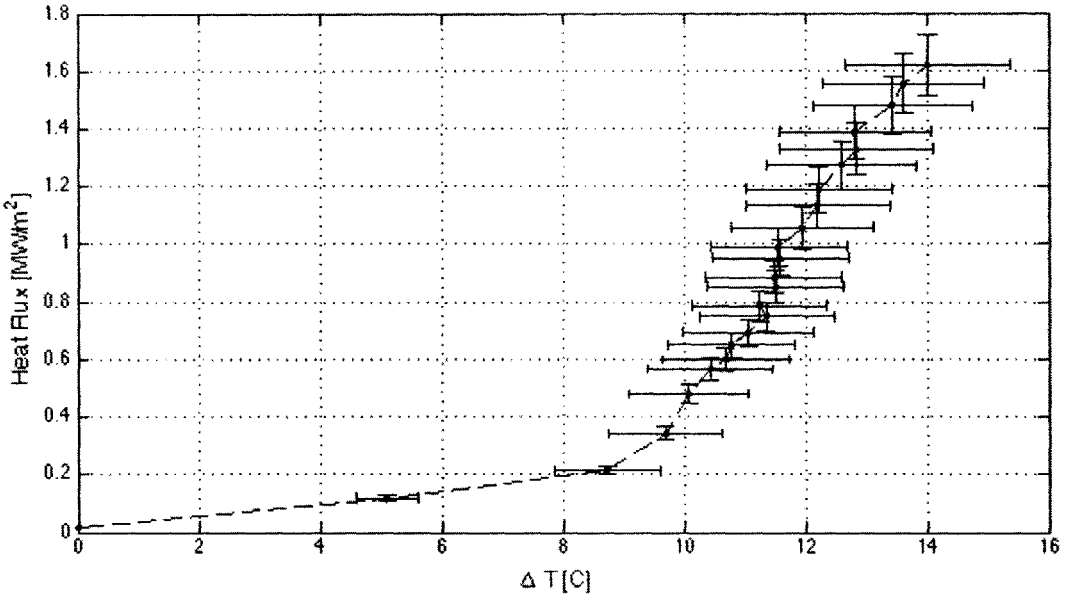

Figure 38: Boiling curve for alumina + PAH-pre-coated nickel wire in deionized water, 01/09 test 1. CHF occurred at 1.619 MW/m^2.

Figure 39 shows the boiling curve from the alumina + PAH-pre-coated wire experiment conducted on 01/12. In this experiment, the wire broke near the solder. A CHF value of 1.359 ± 0.091 MW/m^2 was observed.

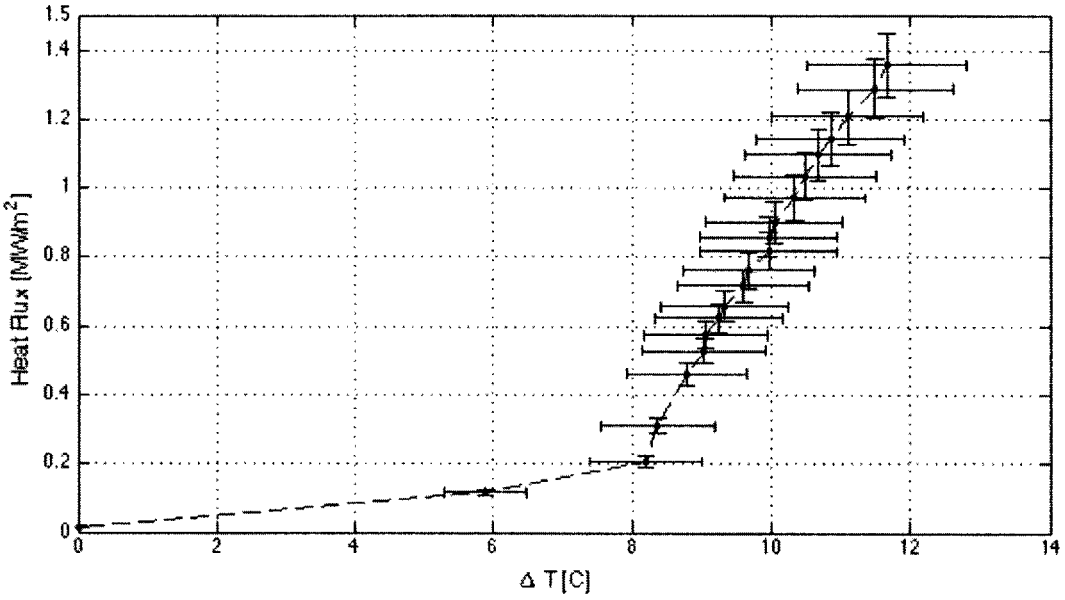

Figure 39: Boiling curve for alumina + PAH-pre-coated nickel wire in deionized water, 01/12 test 1. CHF occurred at 1.359 MW/m^2.

Figure 40 shows the boiling curve from the alumina + PAH-pre-coated wire experiment conducted on 01/14. In this experiment, the wire broke at the solder. A CHF value of 1.310 ± 0.087 MW/m^2 was observed.

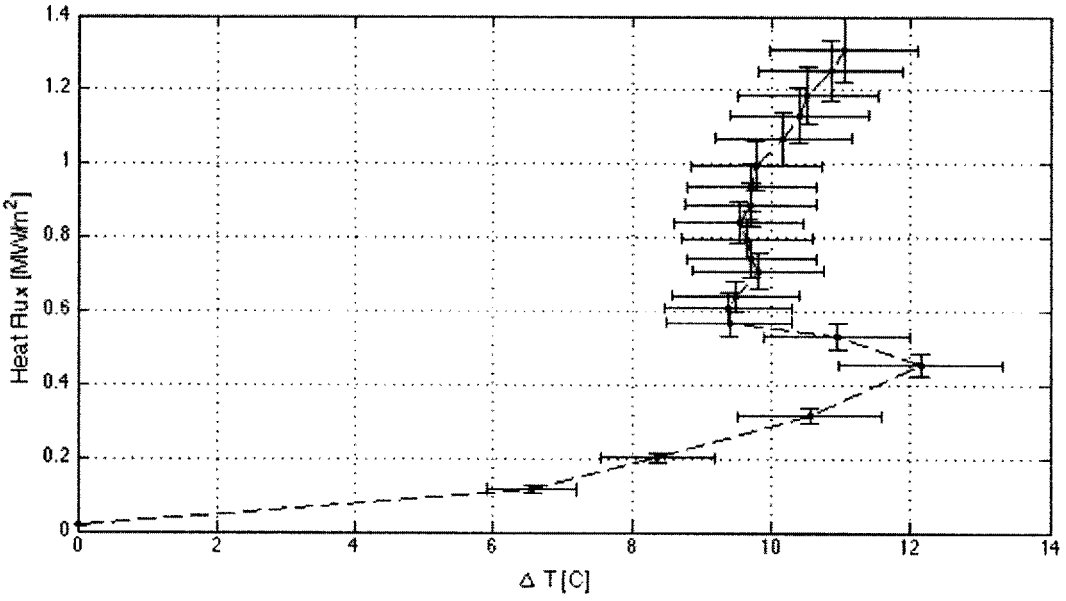

Figure 40: Boiling curve for alumina + PAH-pre-coated nickel wire in deionized water, 01/14 test 1. CHF occurred at 1.310 MW/m^2.

3.2.3 Analysis

Figure 41 shows the boiling curves for all alumina + PAH-pre-coated nickel wire experiments in deionized water. As can be seen in Figure 41, the CHF values for all experiments are relatively close. However, the experiments cover a wide range of temperature differences beyond the free convection region. The heat transfer coefficients, which are equal to q″/ΔT, in the nucleate boiling region also vary.

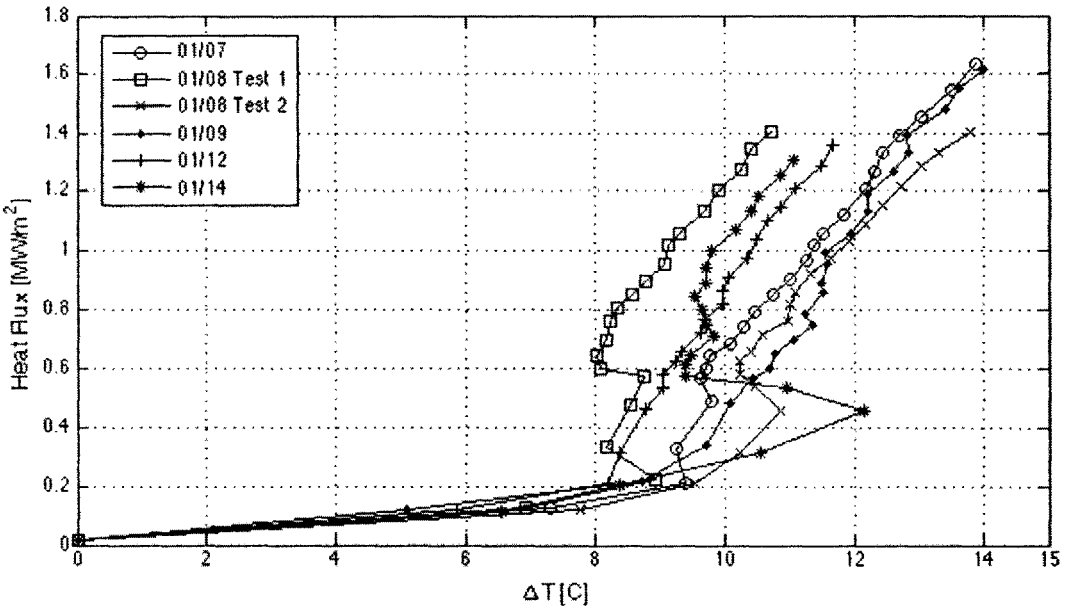

Figure 41: Boiling curves for alumina + PAH-pre-coated nickel wire in deionized water.

Table 9 contains the mixture concentrations and CHF data for the alumina + PAH experiments. No correlation was found between the mixture concentrations and the CHF due to the small variation in concentrations between experiments conducted on 01/07 and 01/08.

Table 9: Alumina + PAH mixture concentrations and CHF data.

Experiment	*Total Mixture Volume (mL)*	*PAH Concentration* (ppm)*	*Alumina Concentration* (%)*	*Coating Time (minutes)*	*CHF (MW/m^2)*
01/07	800	125.00	0.08	30	1.6340
01/08 Test 1	650	153.85	0.09	30	1.4046
01/08 Test 2	600	166.67	0.10	30	1.4040
01/09	800	125.00	0.08	30	1.6191
01/12	800	125.00	0.08	30	1.3586
01/14	800	125.00	0.08	30	1.3095

*These values assume a negligible loss of PAH and alumina particles due to coating.

Table 10 contains CHF values for the alumina + PAH-pre-coated wire experiments. As can be seen, the CHF values for the successful experiments are within 12% of the average value and have fairly close agreement considering coating inconsistencies inherent in boiling deposition. The average CHF ratio of the alumina + PAH-pre-coated wire to bare wire is 1.401 ± 0.069.

Table 10: CHF values for alumina + PAH-pre-coated wire in deionized water.

Test	*CHF (MW/m2)*	*CHF Error (MW/m2)*
01/07	1.634	0.109
01/08-1	1.405	0.094
01/09	1.619	0.108
01/12	1.359	0.091
01/14	1.310	0.087
Average*	1.465	0.044

*Average excludes CHF values for experiment 01/08-2 as explained in Appendix B.4.

Figure 42 shows the heat transfer coefficient as a function of heat flux for the successful alumina + PAH-pre-coated wire experiments. The values of the heat transfer coefficients are fairly consistent among the successful tests, and although error bars are omitted for visual clarity, all of the test values are within error range of the average values (see Figure B.4-2).

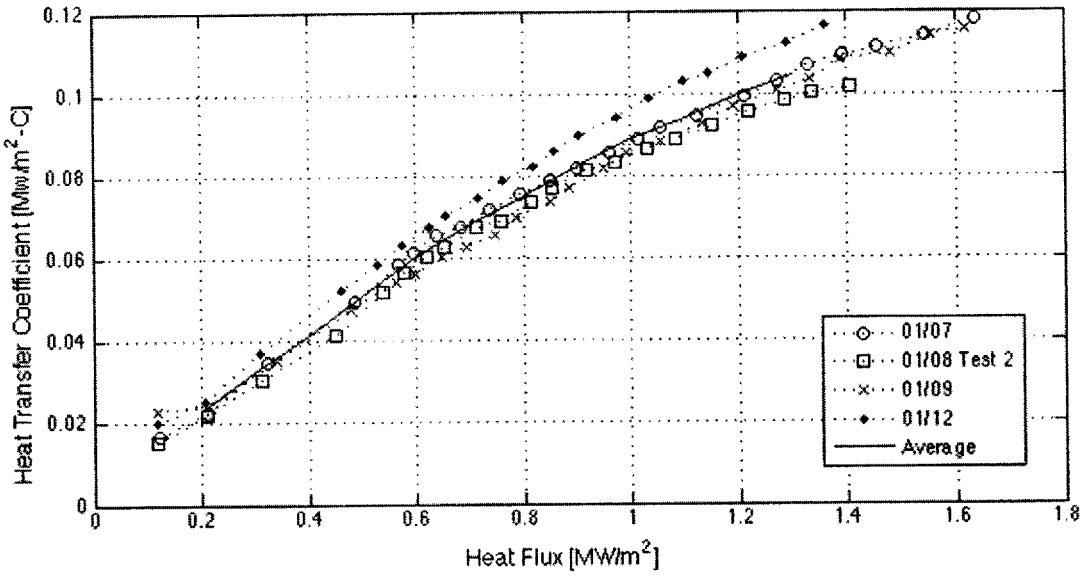

Figure 42: Heat transfer coefficients versus heat flux for alumina + PAH-pre-coated nickel wire in deionized water.

Figure 43 shows the ratio of the alumina + PAH-pre-coated nickel wire heat transfer coefficients to the average bare wire heat transfer coefficients at various heat fluxes. Although there is some variation in this ratio among the successful experiments, the ratio of the average alumina + PAH heat transfer coefficient values to the average bare wire HTC values is 0.996 ± 0.021. Therefore, the HTC of the alumina + PAH-pre-coated wires is not significantly different from the bare wire HTC.

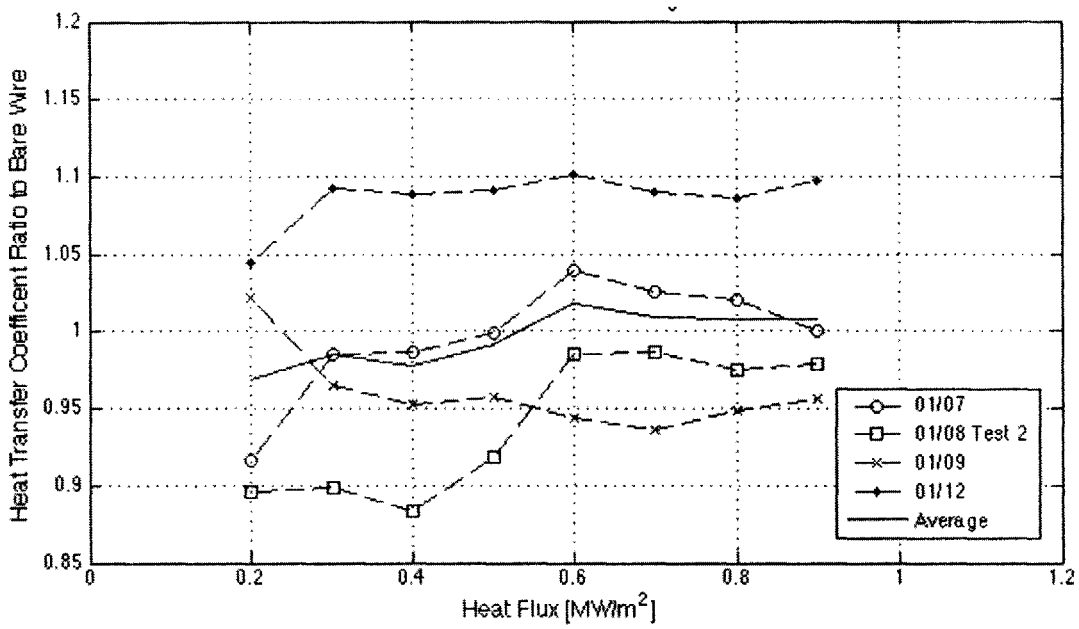

Figure 43: Ratio of alumina + PAH-pre-coated nickel wire heat transfer coefficients to the average bare wire heat transfer coefficients.

Figure 44 illustrates the surface morphology of the alumina + PAH-pre-coated nickel wire at 250, 1000, and 5000 times (x) magnification using SEM imaging (clockwise from upper left). The fourth image shows the coating composition determined by EDS. As can be seen from the EDS graph, the nickel wire is minimally coated by the alumina + PAH mixture. The PAH concentration used in the mixture was very low (only 125ppm PAH), and therefore the chemical compositions of the PAH has an insignificant presence in the EDS graph due to the imprecision of the EDS measurements.

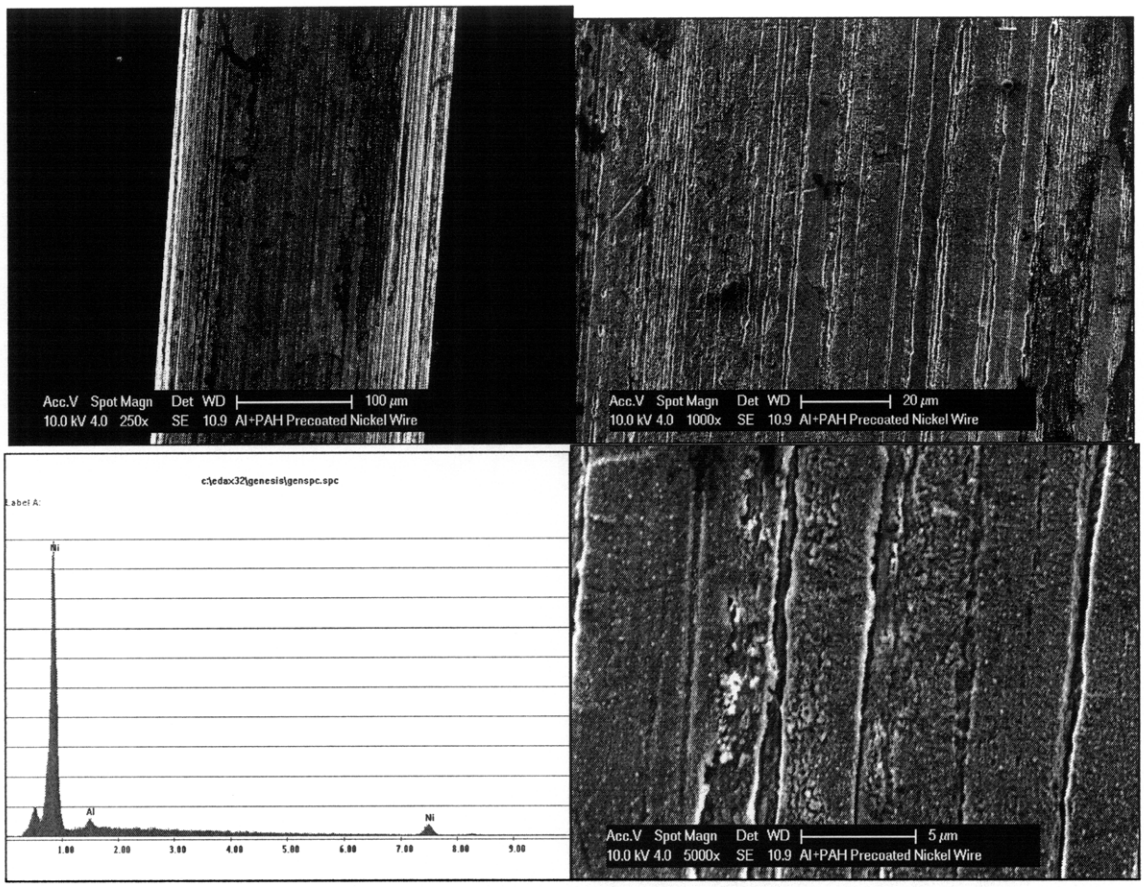

Figure 44: Alumina + PAH-pre-coated wire surface morphology and material composition. Clockwise from top left: 250x, 1000x, 5000x, and EDS data taken after 1000x SEM.

3.3 Effects of PAH Coating on Boiling HTC and CHF

The goal of this experiment was to determine how a PAH coating would affect the boiling HTC and CHF performance of the wire heater. As discussed previously, nanoparticle deposition significantly enhances CHF. However, it is unclear what effect PAH will have on boiling HTC and CHF performance. This experiment involved pre-coating nickel wire with PAH using the boiling deposition method. In total, ten experiments were conducted with PAH-coated nickel wires in deionized water.

3.3.1 Experimental Procedure

- Preparation: sand wire with 600-grid sandpaper and wipe down with acetone. Solder wire ends to electrodes in lid assembly. Solder thermocouple to electrodes.
- Prepare 800mL PAH nanofluid with the following composition:

Table 11: PAH nanofluid composition.

Composition	*DI Water (mL)*	*PAH (g)*
500ppm PAH	800	4

- Put lid assembly into inner vessel filled with boiling prepared nanofluid.
- Attach current source to electrodes.
- Connect thermocouple and voltage measurement leads to data acquisition system.
- Set heat flux to 0.5MW/m^2. Keep wire at this heat flux in boiling nanofluid for 30 minutes.
- Visually estimate if coating is sufficient to significantly affect CHF performance.
- Follow procedure outlined in Section 2.1 to determine CHF.

3.3.2 Results

Figure 45 shows the boiling curve from the PAH-pre-coated wire experiment conducted on 01/20. In this experiment, the wire broke at the solder. A CHF value of 0.980 ± 0.066 MW/m^2 was observed.

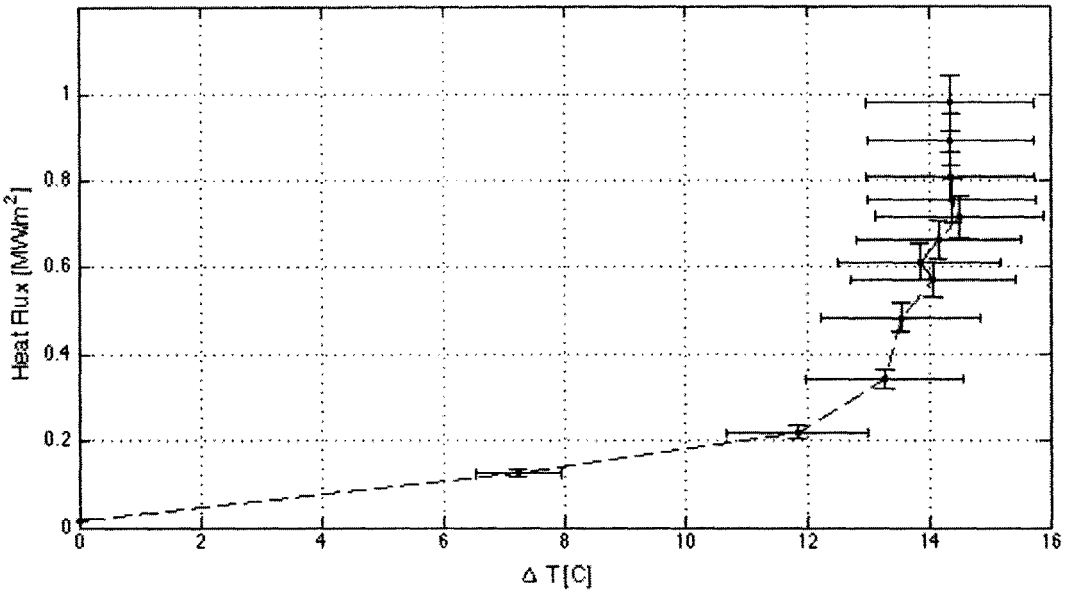

Figure 45: Boiling curve for PAH-pre-coated nickel wire in deionized water, 01/20 test 1. CHF occurred at 0.980 MW/m^2.

Figure 46 shows the boiling curve from the first PAH-pre-coated wire experiment conducted on 01/22. In this experiment, the wire broke near the solder. A CHF value of 0.967 ± 0.065 MW/m^2 was observed.

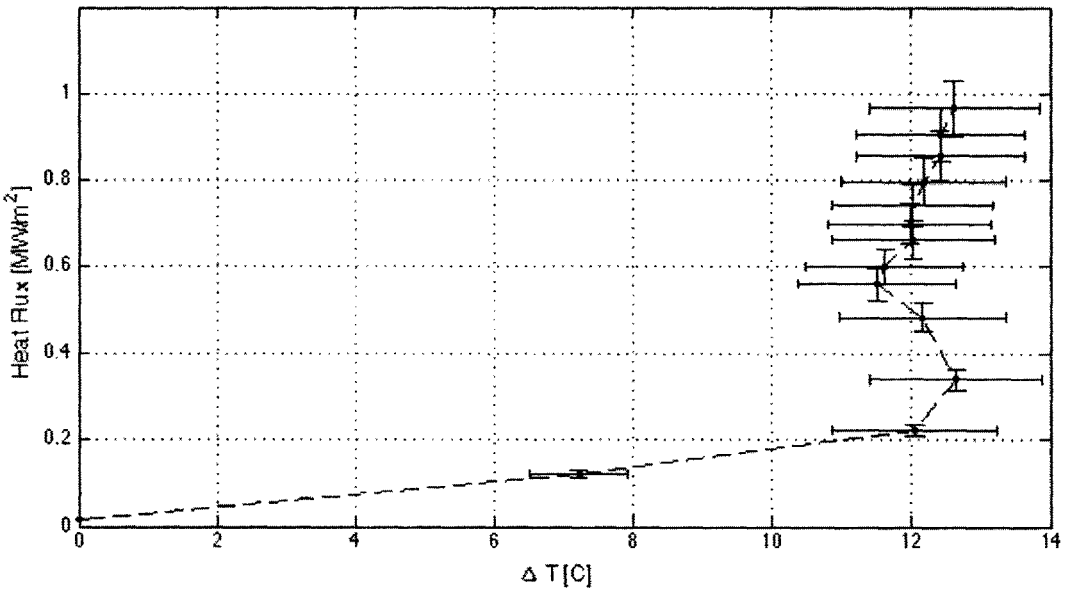

Figure 46: Boiling curve for PAH-pre-coated nickel wire in deionized water, 01/22 test 1. CHF occurred at 0.967 MW/m^2.

Figure 47 shows the boiling curve from the second PAH-pre-coated wire experiment conducted on 01/22. In this experiment, the wire broke near the solder. A CHF value of 1.109 ± 0.074 MW/m^2 was observed.

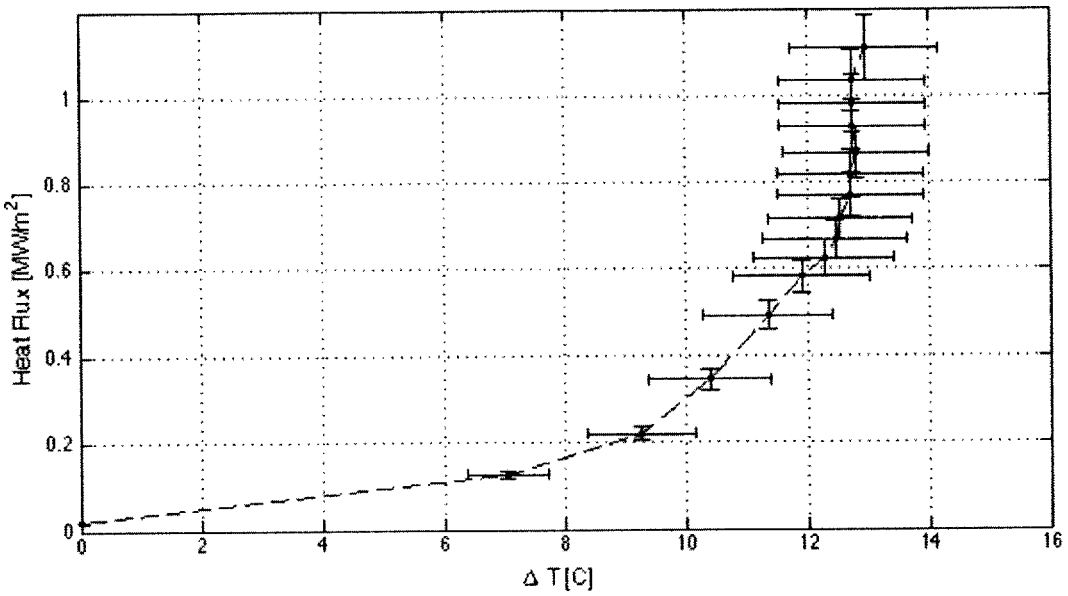

Figure 47: Boiling curve for PAH-pre-coated nickel wire in deionized water, 01/22 test 2. CHF occurred at 1.109 MW/m^2.

Figure 48 shows the boiling curve from the PAH-pre-coated wire experiment conducted on 01/23. In this experiment, the wire broke near the center. A CHF value of 1.242 ± 0.083 MW/m^2 was observed.

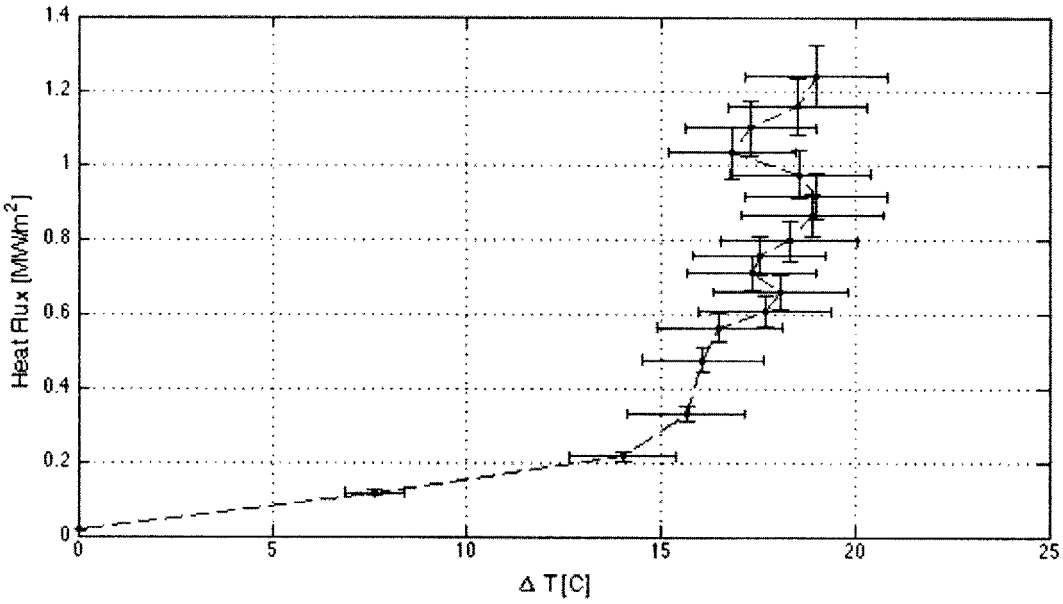

Figure 48: Boiling curve for PAH-pre-coated nickel wire in deionized water, 01/23 test 1. CHF occurred at 1.242 MW/m^2.

Figure 49 shows the boiling curve from the PAH-pre-coated wire experiment conducted on 02/19. In this experiment, the wire broke near the solder. A CHF value of 1.254 ± 0.084 MW/m^2 was observed.

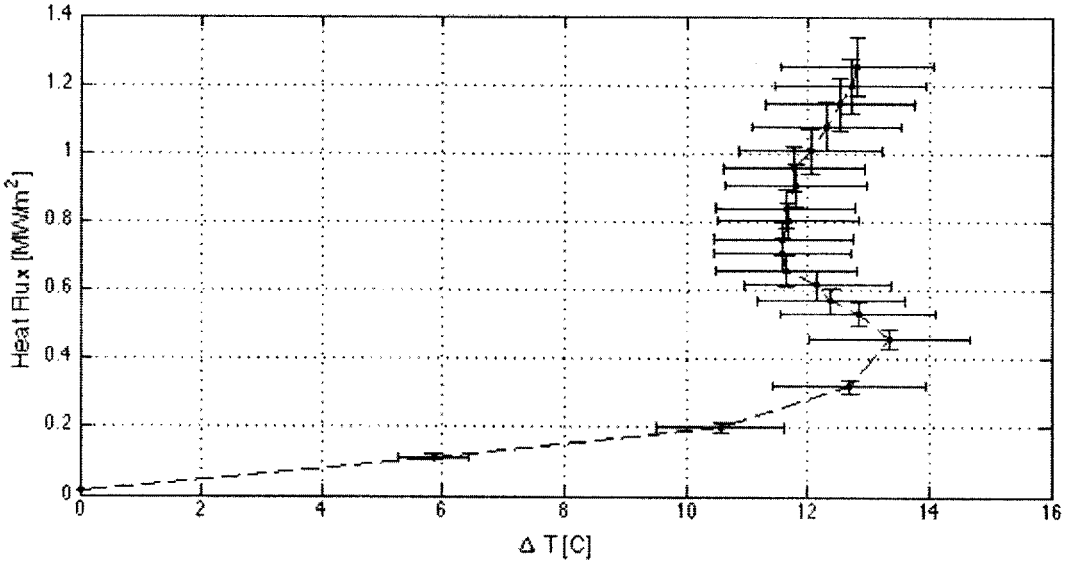

Figure 49: Boiling curve for PAH-pre-coated nickel wire in deionized water, 02/19 test 1. CHF occurred at 1.254 MW/m^2.

Figure 50 shows the boiling curve from the PAH-pre-coated wire experiment conducted on 02/24. In this experiment, the wire broke near the solder. A CHF value of 1.263 ± 0.084

MW/m^2 was observed.

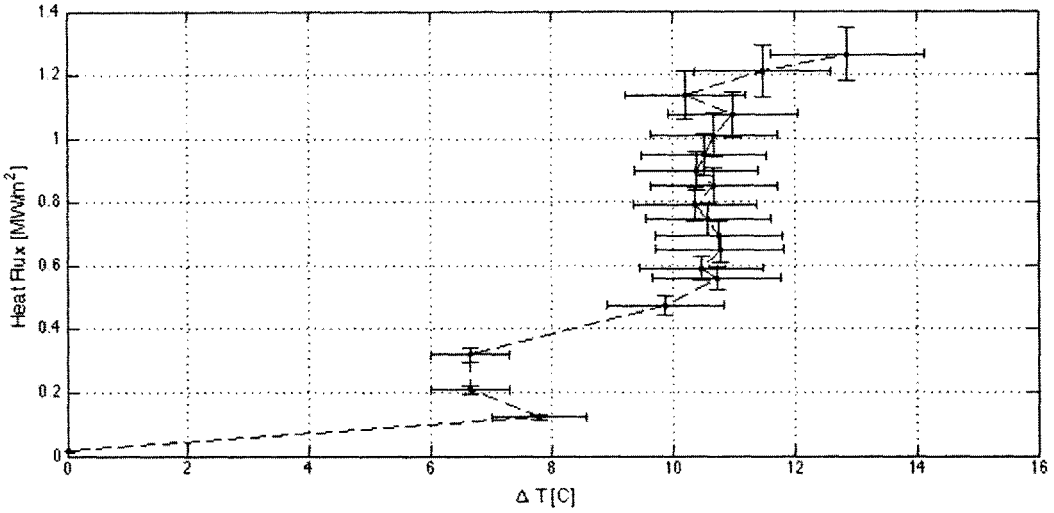

Figure 50: Boiling curve for PAH-pre-coated nickel wire in deionized water, 02/24 test 1. CHF occurred at 1.263 MW/m^2.

Figure 51 shows the boiling curve from the first PAH-pre-coated wire experiment conducted on 03/03. In this experiment, the wire broke near the solder. A CHF value of 0.846 ± 0.057 MW/m^2 was observed.

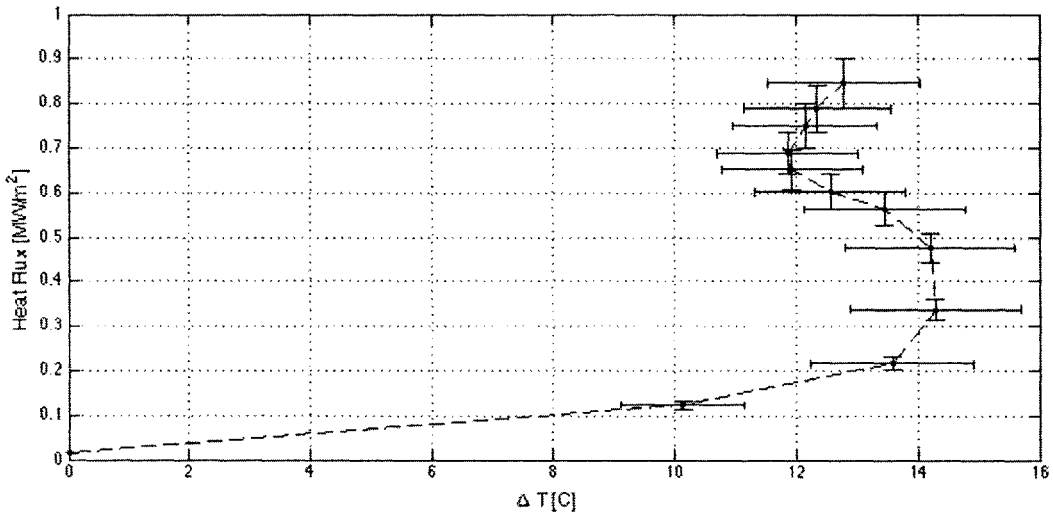

Figure 51: Boiling curve for PAH-pre-coated nickel wire in deionized water, 03/03 test 1. CHF occurred at 0.846 MW/m^2.

Figure 52 shows the boiling curve from the second PAH-pre-coated wire experiment conducted on 03/03. In this experiment, the wire broke near the solder. A CHF value of

1.030 ± 0.069 MW/m^2 was observed.

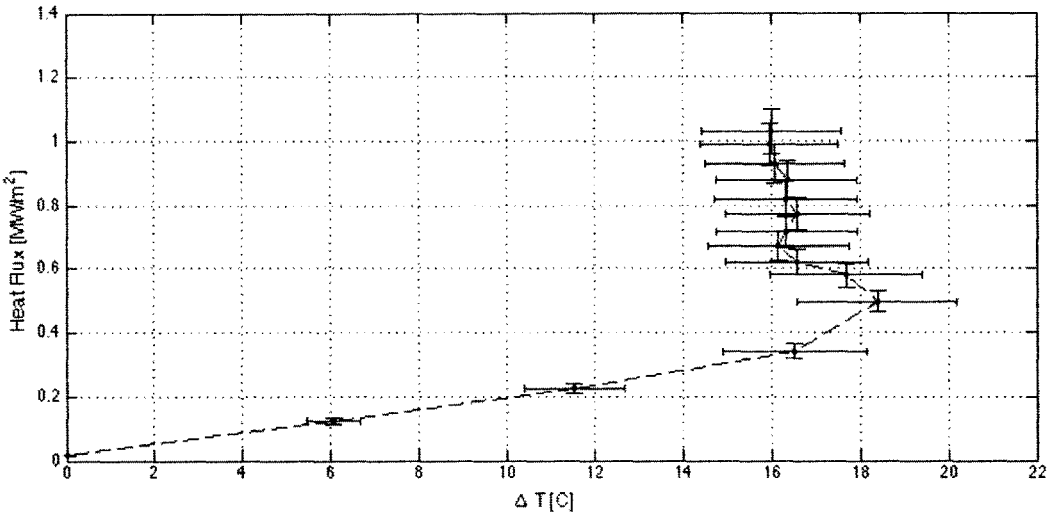

Figure 52: Boiling curve for PAH-pre-coated nickel wire in deionized water, 03/03 test 2. CHF occurred at 1.030 MW/m^2.

3.3.3 Analysis

Figure 53 shows the boiling curves for all PAH-pre-coated nickel wire experiments in deionized water. As can be seen in Figure 66, the CHF values for all experiments are relatively close. However, the experiments cover a wide range of temperature differences beyond the free convection region. The heat transfer coefficients, which are equal to $q''/\Delta T$, in the nucleate boiling region also vary.

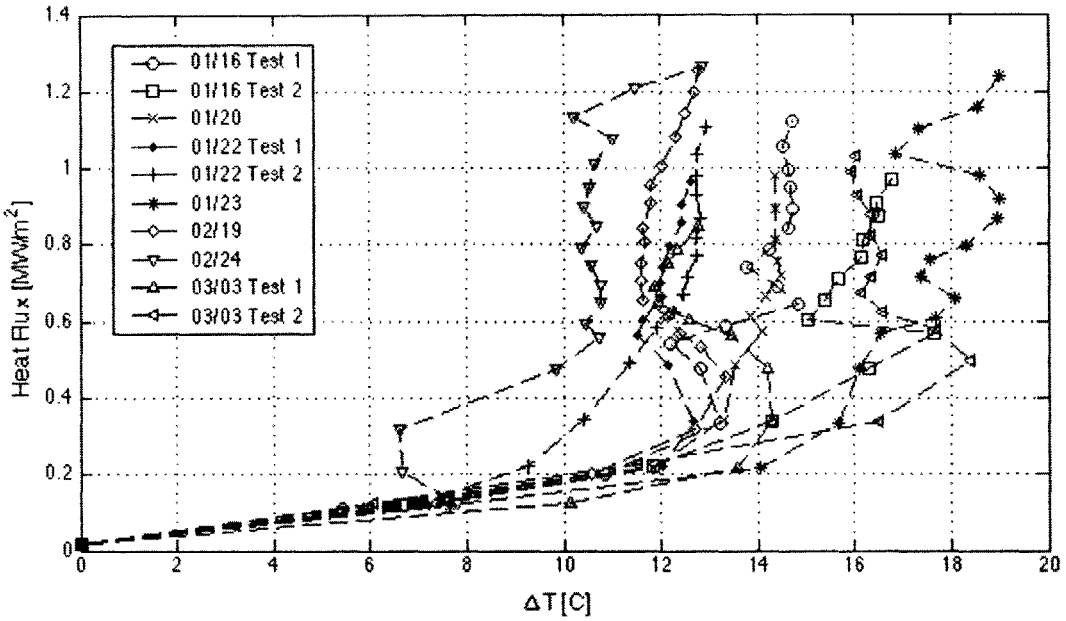

Figure 53: Boiling curves for PAH-pre-coated nickel wire in deionized water.

Table 12 contains CHF values for the PAH-pre-coated wire experiments. As can be seen, the CHF values for these experiments are within 30% of the average value and have fairly close agreement considering coating inconsistencies inherent in boiling deposition. The average CHF ratio of the PAH-pre-coated wire to bare wire is 1.052 ± 0.050.

Table 12: CHF values for PAH-pre-coated wire in deionized water.

Test	*CHF (MW/m^2)*	*CHF Error (MW/m^2)*
01/22-1	0.967	0.065
01/23	1.242	0.083
02/19	1.254	0.084
02/24	1.263	0.084
03/03-1	0.846	0.057
03/03-2	1.030	0.069
Average*	1.100	0.030

*Average excludes CHF values from 01/16, 01/20, and 01/22 test 2 as explained in Appendix B.5.

Figure 54 shows the heat transfer coefficient as a function of heat flux for the successful PAH-pre-coated wire experiments. The values of the heat transfer coefficients are fairly consistent among the successful tests, and although error bars are omitted for visual clarity, all of the test values are within error range of the average values (see Figure B.5-4).

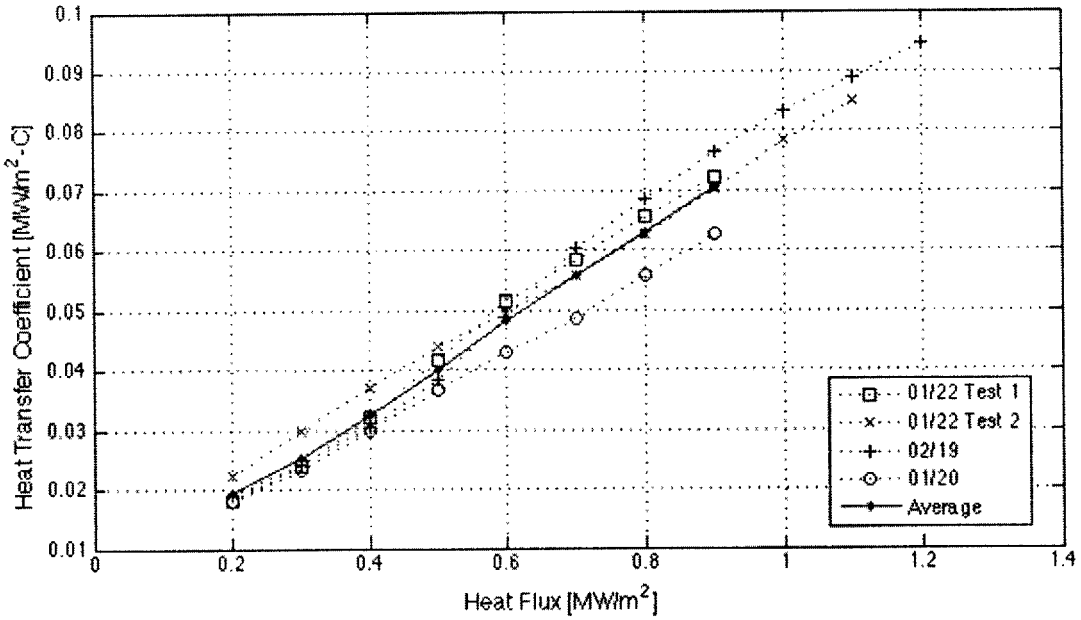

Figure 54: Heat transfer coefficients versus heat flux for PAH-pre-coated nickel wire in deionized water.

Figure 55 shows the ratio of the PAH-pre-coated nickel wire heat transfer coefficients to the average bare wire heat transfer coefficients at various heat fluxes. Although there is some variation in this ratio among the successful experiments, the ratio of the average PAH heat transfer coefficient values to the average bare wire HTC values is 0.810 ± 0.026.

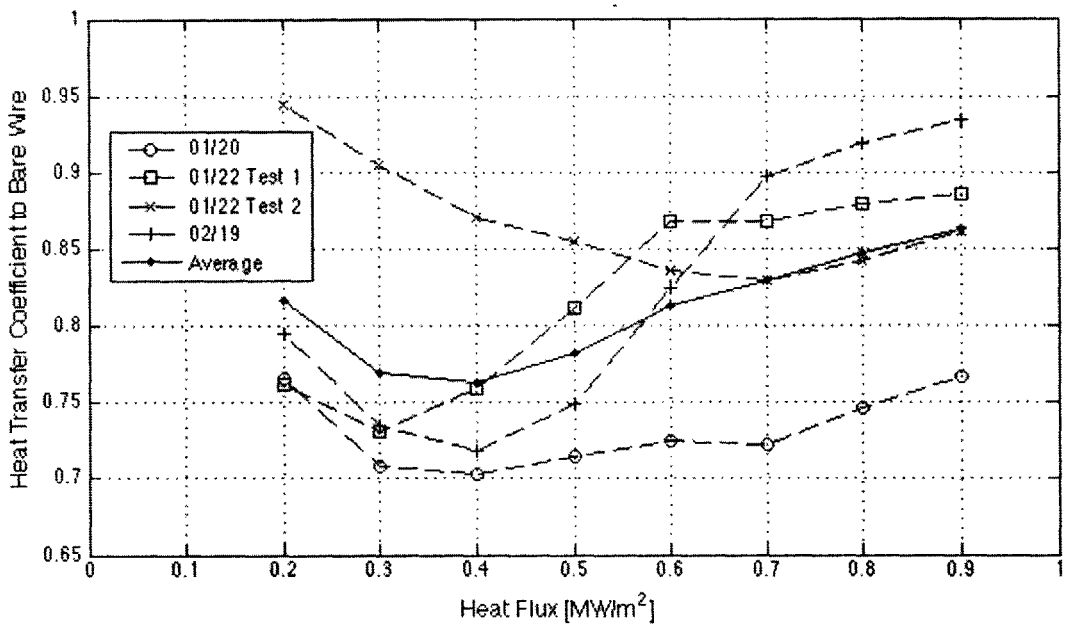

Figure 55: Ratio of PAH-pre-coated nickel wire heat transfer coefficients to the average bare wire heat transfer coefficients.

Figure 56 illustrates the surface morphology of PAH-pre-coated nickel wire at 250, 1000, and 5000x magnifications using SEM imaging (clockwise from upper left). The fourth image shows the coating composition determined by EDS. As can be seen from the EDS graph, the nickel wire is minimally coated with chlorine, which is expected due to the chemical composition of PAH. Note that at a concentration of 500ppm PAH, the chlorine peak is almost negligible. For a concentration of 125ppm PAH, there was no chlorine peak at all (Figure 44).

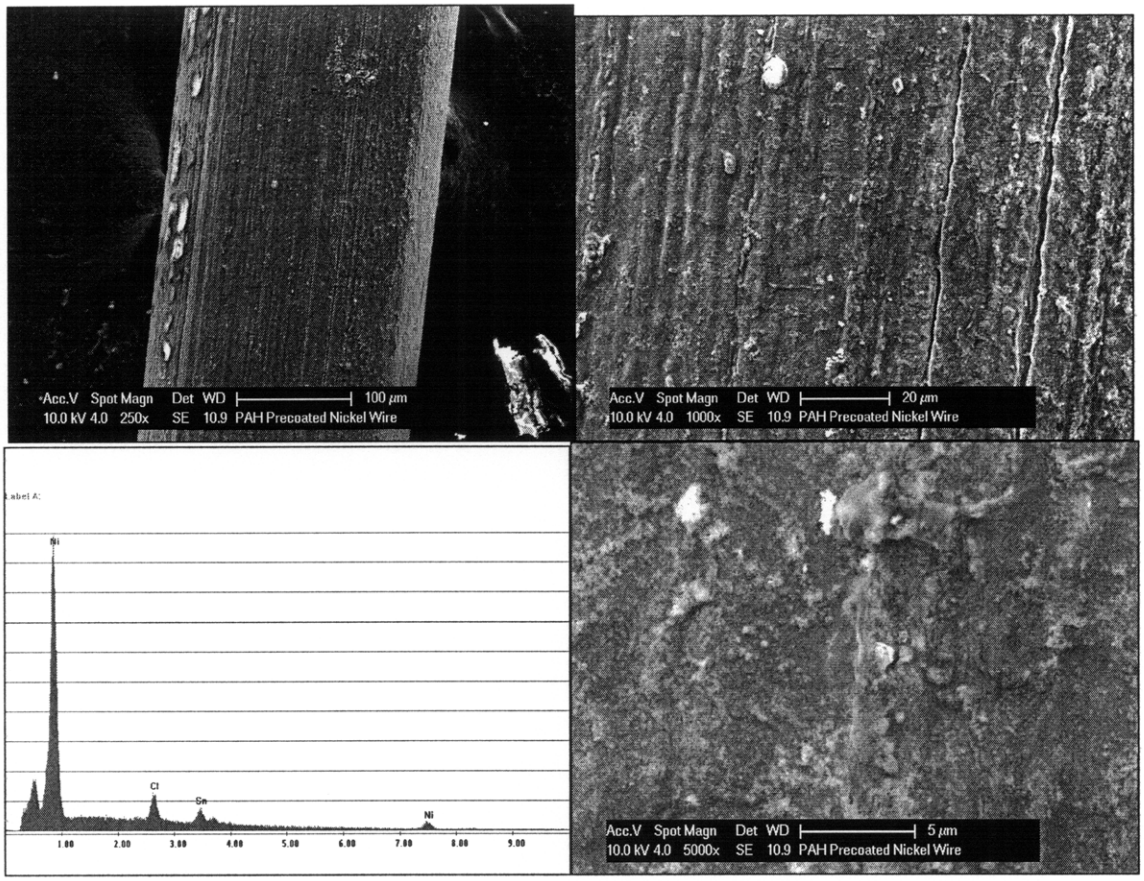

Figure 56: 500ppm PAH-pre-coated wire surface morphology and material composition. Clockwise from top left: 250x, 1000x, 5000x, and EDS data taken after 5000x SEM. The EDS indicates the wire is not completely coated with PAH.

4 Comparison of Alumina, PAH, and Alumina + PAH Coating Heat Transfer Performance

Table 13 contains a summary of the average CHF values of the bare and pre-coated wires and the CHF ratios over the bare wire case. Compared to wires coated with pure alumina (1.329MW/m^2 for 1.0% alumina and 1.429MW/m^2 for 0.1% alumina) or pure PAH (1.100MW/m^2 for 500ppm), wires coated with the combined nanoparticle-polymeric dispersion of alumina + PAH have a higher CHF (1.465MW/m^2 for alumina and PAH).

However, the average CHF of the combined dispersion pre-coated wire is not significantly higher than that of the 0.1% alumina-pre-coated wire given the associated instrumentation and experimental errors. To verify the improved CHF enhancement due to the combined polymeric dispersion coating, more experiments must be conducted.

Table 13: Average CHF values and CHF ratio to bare wire for various coatings.

Coating	*Average CHF (MW/m^2)*	*Average CHF Ratio to Bare Wire*
None	1.046 ± 0.077	N/A
1.0% alumina	1.329 ± 0.051	1.271 ± 0.069
0.1% alumina	1.429 ± 0.036	1.366 ± 0.064
0.1% alumina + 500ppm PAH	1.465 ± 0.044	1.401 ± 0.069
500ppm PAH	1.100 ± 0.030	1.052 ± 0.050

A more obvious thermal performance enhancement due to the combined nanoparticle-polymeric dispersion coating is the improvement in the HTC compared to the HTC for wires pre-coated with a single particle nanofluid. Figure 57 illustrates the average heat transfer coefficients for bare wire and 1.0% alumina, 0.1% alumina, 0.1% alumina and 500ppm PAH, and 500ppm PAH-pre-coated wires (this same figure with error bars is Figure A.2-1). As can be seen in Figure 57, the average HTC values for the bare and alumina + PAH-pre-coated wires are relatively close.

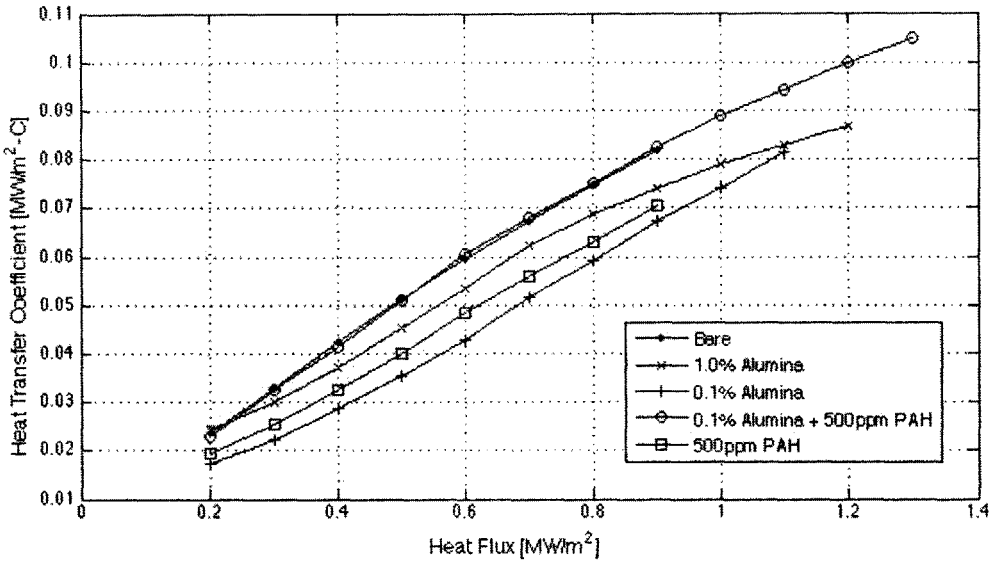

Figure 57: Average heat transfer coefficients for bare and coated wires.

This closeness is especially apparent in Figure 58, which shows the ratio of the pre-coated wire average HTC to the bare wire average HTC at various heat fluxes. The red line represents a ratio of unity. The ratio for the alumina + PAH coating in Figure 58 fairly closely follows this red line, indicating that the HTC for the alumina + PAH coating is roughly equivalent to that of the bare wire. All other coatings cause a significant decrease in the HTC due to mechanisms discussed in Section 1.

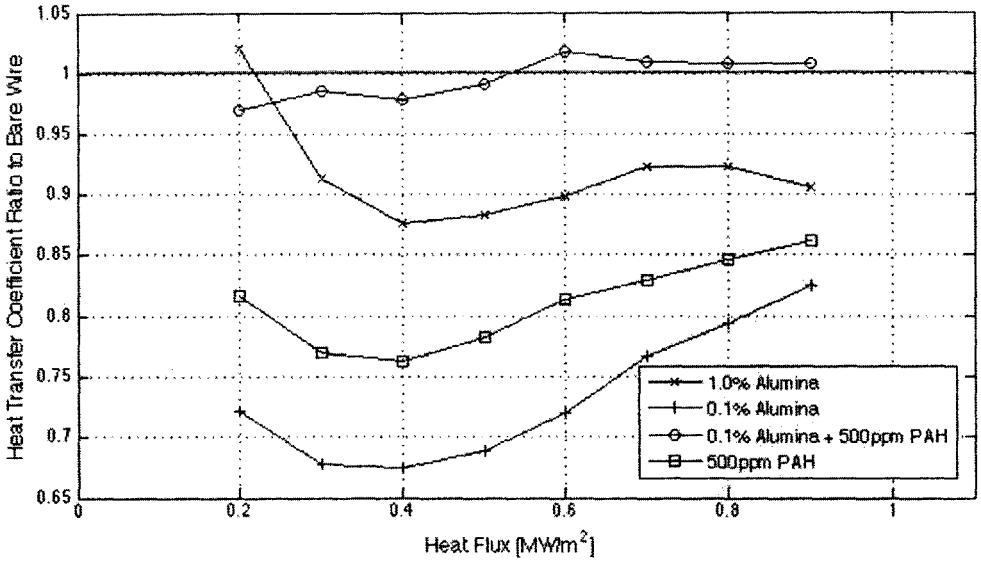

Figure 58: Average heat transfer coefficient ratios to bare wire for various coatings. The red line indicates a ratio of one to the bare wire HTC.

Table 14 contains the average HTC ratio of coated wire to bare wire. The average HTC ratio of the combined dispersion pre-coated wire to bare wire is significantly higher than that of even the 1.0% alumina-pre-coated wire given the associated instrumentation and experimental errors (a ratio of 0.996 ± 0.021 for the alumina-PAH mixture compared to 0.917 ± 0.026 for 1.0% alumina). Both the 0.1% alumina and 500ppm PAH coatings degrade the average wire HTC by more than 18%.

Table 14: Average HTC ratios of various coatings to bare wire.

Coating	*Average HTC Ratio to Bare Wire**
None	N/A
1.0% alumina	0.917 ± 0.026
0.1% alumina	0.734 ± 0.019
0.1% alumina + 500ppm PAH	0.996 ± 0.021
500ppm PAH	0.810 ± 0.026

*These values were found by taking the ratio of the coated wire heat transfer coefficient to the bare wire heat transfer coefficient at heat fluxes of 0 to 2 MW/m^2 in steps of 0.1 MW/m^2. The percentages were then averaged over the entire range of heat flux values.

5 Adhesion Tests

The goal of this experiment was to determine whether polymeric dispersion would improve adhesion of the alumina nanoparticles to the wire surface. As discussed in Section 1, improving nanoparticle adhesion could provide long-term CHF enhancement. This experiment involved evaluating the surface adhesion of the nanoparticle deposition both qualitatively and quantitatively. First, the surface was examined using a scanning electron microscope (SEM) to observe whether the nanoparticle coating adheres to the wire surface. Second, tape and modified bend tests were used to determine more quantitatively when the coatings begin to crack.

5.1 Experimental Procedure

Both tape and bend tests were conducted on the coated wire. The procedure for both of these testing methods is outlined below.

Tape Test

- Pre-coat one wire for each of the coating materials (alumina, alumina + PAH, and PAH) using the procedures outlined in the preceding sections.
- Lay dry pre-coated wire on a clean, flat surface and apply tape perpendicular to the wire with an even and consistent force. Peel tape off at a constant rate. For preliminary tape tests, Scotch tape was used. For subsequent tape tests, Scotch® Transparent Tape 174 was used (the ASTM recommends using pressure sensitive tape [45], but transparent tape is sufficient for qualitative adhesion testing).
- Compare the coating on the stripped section to the coating on other sections of the wire using SEM.

Modified Bending Test

- Pre-coat 3-6 wires for each coating material (alumina and alumina + PAH) using the

procedures outlined in the preceding sections.

- Bend one dry wire of each coating type over a cylindrical rod with a consistent and even force until the wire is wrapped 180 degrees around the rod with the wire center at the apex of the rod (90 degrees from the horizontal). For preliminary bend tests, diameters of 3 1/2", 10 11/32", and 11 11/32" were used. For subsequent bend tests, diameters of 10 11/32" and 11 11/32" were used.
- Visually examine the wire using SEM to determine if cracking or spallation of the coating has occurred.

Preliminary tape and bend tests were conducted to ensure the tape and bend test methods would give visible results of coating adhesion strength. Therefore, these preliminary tests were not rigorously conducted. The results from the preliminary tests were used to specify the final testing methods.

The rod diameters used in this experiment were calculated from the ultimate tensile strength of bulk alumina. The bulk properties of alumina were used as an upper bound to help initially size the rods used in the modified bend test. An alumina coating is expected to fail at bend radii much greater than the calculated value because of the weak interfacial bonding discussed in Section 1.2.3. Table 15 contains the room-temperature mechanical properties used in the stress/strain calculations for alumina and annealed nickel.

Table 15: Mechanical properties for bulk alumina and annealed nickel at room temperature [31].

	Alumina	*Annealed Nickel*
Ultimate Tensile Strength (MPa)	300	45
Young's Modulus (GPa)	370	207

The failure strain of alumina was found using the following relationship:

$$\varepsilon_{Al_2O_3,failure} = \frac{\sigma_{Al_2O_3,YS}}{E_{Al_2O_3}}, \qquad (16)$$

with $\sigma_{Al2O3,YS}$ equal to the yield strength of alumina and E_{Al2O3} equal to the Young's modulus of alumina. The ultimate tensile strength instead of the yield strength is used to determine the failure strain because alumina is a ceramic and therefore does not plastically deform, meaning the ultimate tensile strength and yield strength are equivalent (unlike the PAH coating, which does plastically deform) [40].[4] The failure strain for alumina was found to be 8.108×10^{-4} (dimensionless). The failure strain was then used to calculate the rod radius required to fail the alumina coating using the following relationship:

$$R_{rod,failure} = \frac{r_{wire}}{\varepsilon_{Al_2O_3,failure}} - r_{wire} - \delta_c \qquad (17)$$

with all variables previously defined [30]. $R_{rod,failure}$ was calculated to be 136mm (13.6cm or 10 3/5″ inches). Table 16 contains the strain and stress corresponding to different rod diameters used in the modified bend tests. As a reference for comparison in the final tape and bend tests, Figures 59 and 60 show original coatings of 0.1% alumina and 0.1% alumina + 500ppm PAH, respectively.

[4] Note that the failure strain of PAH was not calculated due to limited information on PAH mechanical properties. PAH is typically used in combination with other substances (polymers or inorganic particles), and existing information focuses on the mechanical properties of these various combinations [41, 42, 43]. For combined polystyrene sulfonate (PSS) and PAH, the Young's modulus is on the order of 100MPa [42, 43]. A summary of Young's moduli for various combinations can be found in Ref. [44]. The ultimate tensile strength of a typical LbL film with PAH and a polymer or inorganic particle is on the order of 40-70 MPa [45] with a record of 220GPa with carbon nanotube reinforcement [44, 45].

Table 16: Interfacial strain and stress between the alumina and nickel wire corresponding to rod radii used in bend tests.

Bend Test	*Rod Diameter (mm)*	*Strain* ($x10^{-4}$)*	*Stress on Alumina (MPa)*
1 - 3 1/2"	88.900	24.682 ± 3.459	913.3 ± 128.0
2 - 10 11/32"	262.731	8.366 ± 0.818	309.6 ± 30.3
3 - 11 11/32"	288.131	7.629 ± 0.737	282.3 ± 27.3

*The failure strain of alumina was found to be 8.108×10^{-4}.

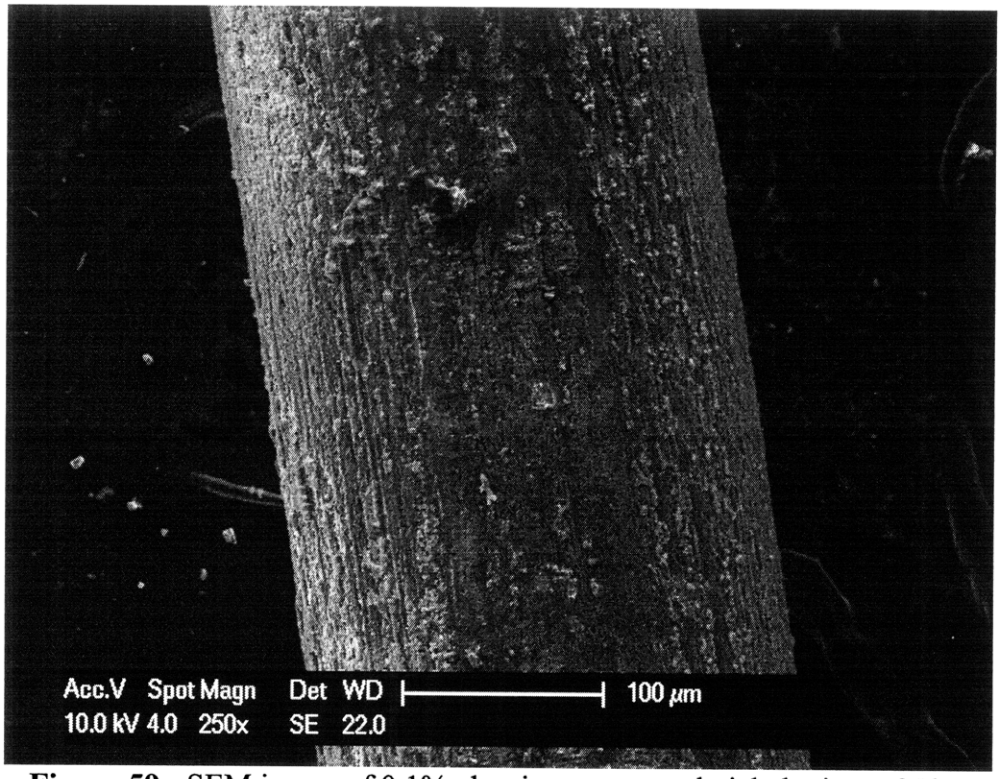

Figure 59: SEM image of 0.1% alumina pre-coated nickel wire at 250x.

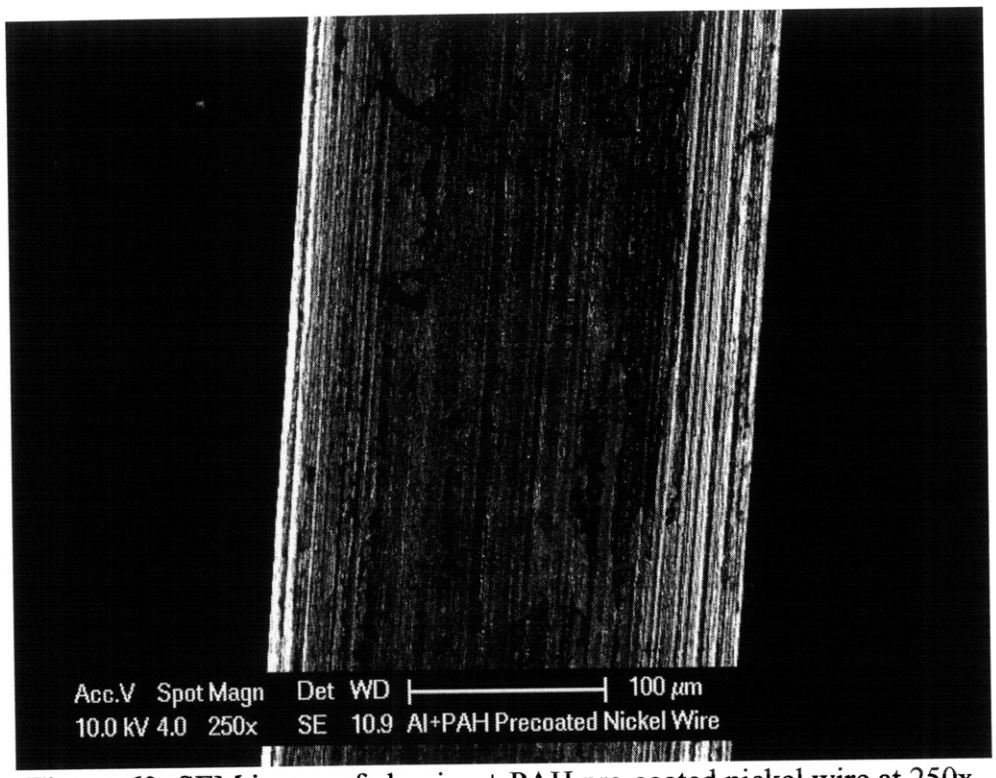

Figure 60: SEM image of alumina + PAH pre-coated nickel wire at 250x.

5.2 Results

5.2.1 Preliminary Tape Tests- Scotch electrical tape

5.2.1.1 0.1% Alumina

Figure 61 illustrates the results of the tape test conducted on a wire pre-coated with 0.1% alumina. As can be seen, the area on which the tape was applied (labeled as 'exposed nickel wire') is completely stripped of coating.

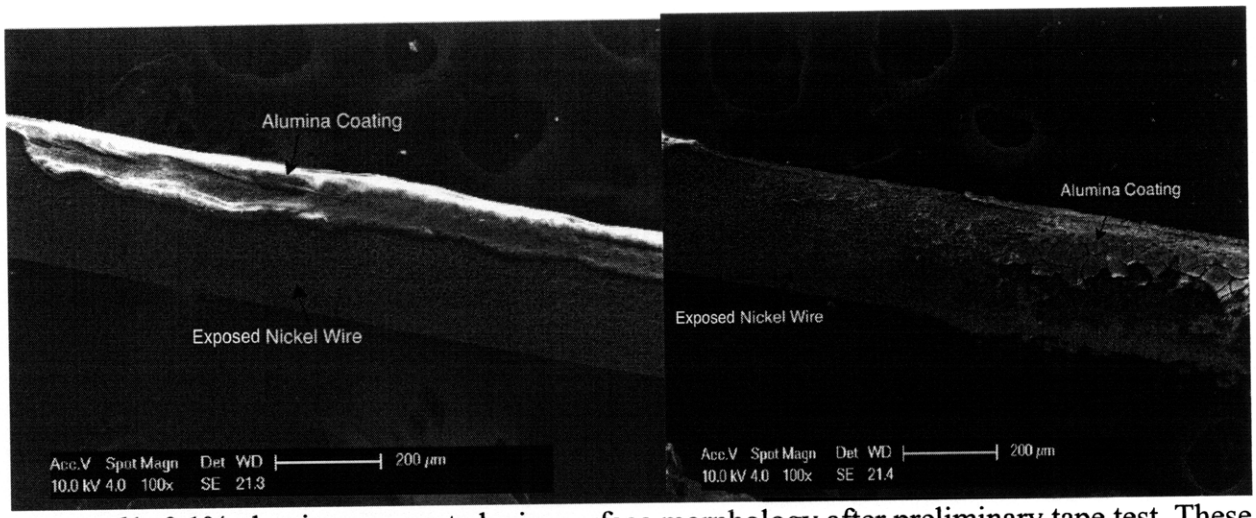

Figure 61: 0.1% alumina-pre-coated wire surface morphology after preliminary tape test. These figures show two different regions of the 0.1% alumina-pre-coated wire at 100x magnification.

5.2.1.2 Alumina + PAH

Figure 62 illustrates the results of the tape test conducted on a wire pre-coated with the alumina + PAH mixture. As can be seen, the area on which the tape was applied (labeled as 'exposed nickel wire') has had a significant amount of coating removed. Coating that remains is in non-uniform patches along the wire surface.

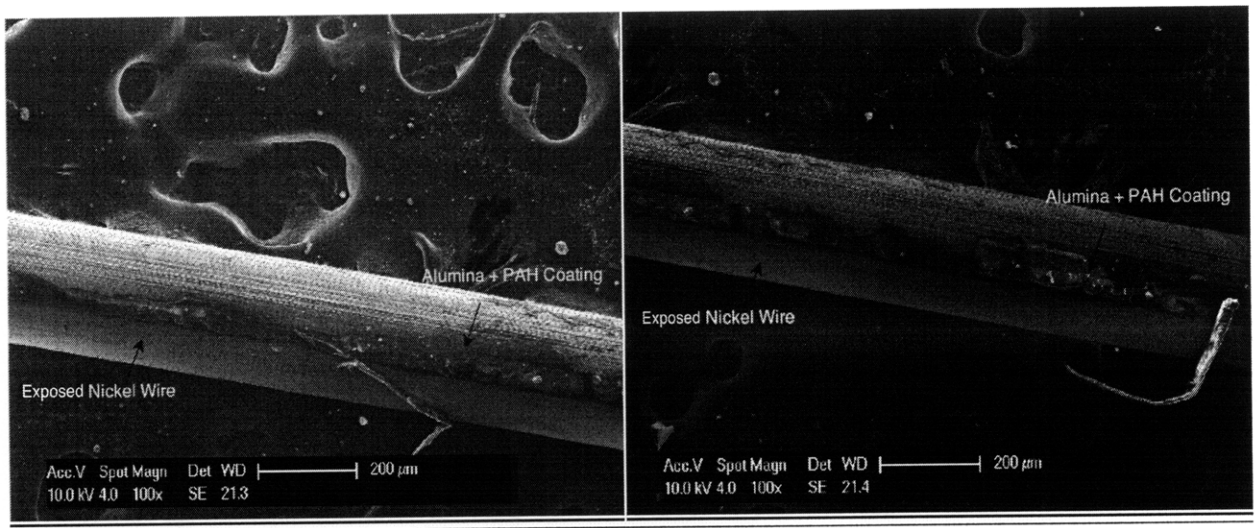

Figure 62: Alumina + PAH-pre-coated wire surface morphology after preliminary tape test. These figures show two different regions of the alumina + PAH-pre-coated wire at 100x magnification.

5.2.1.3 500ppm PAH

Figure 63 illustrates the results of the tape test conducted on a wire pre-coated with 500ppm PAH. As can be seen, the area on which the tape was applied (labeled as 'exposed nickel wire') has had a significant amount of coating removed. Coating that remains is in non-uniform patches along the wire surface.

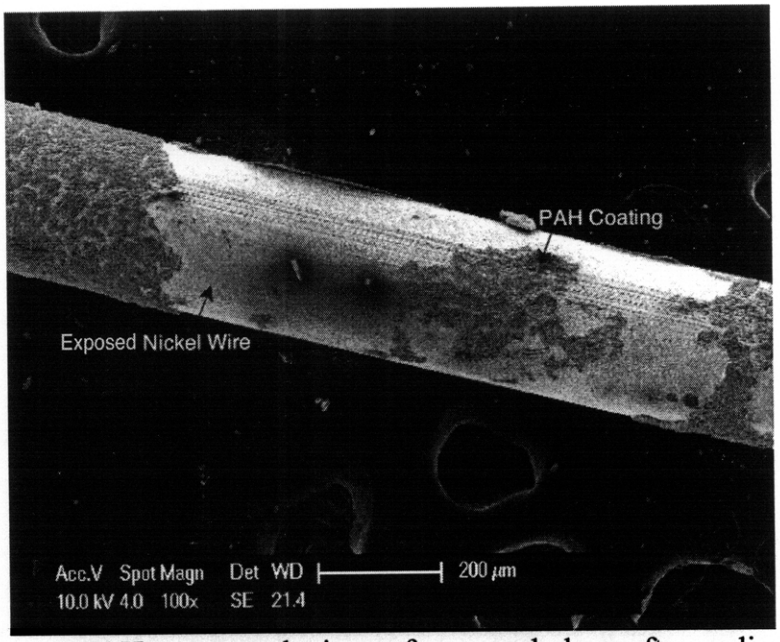

Figure 63: 500ppm PAH-pre-coated wire surface morphology after preliminary tape test.

5.2.2 Final Tape Tests - Scotch transparent tape

5.2.2.1 0.1% Alumina

Figure 64 illustrates the results of the more standard tape test conducted on a wire pre-coated with 0.1% alumina. As can be seen, the area on which the tape was applied (labeled as 'exposed nickel wire') has had a significant amount of coating removed. Coating that remains is in non-uniform patches along the wire surface. Note that there are large sections of bare nickel wire showing through the alumina coating.

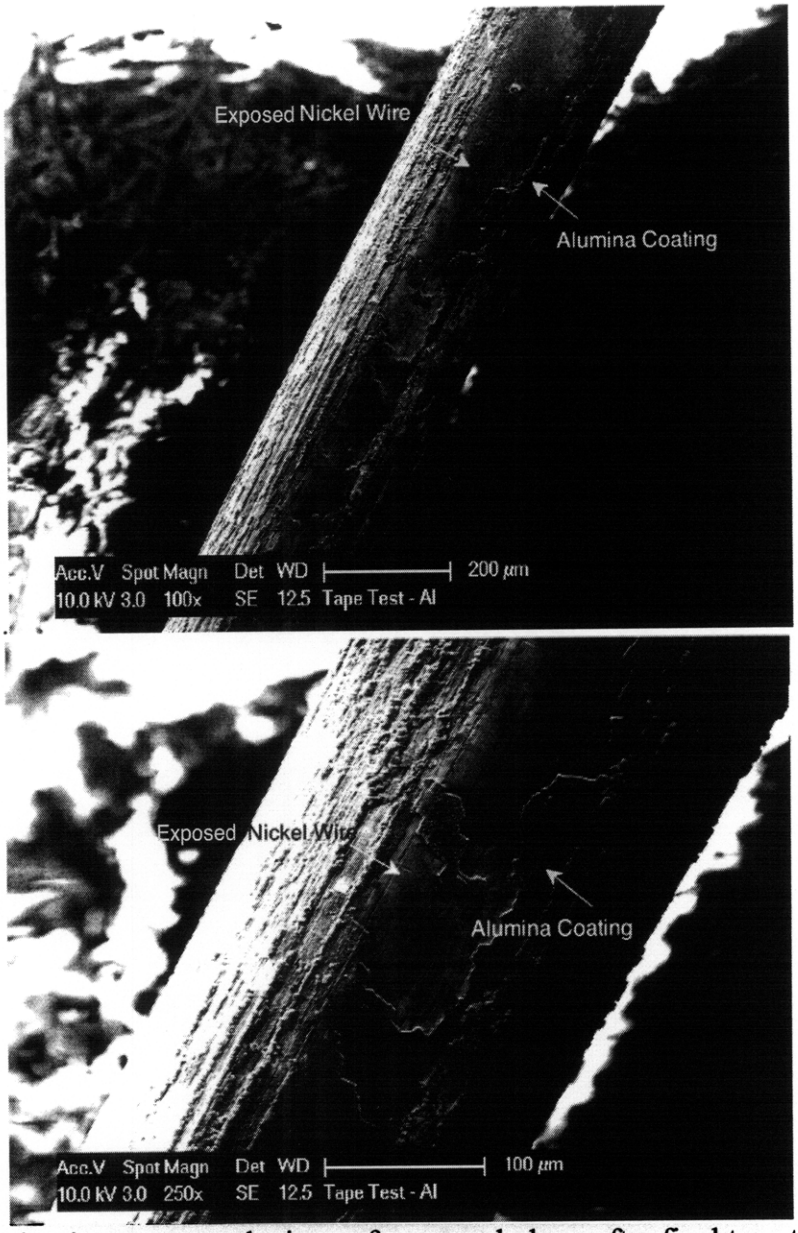

Figure 64: 0.1% alumina-pre-coated wire surface morphology after final tape test. These figures show the same region of the 0.1% alumina-pre-coated wire at 100x (left) and 250x (right) magnifications.

5.2.2.2 Alumina + PAH

Figures 65 and 66 illustrate the results of the more standard tape test conducted on a wire pre-coated with the alumina + PAH mixture. As can be seen, the area on which the tape was applied (labeled as 'exposed nickel wire') has removed some of the coating in a fairly uniform method. Figure 65 shows a stippled removal of the alumina + PAH coating in the portion

labeled 'peeled section'. Rather than have patches of bare nickel wire, the coating is still uniform. Figure 66 shows a similar phenomenon.

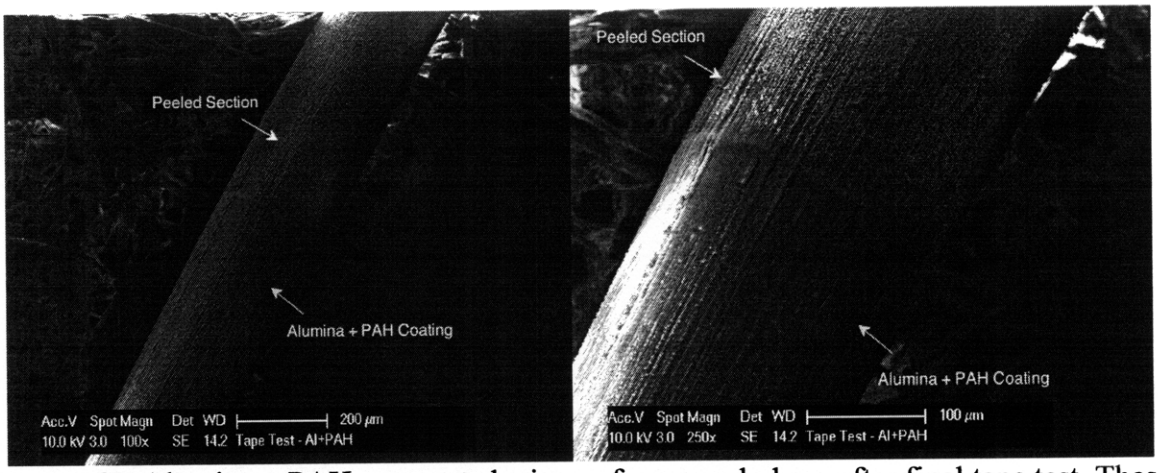

Figure 65: Alumina + PAH-pre-coated wire surface morphology after final tape test. These figures show the same region of the alumina + PAH-pre-coated wire at 100x (left) and 250x (right) magnifications.

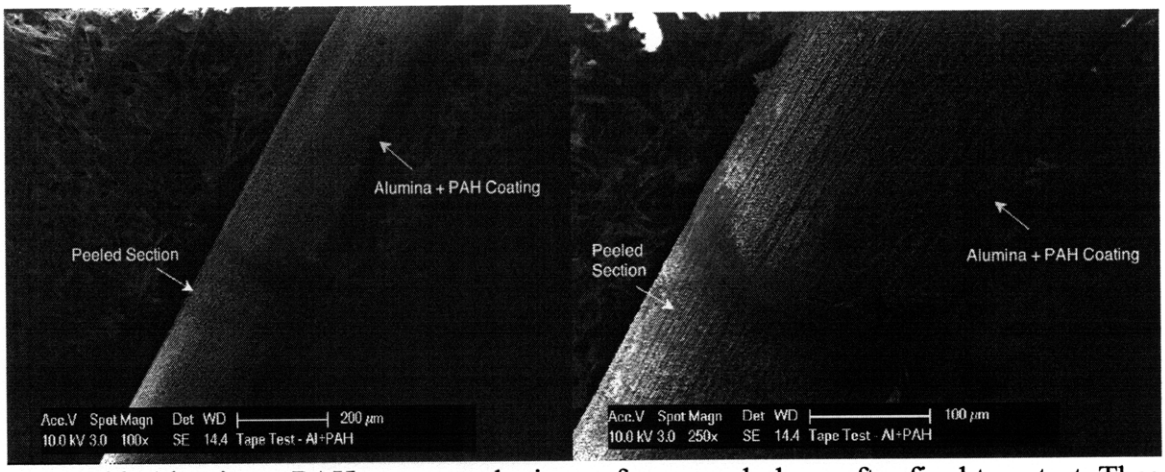

Figure 66: Alumina + PAH-pre-coated wire surface morphology after final tape test. These figures show the same region of the alumina + PAH-pre-coated wire at 100x (left) and 250x (right) magnifications.

5.2.3 Preliminary 1.0% Alumina Bend Tests

5.2.3.1 – 3 1/2" Diameter

Figure 67 illustrates the results of the preliminary bend test conducted on a wire pre-coated with 0.1% alumina at a rod diameter of 3 1/2". As can be seen, a significant amount of the coating has been removed. Coating that remains is in non-uniform patches along the wire

surface. Note that there are large sections of bare nickel wire showing through the alumina coating.

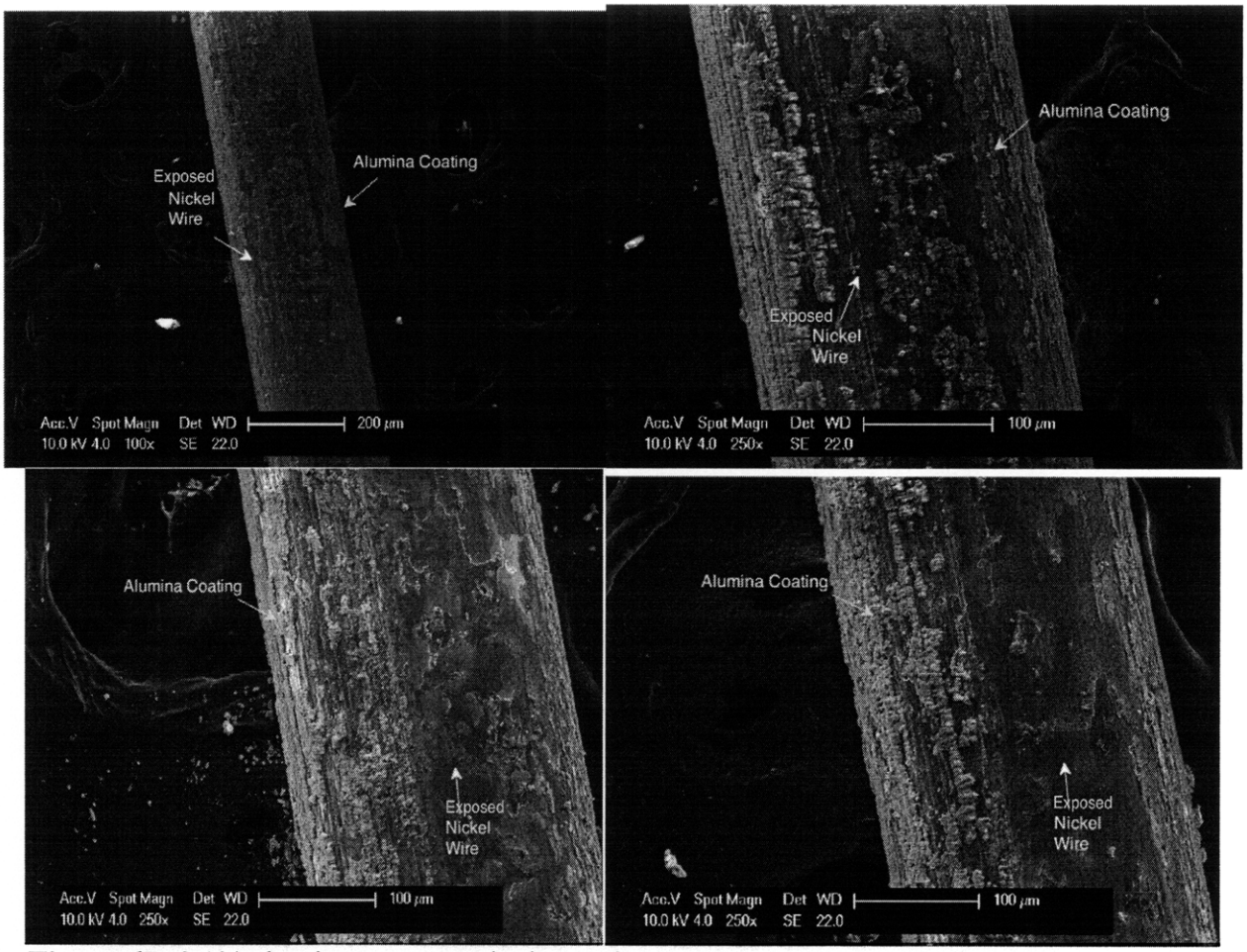

Figure 67: 0.1% alumina-pre-coated wire surface morphology after 3 1/2" rod diameter bend test. These figures show regions of the 0.1% alumina-pre-coated wire at (clockwise from upper left): 100x, 250x, 250x, and 250x magnifications.

5.2.3.2 - 10 11/32" Diameter

Figures 68 and 69 illustrate the results of the preliminary bend test conducted on a wire pre-coated with 0.1% alumina at a rod diameter of 10 11/32". As can be seen, a significant amount of the coating has cracked and some coating has even been removed. Coating that remains is in non-uniform patches along the wire surface. Note that there are sections of bare nickel wire showing through the alumina coating.

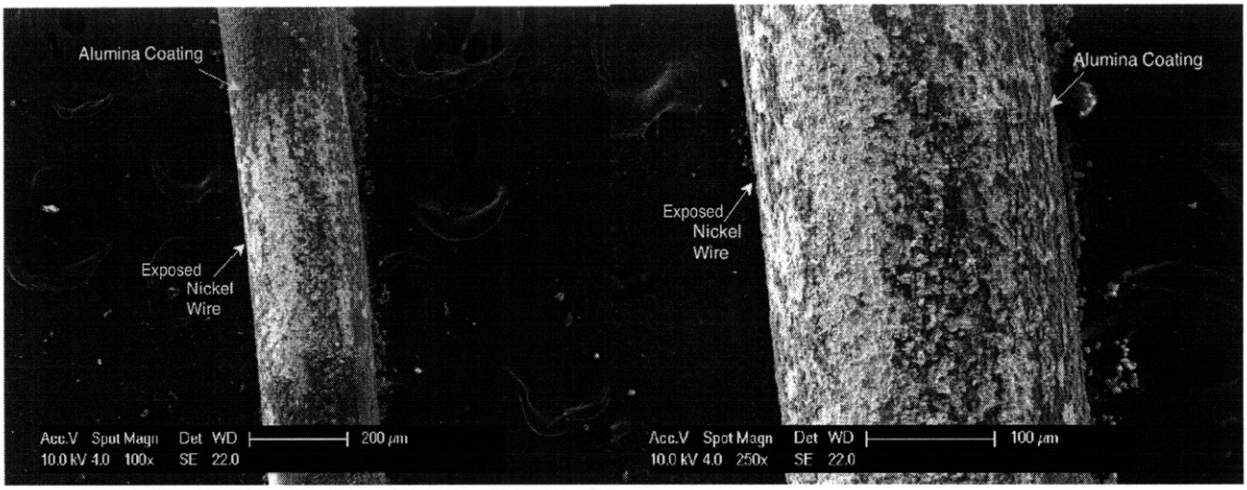

Figure 68: 0.1% alumina-pre-coated wire surface morphology after 10 11/32" rod diameter bend test. These figures show the same region of the 0.1% alumina-pre-coated wire at 100x (left) and 250x (right) magnifications. Note that a visible amount of coating has transferred to the mounting tape, perhaps due to sample movement.

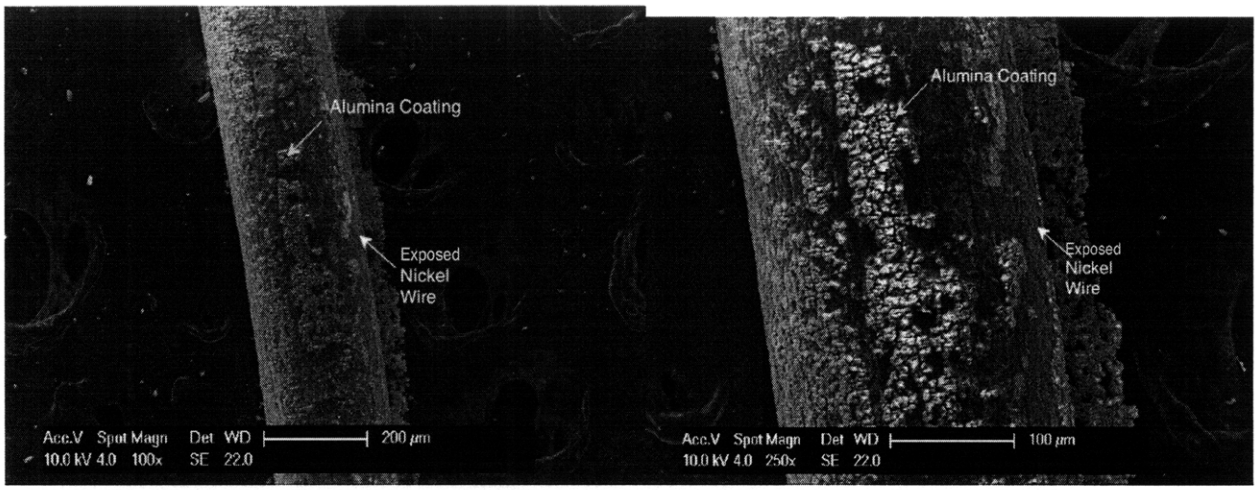

Figure 69: 0.1% alumina-pre-coated wire surface morphology after 10 11/32" rod diameter bend test. These figures show the same region of the 0.1% alumina-pre-coated wire at 100x (left) and 250x (right) magnifications. Note that a visible amount of coating has transferred to the mounting tape, perhaps due to sample movement.

5.2.3.3 - 11 11/32" Diameter

Figures 70 and 71 illustrate the results of the preliminary bend test conducted on a wire pre-coated with 0.1% alumina at a rod diameter of 11 11/32". As can be seen, most of the coating has cracked and a small amount of coating has been removed from the wire. Note that large sections of bare nickel wire are *not* showing through the alumina coating at this rod diameter (seen more clearly in the 250x magnification).

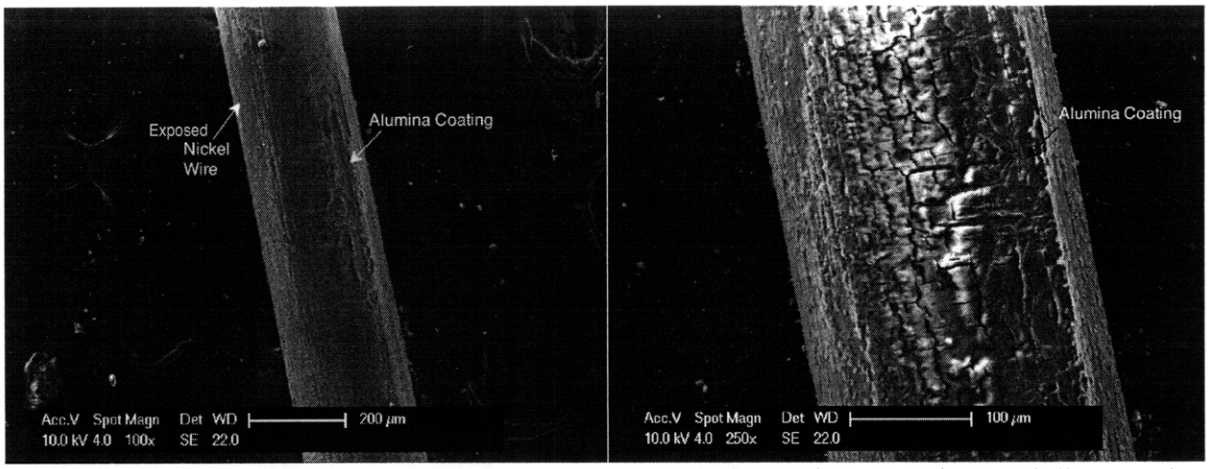

Figure 70: 0.1% alumina-pre-coated wire surface morphology after 11 11/32" rod diameter bend test. These figures show the same region of the 0.1% alumina-pre-coated wire at 100x (left) and 250x (right) magnifications.

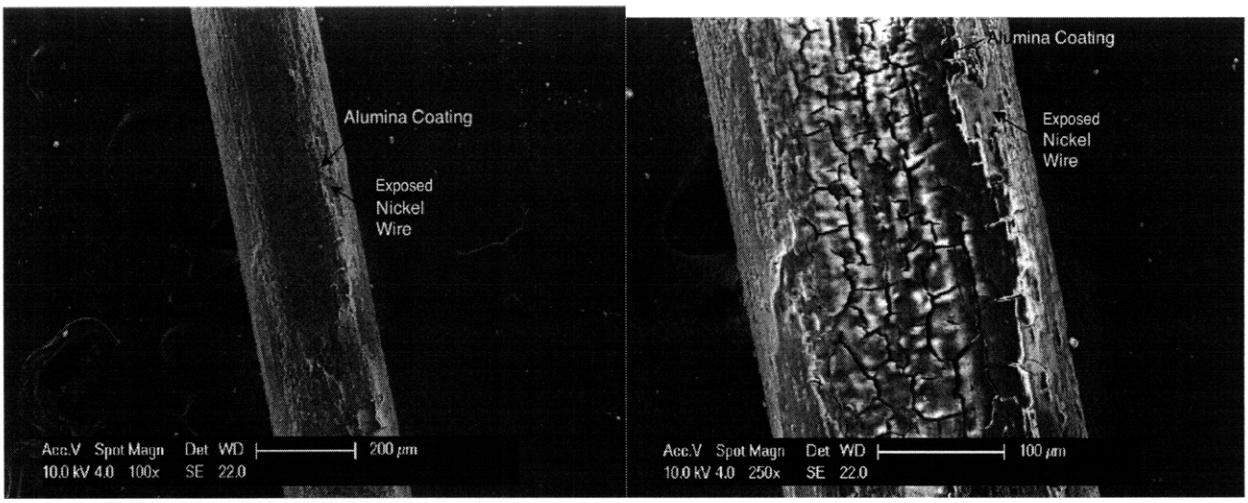

Figure 71: 0.1% alumina-pre-coated wire surface morphology after 11 11/32" rod diameter bend test. These figures show the same region of the 0.1% alumina-pre-coated wire at 100x (left) and 250x (right) magnifications.

5.2.4 Final Bend Tests - 10 11/32" Diameter

5.2.4.1 0.1% Alumina

Figures 72 through 75 illustrate the results of the final bend test conducted on two different wires pre-coated with 0.1% alumina at a rod diameter of 10 11/32" (Figures 72 and 873 illustrate a wire pre-coated on 4/2 and Figures 74 and 75 illustrate a wire pre-coated on 3/31). As can be seen, a significant amount of the coating has cracked and some coating has even been removed. Coating that remains is in non-uniform patches along the wire surface. Note that there

are sections of bare nickel wire showing through the alumina coating.

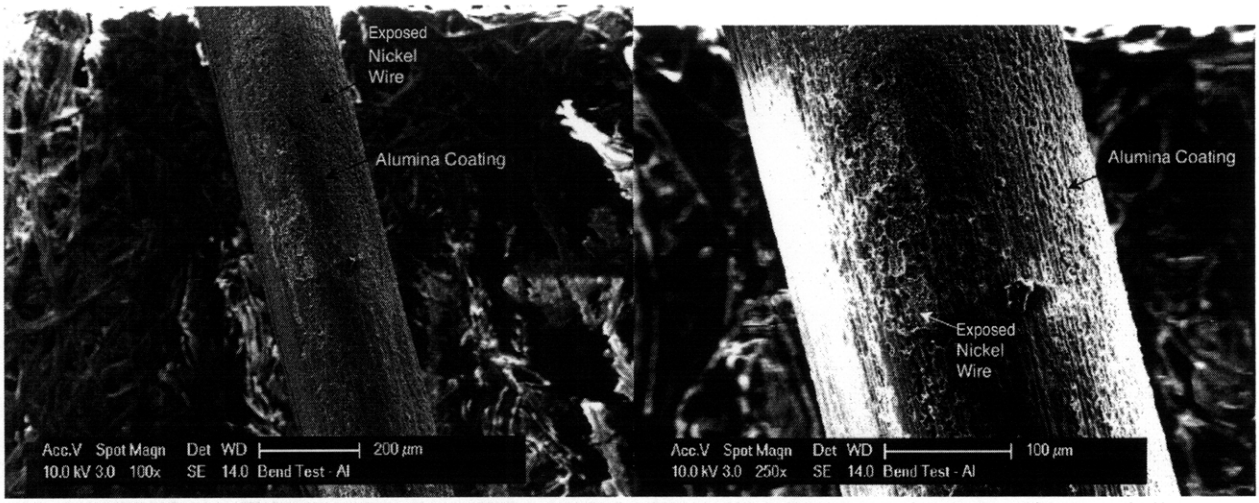

Figure 72: 0.1% alumina-pre-coated wire (4/2) surface morphology after 10 11/32" rod diameter bend test. These figures show the same region of the 0.1% alumina-pre-coated wire at 100x (left) and 250x (right) magnifications.

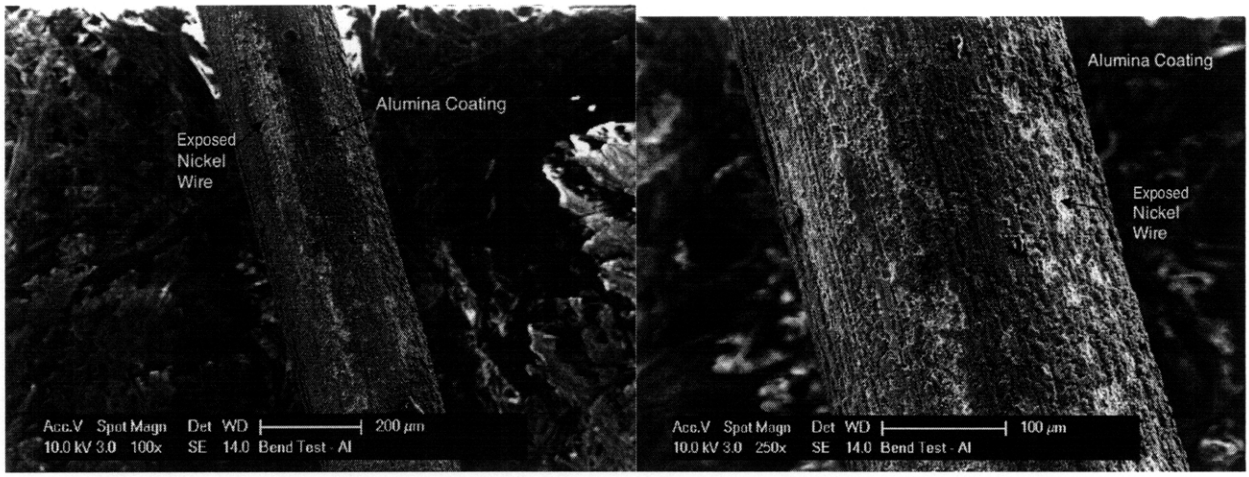

Figure 73: 0.1% alumina-pre-coated wire (4/2) surface morphology after 10 11/32" rod diameter bend test. These figures show the same region of the 0.1% alumina-pre-coated wire at 100x (left) and 250x (right) magnifications.

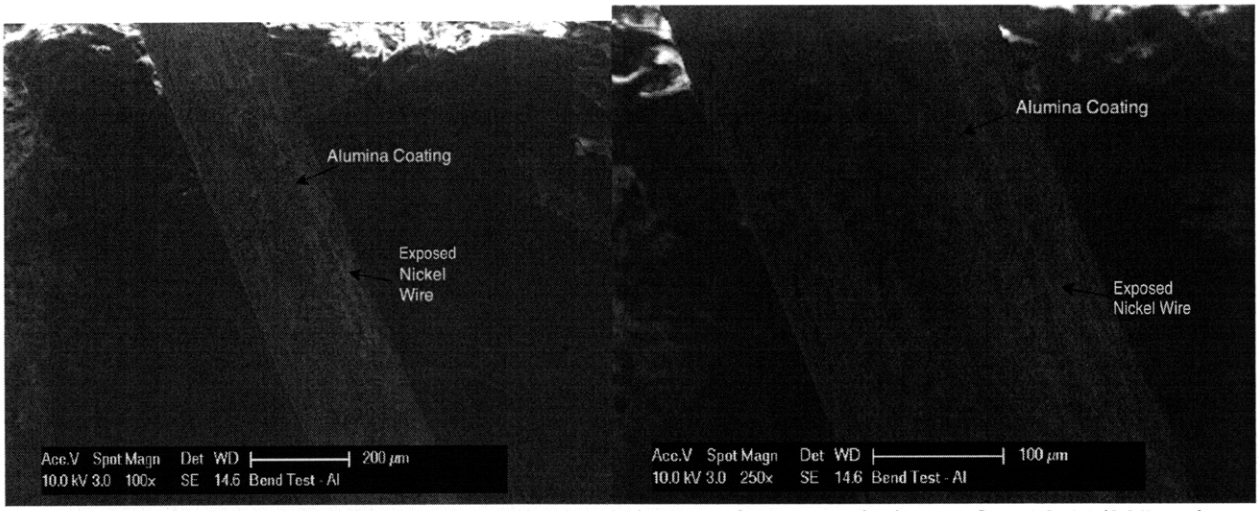

Figure 74: 0.1% alumina-pre-coated wire (3/31) surface morphology after 10 11/32" rod diameter bend test. These figures show the same region of the 0.1% alumina-pre-coated wire at 100x (left) and 250x (right) magnifications.

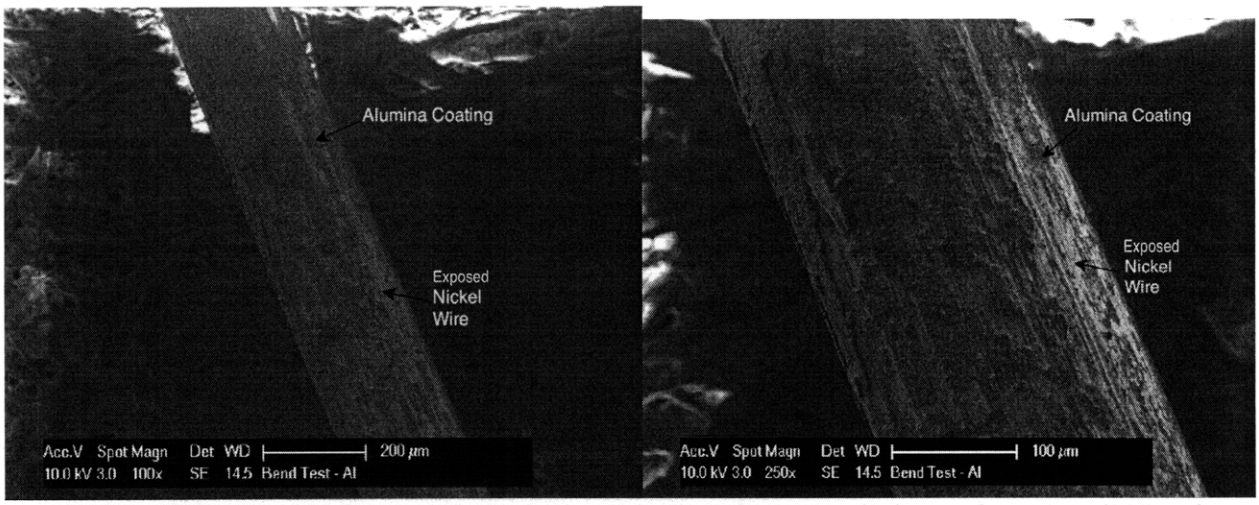

Figure 75: 0.1% alumina-pre-coated wire (3/31) surface morphology after 10 11/32" rod diameter bend test. These figures show the same region of the 0.1% alumina-pre-coated wire at 100x (left) and 250x (right) magnifications.

5.2.4.2 Alumina + PAH

Figures 76 and 77 illustrate the results of the final bend test conducted on two different wires pre-coated with 0.1% alumina and 500ppm PAH at a rod diameter of 10 11/32" (Figure 76 illustrates a wire pre-coated on 3/19 and Figure 77 illustrates a wire pre-coated on 4/2). As can be seen, there is no apparent sign that the coating has cracked or spalled from the surface.

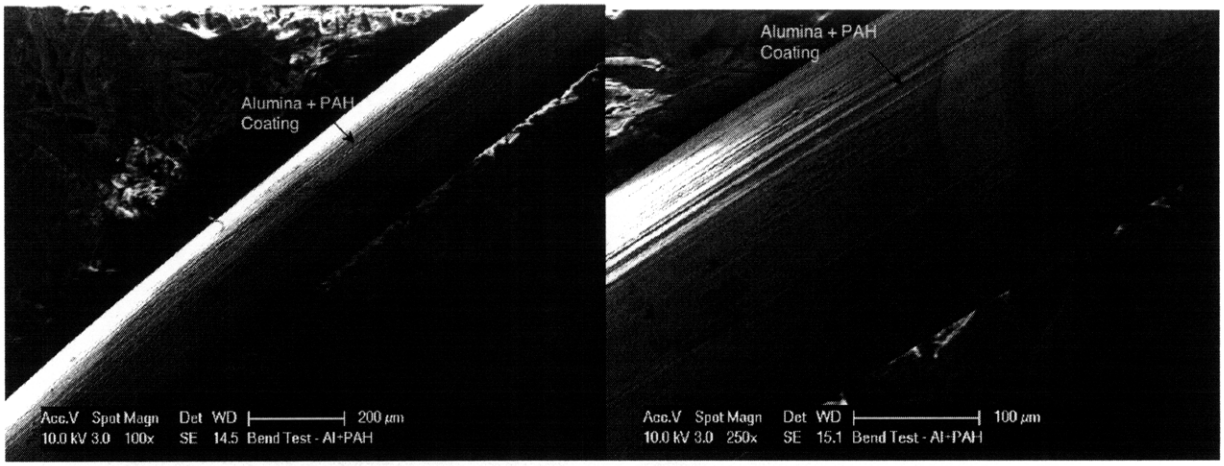

Figure 76: Alumina and PAH-pre-coated wire (3/19) surface morphology after 10 11/32" rod diameter bend test. These figures show the same region of the alumina + PAH-pre-coated wire at 100x (left) and 250x (right) magnifications. The striated lines are most likely caused by the die through which the wire was drawn.

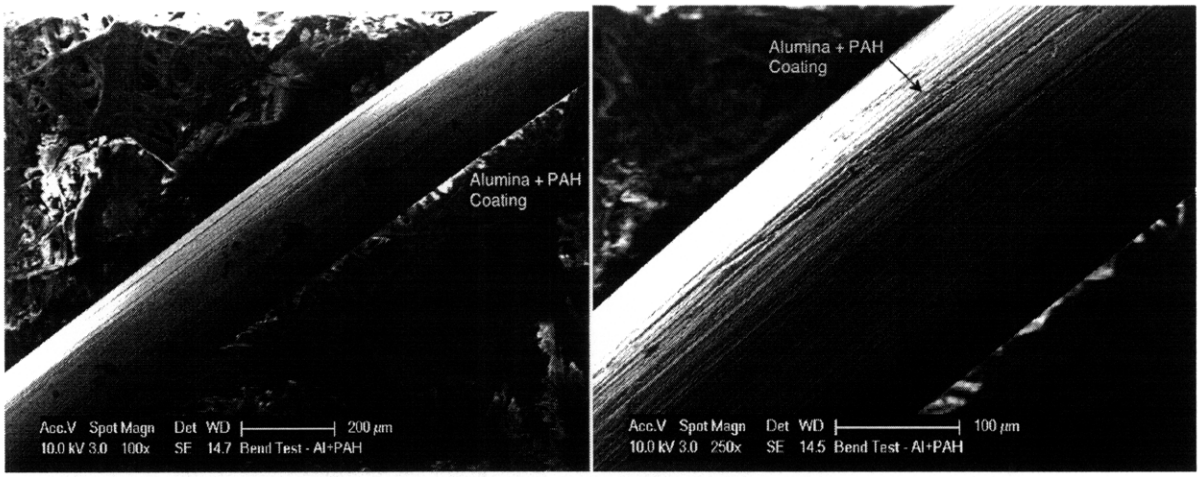

Figure 77: Alumina and PAH-pre-coated wire (4/2) surface morphology after 10 11/32" rod diameter bend test. These figures show the same region of the alumina + PAH-pre-coated wire at 100x (left) and 250x (right) magnifications.

5.2.5 Final Bend Tests - 11 11/32" Diameter

5.2.5.1 0.1% Alumina

Figures 78 through 81 illustrate the results of the final bend test conducted on two different wires pre-coated with 0.1% alumina at a rod diameter of 11 11/32" (Figures 78 and 79 illustrate a wire pre-coated on 3/31 and Figures 80 and 81 illustrate a wire pre-coated on 4/2). As can be seen, a significant amount of the coating has cracked and some coating has even been removed. Coating that remains is in non-uniform patches along the wire surface. Note that there

are small sections of bare nickel wire showing through the alumina coating.

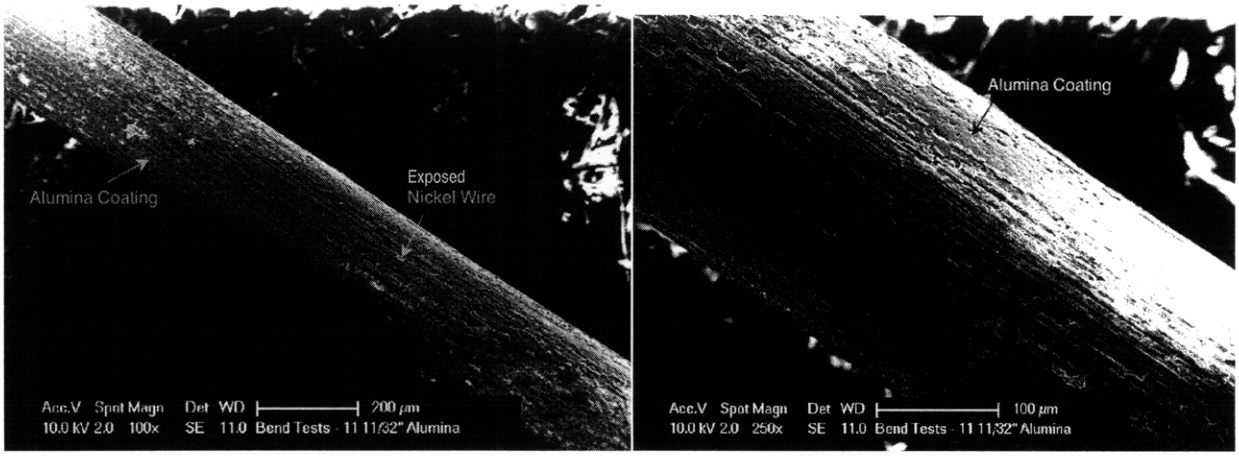

Figure 78: 0.1% alumina-pre-coated wire (3/31) surface morphology after 11 11/32" rod diameter bend test. These figures show the same region of the 0.1% alumina-pre-coated wire at 100x (left) and 250x (right) magnifications.

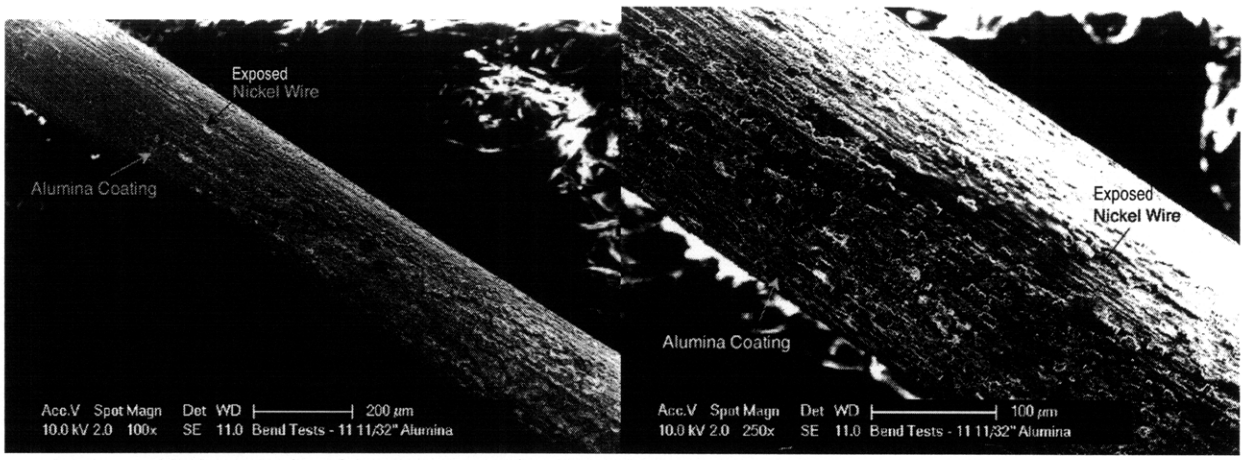

Figure 79: 0.1% alumina-pre-coated wire (3/31) surface morphology after 11 11/32" rod diameter bend test. These figures show the same region of the 0.1% alumina-pre-coated wire at 100x (left) and 250x (right) magnifications.

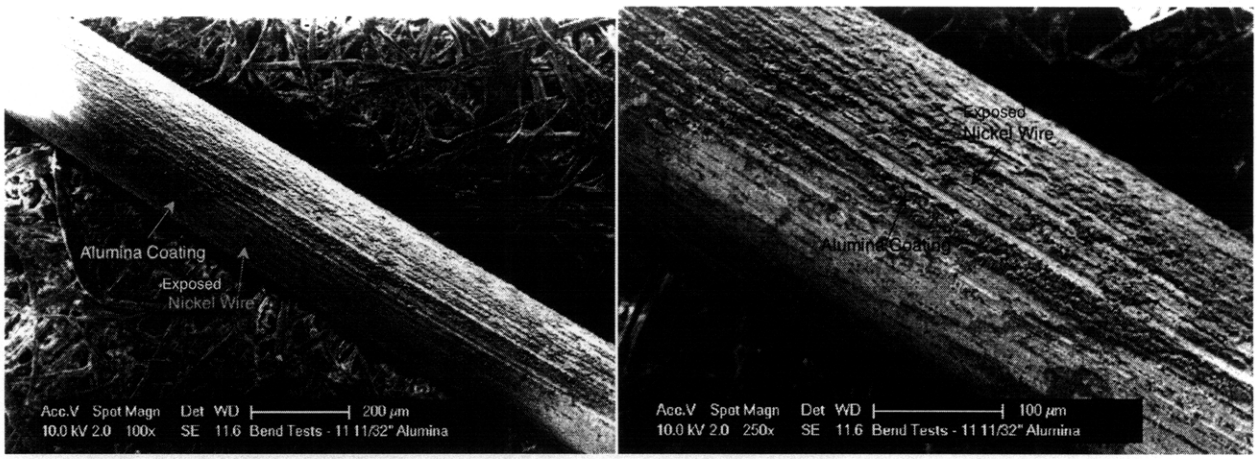

Figure 80: 0.1% alumina-pre-coated wire (4/2) surface morphology after 11 11/32" rod diameter bend test. These figures show the same region of the 0.1% alumina-pre-coated wire at 100x (left) and 250x (right) magnifications.

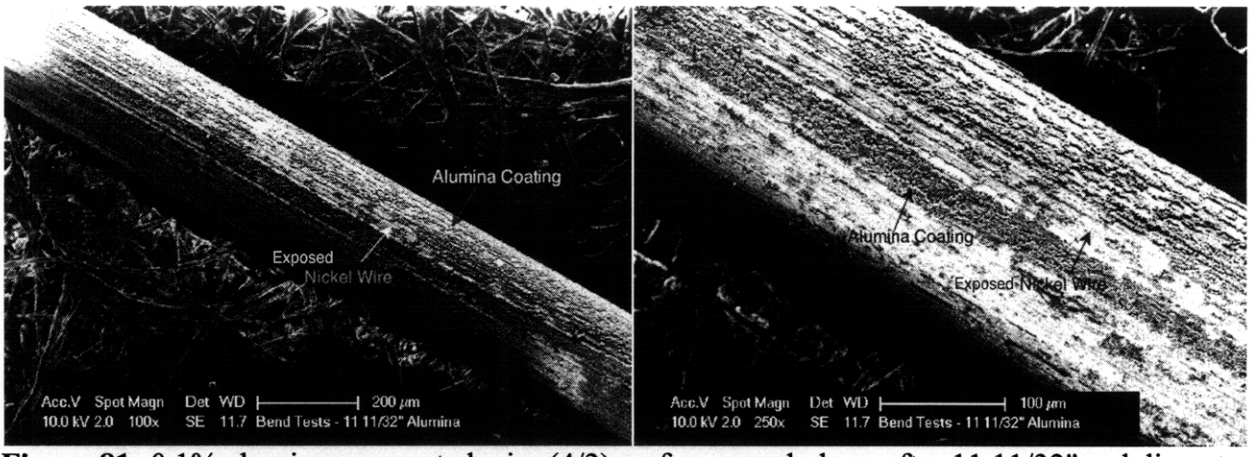

Figure 81: 0.1% alumina-pre-coated wire (4/2) surface morphology after 11 11/32" rod diameter bend test. These figures show the same region of the 0.1% alumina-pre-coated wire at 100x (left) and 250x (right) magnifications.

5.2.5.2 Alumina + PAH

Figures 82 and 83 illustrate the results of the final bend test conducted on two different wires pre-coated with 0.1% alumina and 500ppm PAH at a rod diameter of 11 11/32" (Figure 82 illustrates a wire pre-coated on 3/19 and Figure 83 illustrates a wire pre-coated on 4/2). As can be seen, there is no apparent sign that the coating has cracked or spalled from the surface.

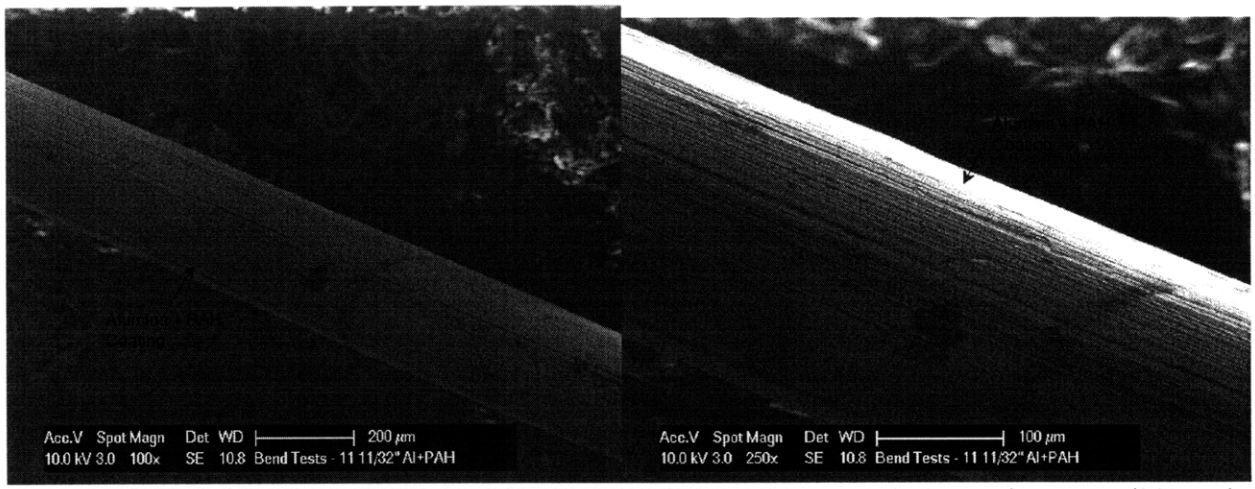

Figure 82: Alumina and PAH-pre-coated wire (3/19) surface morphology after 11 11/32" rod diameter bend test. These figures show the same region of the alumina + PAH-pre-coated wire at 100x (left) and 250x (right) magnifications.

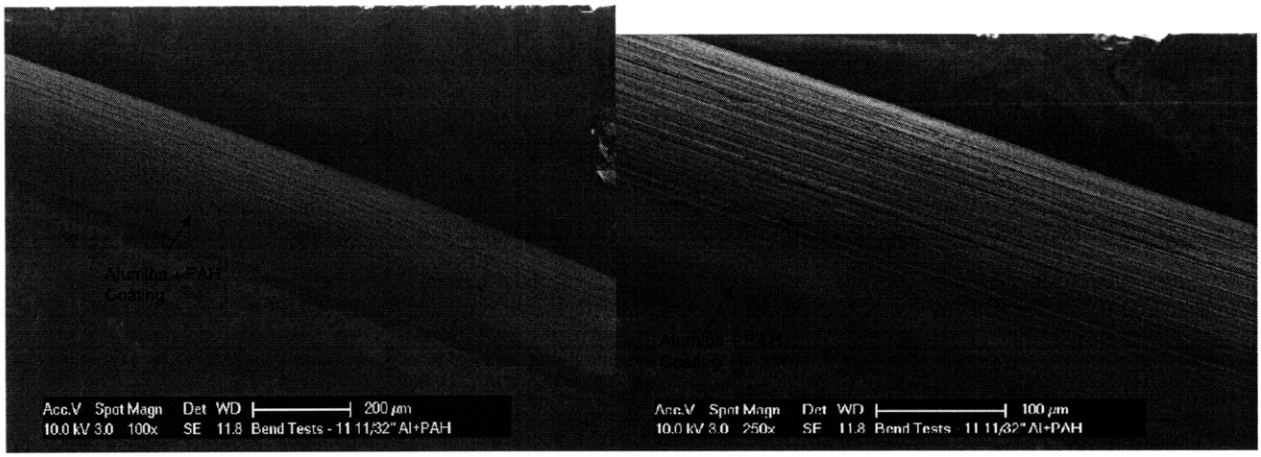

Figure 83: Alumina and PAH-pre-coated wire (4/2) surface morphology after 11 11/32" rod diameter bend test. These figures show the same region of the alumina + PAH-pre-coated wire at 100x (left) and 250x (right) magnifications.

5.3 Analysis

5.3.1 Preliminary Tape Tests - Scotch vinyl tape

Although the tape used in the preliminary tape tests was not ideal for this purpose, since electrical tape leaves visible adhesive residue, the general results are still informative. When applied to a wire pre-coated with 0.1% alumina, the tape completely stripped the coating from the wire (Figure 61). The behavior of the alumina coating was used as a standard to which the other coatings were compared. The alumina + PAH coating was not completely removed from

the wire and was instead removed in non-uniform patches (Figure 62). Similarly, the PAH coating was not completely removed from the wire (Figure 63).

Since both the PAH and alumina + PAH coatings were resilient to the tape test, it seems that the addition of the PAH (a polymer) to the coating improved the coating adhesion. Without rigorous testing using strict guidelines, this improvement cannot be proven. However, the results of the preliminary tape test indicate that, as expected theoretically, the addition of a polymer improves coating adhesion.

5.3.2 Final Tape Tests - Scotch transparent tape

Transparent scotch tape was used for the final tape tests as recommended by various ASTM standards. The transparent tape was less adhesive than the electrical tape, in general peeling off less of the surface coating. When applied to a wire pre-coated with 0.1% alumina, the tape stripped the coating from the wire in non-uniform patches, exposing a significant amount of the bare wire (Figure 64). These bare patches could affect the CHF value of the stripped wire, since the exposed nickel wire would have a CHF value closer to that of bare wire. The behavior of the alumina coating was used as a standard to which the other coatings were compared.

The alumina + PAH coating was removed in a stippled pattern and did not expose patches of bare wire (Figures 65 and 66). The alumina + PAH coating remaining was relatively uniform, and presumably would still allow for enhanced heat transfer and a higher CHF compared to bare wire. However, it is unclear whether the CHF value for the stripped wire would be the same as that of an alumina + PAH-pre-coated wire. The alumina + PAH coatings were fairly resilient to the tape test, again indicating that the addition of the PAH (a polymer) to the coating improved the coating adhesion.

5.3.3 Preliminary 0.1% *Alumina Bend Tests*

As can be seen in Figure 67, the 0.1% alumina coating experienced significant spallation at a rod diameter of 3 1/2" (roughly 33% of the failure diameter, 10 3/5"). Much of the nickel wire has been exposed, and the remaining coating is severely cracked and appears in non-uniform patches.

Figures 68 and 69 illustrate significant cracking in the coating but a lower amount of spallation at a rod diameter of 10 11/32". Most of the nickel wire is still covered by the alumina coating. An interesting observation is that the amount of coating on the mounting tape is higher for the rod diameter of 10 11/32" than 3 1/2", presumably because the wire bent around the 3 1/2" diameter rod has already spalled off most of its coating.

Figures 70 and 71 illustrate minor cracking and no spallation of the alumina coating at a rod diameter of 11 11/32" (roughly 7% larger than the failure diameter, 10 3/5"). Cracking at a diameter of 11 11/32" indicates that the failure diameter of 10.6" is only a rough estimate of the diameter at which the alumina coating begins to crack. Also, cracking at a diameter of 11 11/32" could be due to the inconsistency in the alumina coating thickness. Variations in the coating thickness could affect the rod radius required to induce coating failure (see Equation 17).

5.3.4 Final Bend Tests

As in the preliminary bend tests, the 0.1% alumina coating experienced significant cracking and limited spallation at rod diameters of 10 11/32" (Figures 72 through 75) and 11 11/32" (Figures 77 through 81). The wires coated with the alumina + PAH mixture, however, did not experience any cracking or spallation at these rod diameters. The entire lengths of both alumina + PAH-pre-coated wires were examined for small cracks or spallation, but the coating was not altered. In general, the alumina + PAH coating was not as thick as the 0.1% alumina

coating. This difference in thickness could have affected the response of the alumina + PAH coating to the various bending diameters.

5.3.5 Comparison to Shear Stress in Industrial Applications

Several attempts have been made to estimate the shear stress due to fluid flow in different industrial applications, including nuclear reactors [34, 35]. Most calculations of wall shear stress in two-phase flow have used rectangular rather than circular pipe geometries. However, in most nuclear systems, including steam generator tubes, circular pipes are used.

Table 17 contains a summary of Sampaio's findings in examining the shear stress due to two-phase fluid flow (laminar in both liquid and gas phases) with a smooth interface in a horizontal circular pipe. The mean wall interface shear stress reported was found using Biberg and Halvorsen's analytic model [34].

Table 17: Average wall shear stress for laminar-laminar two-phase flow in a horizontal, circular pipe [34]. U is the superficial velocity [cm/s] and τ is the mean wall interface shear stress with subscripts f and g denoting liquid and gas, respectively.

Case	U_{fs} *(cm/s)*	U_{gs} *(cm/s)*	τ_g *(mPa)*	τ_f *(mPa)*
1	0.084	1.686	0.1193	0.2481
2	0.169	3.373	0.2390	0.4968
3	0.337	3.373	0.3216	0.7497

Table 18 contains a summary of Wongwises' finding in examining the gas-wall shear stress due to fully developed, turbulent, stratified two-phase flow in a horizontal circular pipe. The gas-wall shear stress reported was found using Preston's method for measuring skin friction in the turbulent boundary layer [35].

Table 18: Gas-wall shear stress due to stratified two-phase flow in a horizontal, circular pipe [35]. Re is the Reynolds number with subscripts L and G denoting liquid and gas, respectively, D is the pipe diameter [m], and τ is the gas-wall shear stress.

Case	Re_L	Re_G	*D (m)*	*Flow Type*	τ_w *(Pa x10^2)*
1	5184	8363	0.054	smooth	3.5
2	5962	6258	0.054	smooth	2.8
3	3619	7062	0.029	smooth	10.5
4	5367	12932	0.054	wavy	8.5
5	5558	15266	0.054	wavy	10.5
6	3798	8797	0.029	wavy	16.5

The wall shear stresses reported by both Sampaio and Wongwises are much lower than the 300 MPa tensile stress required to fracture the alumina coating. However, previously existing flaws and non-uniform coating could cause the coating to erode at lower stresses.

6 Conclusions

Compared to pure alumina nanofluids, specifically 0.1 % alumina, the coating obtained from combined alumina and PAH dispersion coating had the following effects on thermal and adhesive performance:

- Enhanced CHF by ~40%, compared to an enhancement of ~37% with 0.1 % alumina,
- Degraded HTC by less than 1%, compared to a degradation of ~27% with 0.1 % alumina, and
- Did not experience any adhesion failure modes (cracking or spallation) at a strain of 8.108×10^{-4}.

The CHF and HTC test results presented in Section 4 illustrate the enhanced performance of the alumina and PAH coating compared to all other coatings examined (1.0% alumina, 0.1% alumina, and 500ppm PAH). The combined alumina nanoparticle and PAH dispersion enhanced CHF by ~40%, which was on the order of CHF enhancement due to 0.1% alumina coating, but did not degrade HTC. Therefore, the thermal performance enhancement of the combined alumina and PAH coating is higher than that of a pure substance nanofluid. Future work is recommended in determining an optimum mixture of alumina and PAH (or, more generally, different types of nanoparticle and polymer) for maximum CHF and HTC enhancement.

The adhesion test results presented in Section 5 illustrate the relative resilience of the alumina and PAH coating. Qualitatively, the composite alumina and PAH coating was more resilient to the tape tests than the 0.1% alumina coating. The tape used in both tests stripped large sections of the 0.1% alumina coating from the wire but relatively little of the alumina and PAH coating. More quantitatively, the alumina and PAH coating did not experience significant cracking at tensile stresses that induced cracking and spallation in the 0.1% alumina coating. To

determine the failure tensile strain of the alumina and PAH coating, a conical Mandrel bend test should be conducted.

Appendix A- Error Analysis and Propagation

A.1 - Experimental (Instrumentation) Error

Determining the temperature coefficient of resistivity uncertainty required several steps. First, nickel wire was chosen as the wire heater because it has a relatively well-established temperature coefficient of resistivity, compared to alloys such as nickel-chromium or stainless steel that were used in previously in our lab. Based on previous experimentation, heaters like stainless steel behave less reliably with increasing temperature. Second, the nickel wire temperature coefficient of resistivity was verified by experimentation. The wire temperature was found using the following relationship:

$$T_{wire} = \frac{\left(\frac{R_{wire}}{R_0} - 1\right)}{\alpha} + T_0, \qquad \text{(A-1)}$$

with R_{wire} equal to the current wire resistance, R_0 equal to the initial wire resistance, α equal to the temperature coefficient of reactivity, and T_0 equal to the initial bulk fluid temperature. The uncertainty of α was estimated using a best-fit regression (Figure A.1-1, supplied by Eric

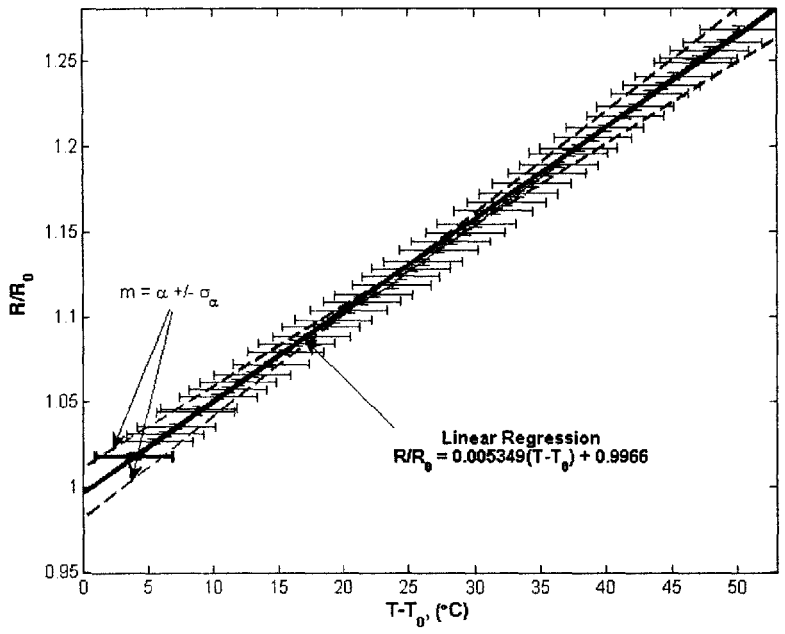

Figure A.1-1: Linear regression solution for α, with σ_α ~10.6%.

Forrest). The uncertainty of the bulk fluid temperature was estimated using the thermocouple measurement uncertainty. Instrumentation uncertainties for the calipers used to measure the wire diameter, shunt resistance and voltage error, and the voltage source (wire voltage) error were provided by the manufacturers.

All error values can be found in Table A.1-1. All error bars included in boiling curves throughout represent experimental (instrumentation) uncertainty rather than statistical uncertainty. Table A.1-2 includes the average CHF values with both experimental (instrumental) and statistical uncertainties.

Table A.1-1: Instrumentation error values used for error propagation.

	*Error (units)**	
Shunt resistor	1.25E-6	(Ohms)
Shunt voltage	0.5E-3	(mV)
Wire voltage	0.01	(V)
Wire diameter	0.001	(cm)
Wire length	0.3	(cm)
Bulk temperature	0.3	(°C)
α	0.1	($°C^{-1}$)
Bend rod radius	3/16	(inches)
Coating thickness	2	(μm)

*Note that some units are percentages of the data values rather than a constant.

Error bars included in boiling curves represent experimental (instrumentation) uncertainty rather than statistical uncertainty. Experimental uncertainty describes all uncertainties in the measurement devices used to collect data whereas statistical uncertainty describes the uncertainty that a data point (for example, an average CHF value) represents the population of data points (all measured values of CHF). Table A.3-1 includes the average CHF values with both experimental (instrumental) and statistical uncertainties.

A.2 - Error Propagation

A general rule for error propagation relates the error of a function of different variables to the error of those variables in the following way:

$$\Delta F(x_0 \rightarrow x_n) = \sqrt{\sum_{i=0}^{n}\left(\left(\frac{\delta F(x_i)}{\delta x_i}\right)^2 \cdot (\Delta x_i)^2\right)}, \tag{A-2}$$

with $F(x_i)$ equal to a function of the variable x_i and Δx_i equal to the error of the variable x_i. For example, the following relationship was used to find the HTC of the nickel wire:

$$h = \frac{q''}{\Delta T}. \tag{A-3}$$

The derivative of h with respect to q" is:

$$\frac{\partial h}{\partial q''} = \frac{1}{\Delta T} \tag{A-4}$$

and with respect to ΔT is:

$$\frac{\partial h}{\partial \Delta T} = -\frac{q''}{(\Delta T)^2} \tag{A-5}$$

Using these relationships, Δh can be found with the following expression:

$$\Delta h = \sqrt{\left(\left(\frac{\partial h}{\partial q''}\right)^2 \cdot (\Delta q'')^2 + \left(\frac{\partial h}{\partial \Delta T}\right) \cdot (\Delta(\Delta T))^2\right)} \tag{A-6}$$

or:

$$\Delta h = \sqrt{\left(\left(\frac{1}{\Delta T}\right)^2 \cdot (\Delta q'')^2 + \left(\frac{-q''}{(\Delta T)^2}\right)^2 \cdot (\Delta(\Delta T))^2\right)}, \tag{A-7}$$

which simplifies to:

$$\Delta h = h \cdot \sqrt{\left(\left(\frac{\Delta(\Delta T)}{(\Delta T)}\right)^2 + \left(\frac{\Delta q''}{q''}\right)^2\right)}. \tag{A-8}$$

A more general expression for this behavior is:

$$\left(\frac{\Delta F(x_0 \rightarrow x_n)}{F(x_0 \rightarrow x_n)}\right)^2 = \sum_{i=0}^{n}\left(\left(\frac{\Delta x_i}{x_i}\right)^2\right) \tag{A-9}$$

This expression can be used for functions that either divide or multiply the variables with associated errors (see Equation A-3 for an example).

The error of an average value can also be derived from Equation A-2. However, this expression can be simplified to:

$$\Delta x_{avg} = \frac{1}{n}\sqrt{\sum_{i=0}^{n}\left((\Delta x_i)^2\right)}, \tag{A-10}$$

with n equal to the number of values taken into the average. This expression was used to evaluate errors on all average CHF and HTC values. For example, the error bars in Figures A.2-1 and A.2-2 were generated using this expression.

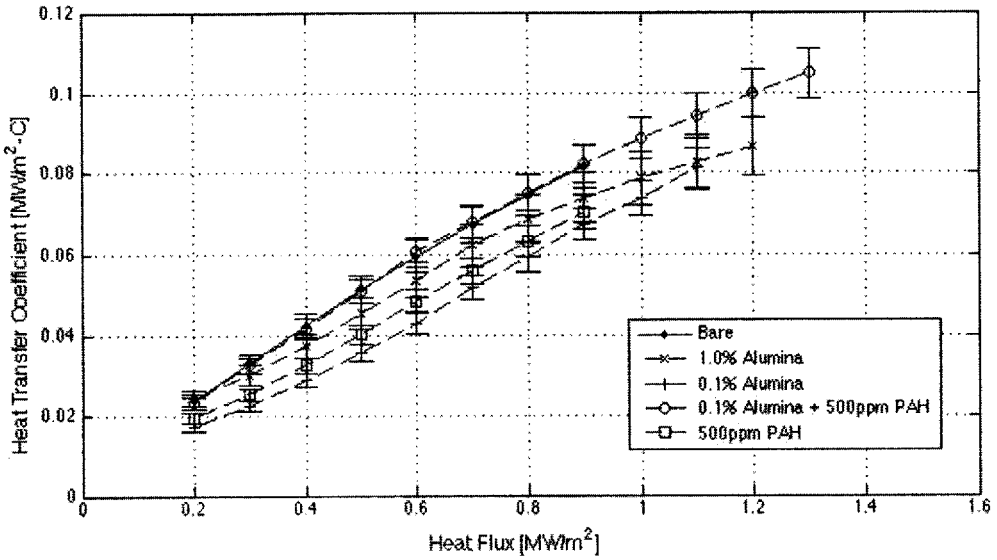

Figure A.2-1: Average heat transfer coefficient values for various wire coatings with experimental error bars.

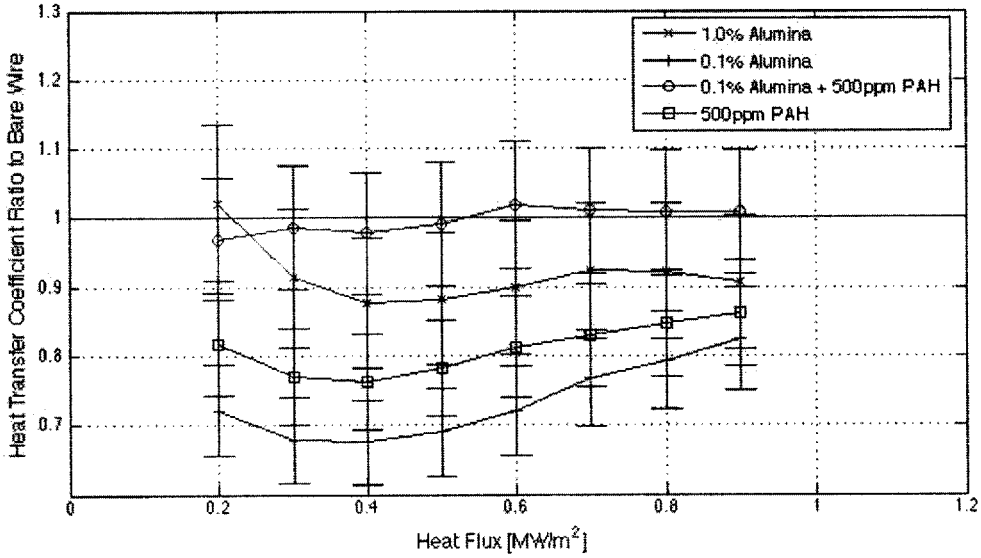

Figure A.2-2: Average HTC ratios to bare wire for various coatings with experimental error bars.

A.3 - Statistical Uncertainty

As mentioned previously, all error values included in error bars represented instrumentation error rather than statistical uncertainty. The initial measurement errors (Table A.1-1) were propagated through the calculations to CHF and HTC values using the methods explained above. The standard deviation of multiple measurements can be found with the following expression:

$$\sigma^2 = \frac{\sum_{i=0}^{n}\left(\left(x_i - x_{avg}\right)^2\right)}{n}, \tag{A-11}$$

with x_{avg} equal to the average value, x_i equal to the individual values included in the average, and n equal to the number of values taken into the average. The 95% confidence interval includes values in the range $x_{avg} \pm 1.69(\sigma/n^{1/2})$, which is calculated using the normal tables [39]. Table A-3.1 compares the experimental error and statistical uncertainty for the average CHF values. As can be seen in Table A.3-1, the statistical uncertainty for the average CHF values indicate that there is no significant difference in average CHF values between the different alumina-based coatings. To verify the statistical significance of the CHF enhancement of the various coatings, many more experiments would have to be conducted.

Table A.3-1: Experimental and statistical error for average CHF values.

Experiment	*Average CHF (MW/m^2)*	*Experimental Error (MW/m^2)*	*95% Confidence Interval (MW/m^2)*
Bare	1.046	0.077	0.143
1.0% alumina-pre-coated	1.329	0.051	0.143
0.1% alumina-pre-coated	1.429	0.036	0.135
Alumina + PAH-pre-coated	1.465	0.044	0.132
PAH-pre-coated	1.100	0.030	0.142

Appendix B- CHF and HTC Test Results

Wires that break at the solder typically experience CHF due to end effects rather than resistivity effects; therefore, only CHF values found for wires that broke near the wire center were considered valid [9]. End effects typically include bending or pinching near the solder point due to human error. At a bend or pinch in the wire, the cross-sectional area is different from the average wire cross-sectional area. Changes in the cross-sectional area can affect the heat flux at which CHF occurs compared to a perfectly straight/unbent wire.

Experimental results collected under subcooled conditions (i.e. water temperature was less than the saturation temperature) were also discarded because the focus of this study is saturated boiling CHF. When the bulk liquid is subcooled, the vapor bubbles can collapse even before leaving the heater surface [12, 13]. The heat flux therefore goes directly into heating the liquid, increasing CHF [12, 13]. In general, subcooled CHF is significantly higher than CHF that occurs under saturated conditions.

Experimental results used to calculate HTC were chosen based on the linearity of the HTC versus heat flux. HTC versus heat flux curves with significant deviations from linearity, either in the form of obvious curves or peaks, were not used in HTC calculations.

B.1 - Bare Wire

Results from all bare wire CHF experiments conducted before February 2009 were discarded due to experimental inconsistencies. Results from 10/17 and 10/24 were discarded because the wire broke at the solder in all of these tests. Results from 10/31 were discarded due to subcooled boiling.

Figure B.1-1 shows the boiling curve from the first deionized water experiment conducted on 10/17. This experiment was performed with the original lid assembly, which

required a wire length of 9.5 ± 0.5 cm. In this experiment, the wire broke at the solder. A CHF value of 0.978 ± 0.066 MW/m² was observed.

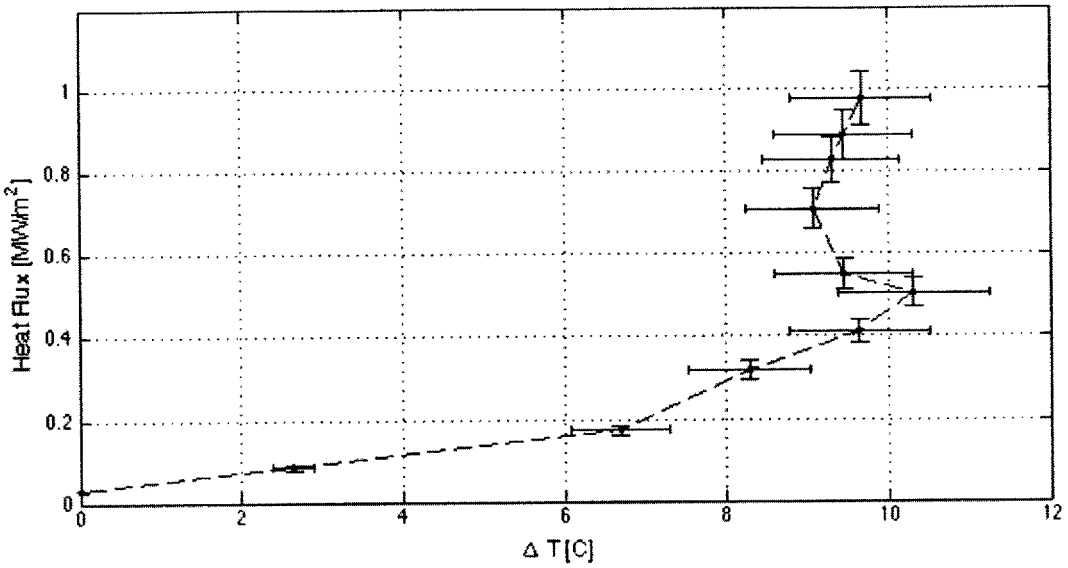

Figure B.1-1: Boiling curve for bare nickel wire in deionized water, 10/17 test 1. CHF occurred at 0.978 MW/m².

Figure B.1-2 shows the boiling curve from the second deionized water experiment conducted on 10/17. This and all subsequent experiments were performed with a new lid assembly, which required a wire length of 6.2 ± 0.5cm. In this experiment, the boiling vessel was insulated and the wire again broke at the solder. A CHF value of 0.745 ± 0.050 MW/m² was observed.

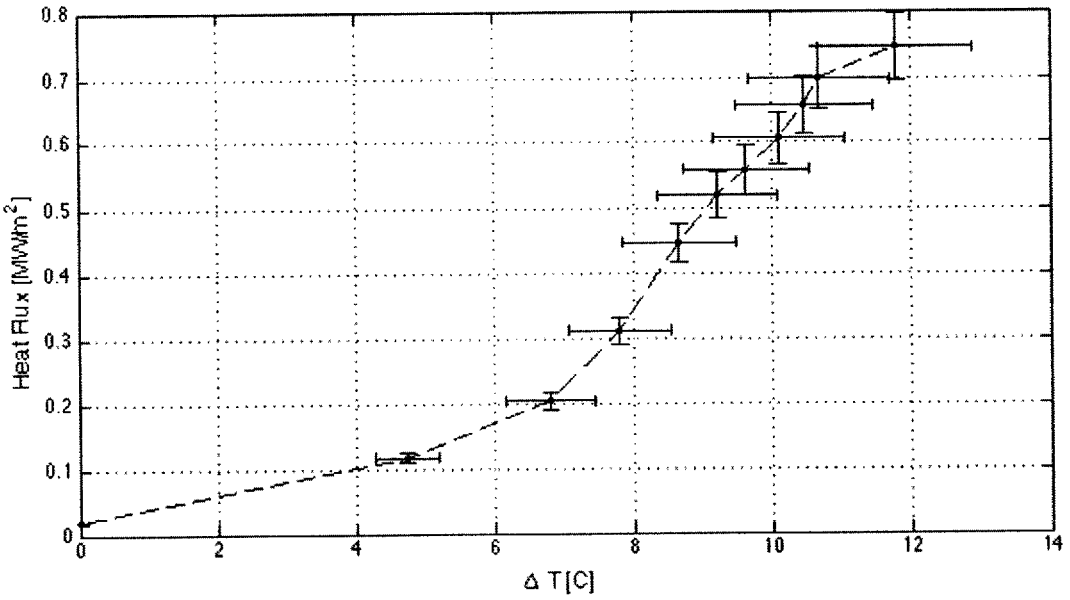

Figure B.1-2: Boiling curve for bare nickel wire in deionized water, 10/17 test 2. CHF occurred at 0.745 MW/m^2.

Figure B.1-3 shows the boiling curve from the deionized water experiment conducted on 10/24. In this experiment, the wire broke near the center. A CHF value of 0.759 ± 0.051 MW/m^2 was observed.

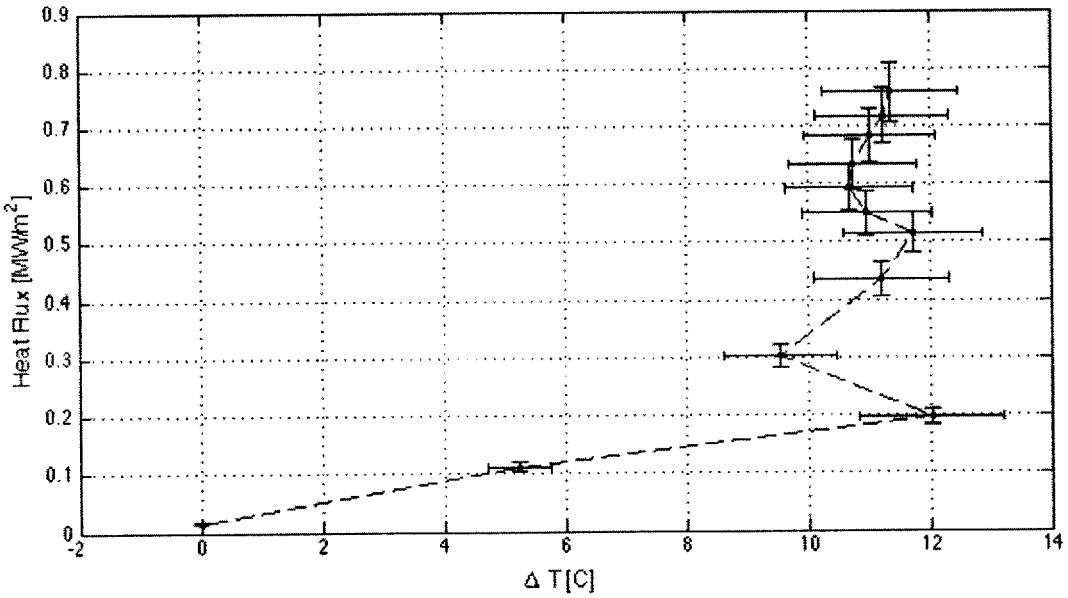

Figure B.1-3: Boiling curve for bare nickel wire in deionized water, 10/24 test 1. CHF occurred at 0.759 MW/m^2.

Figure B.1-4 shows the boiling curve from the deionized water experiment conducted on 10/24. In this experiment, the wire broke at the solder. A CHF value of 0.770 ± 0.052 MW/m^2

was observed.

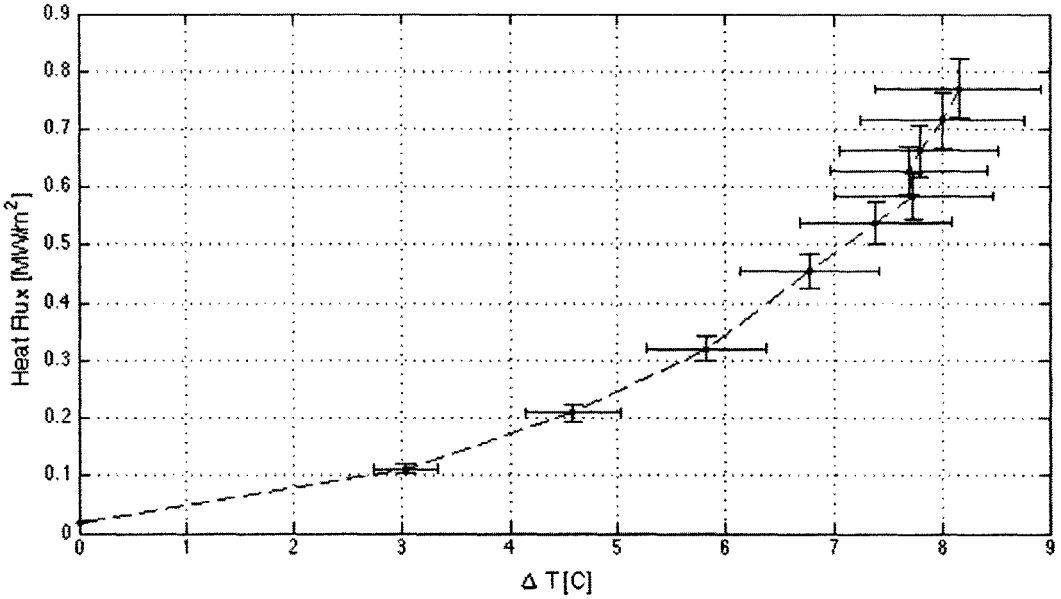

Figure B.1-4: Boiling curve for bare nickel wire in deionized water, 10/24 test 2. CHF occurred at 0.770 MW/m^2.

Figure B.1-5 shows the boiling curve from the deionized water experiment conducted on 10/27. In this experiment, the wire broke near the center. A CHF value of 0.810 ± 0.054 MW/m^2 was observed.

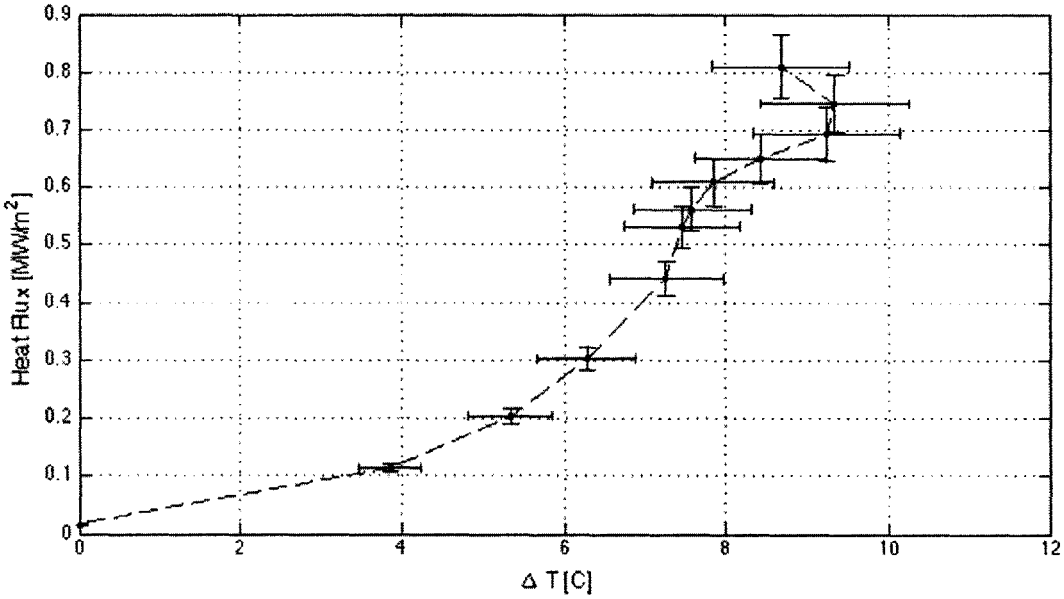

Figure B.1-5: Boiling curve for bare nickel wire in deionized water, 10/27 test 1. CHF occurred at 0.810 MW/m^2.

Figure B.1-6 shows the boiling curve from the deionized water experiment conducted on 10/29. In this experiment, the wire broke near the center. A CHF value of 0.726 ± 0.049 MW/m^2 was observed.

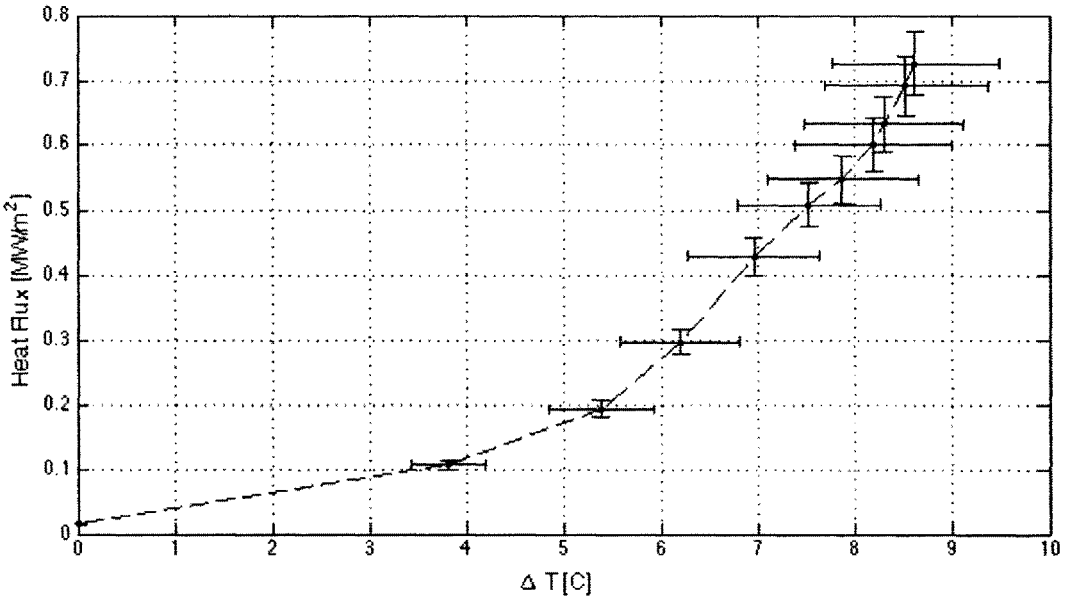

Figure B.1-6: Boiling curve for bare nickel wire in deionized water, 10/29 test 1. CHF occurred at 0.726 MW/m^2.

Figure B.1-7 shows the boiling curve from the deionized water experiment conducted on 10/31. In this experiment, the wire broke near the solder. A CHF value of 1.271 ± 0.085 MW/m^2 was observed. This experiment was started before the water reached saturation and took place under subcooled conditions, resulting in a higher CHF than in previous tests.

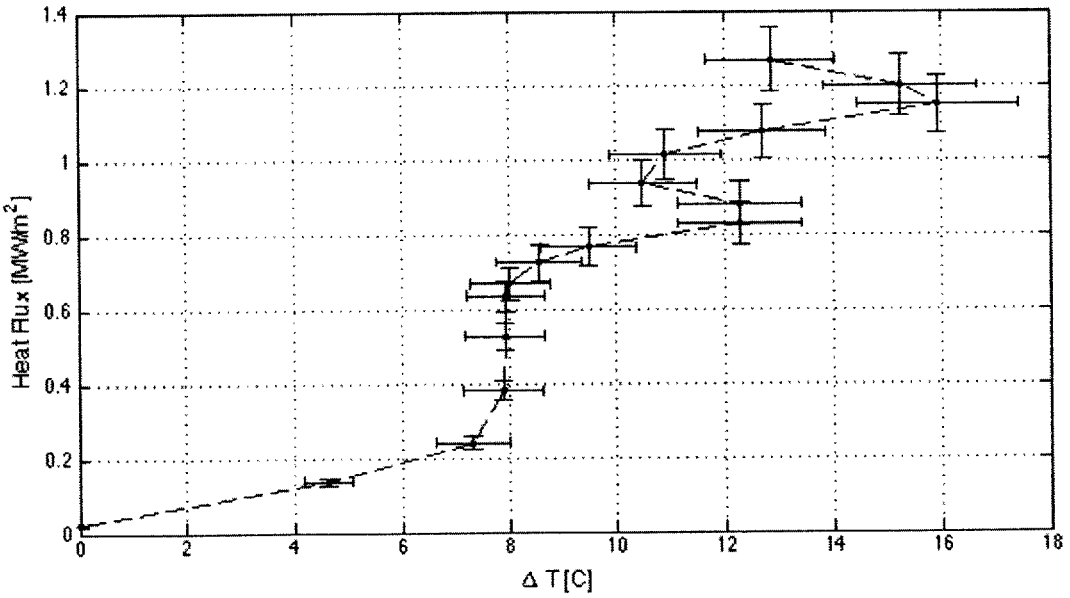

Figure B.1-7: Boiling curve for bare nickel wire in deionized water, 10/31 test 1. CHF occurred at 1.271 MW/m^2.

Figure B.1-8 shows the boiling curve from the deionized water experiment conducted on 01/30. In this experiment, the wire broke near the solder. A CHF value of 1.272 ± 0.085 MW/m^2 was observed.

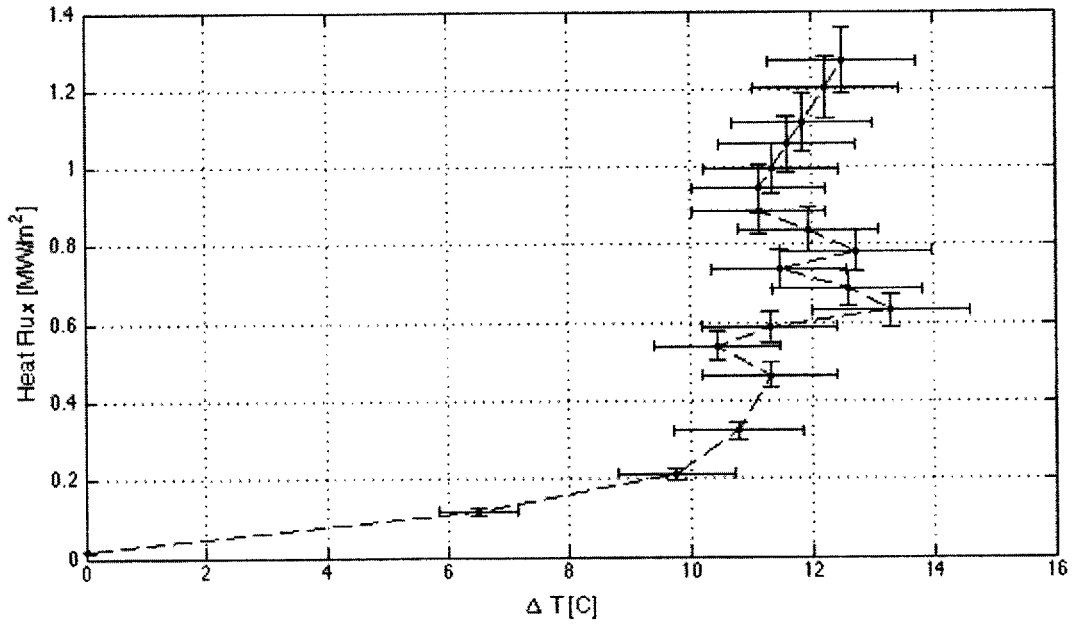

Figure B.1-8: Boiling curve for bare nickel wire in deionized water, 01/30 test 1. CHF occurred at 1.272 MW/m^2.

Experimental results obtained from the three tests conducted on 02/02 were consistent with each other and provided a solid baseline for comparison with pre-coated wires. For this reason, only the experimental results from 02/02 were used in determining bare wire CHF and HTC values. Figure B.1-1 illustrates the curves of the HTC values used in calculations with corresponding error bars. As can be seen, the HTC curves used are all within error range of the average values.

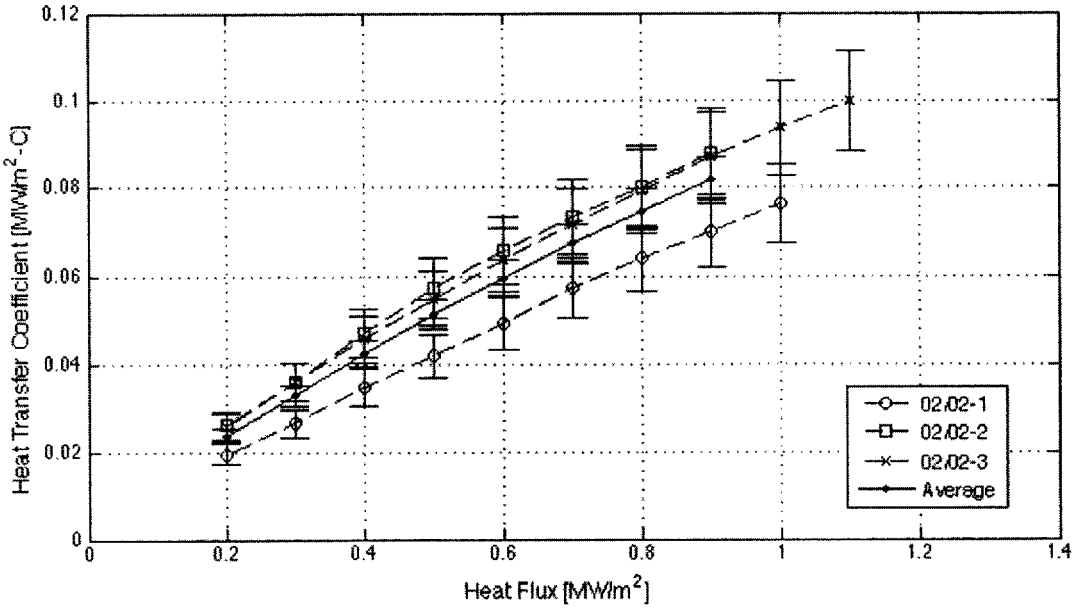

Figure B.1-9: Heat transfer coefficients versus heat flux for bare nickel wire in deionized water with corresponding error bars.

B.2 - 1.0% Alumina

Experimental results from 11/07 were omitted from Figure 31 and CHF calculations because of an error in the measurement instrumentation, which reported negative ΔT values. Experimental results from 11/13 and 01/06 were omitted from CHF calculations because the wire broke at the solder, indicating that CHF occurred due to end effects. The CHF value from 02/03 was omitted as an outlier, since all other CHF experiments yielded CHF values that were ~60% lower than the value of 2.115 MW/m^2 recorded on 02/03.

Figure B.2-1 shows the boiling curve from the alumina-pre-coated experiment conducted on 11/1. In this experiment, the wire broke near the solder. A CHF value of 1.573 ± 0.105 MW/m^2 was observed.

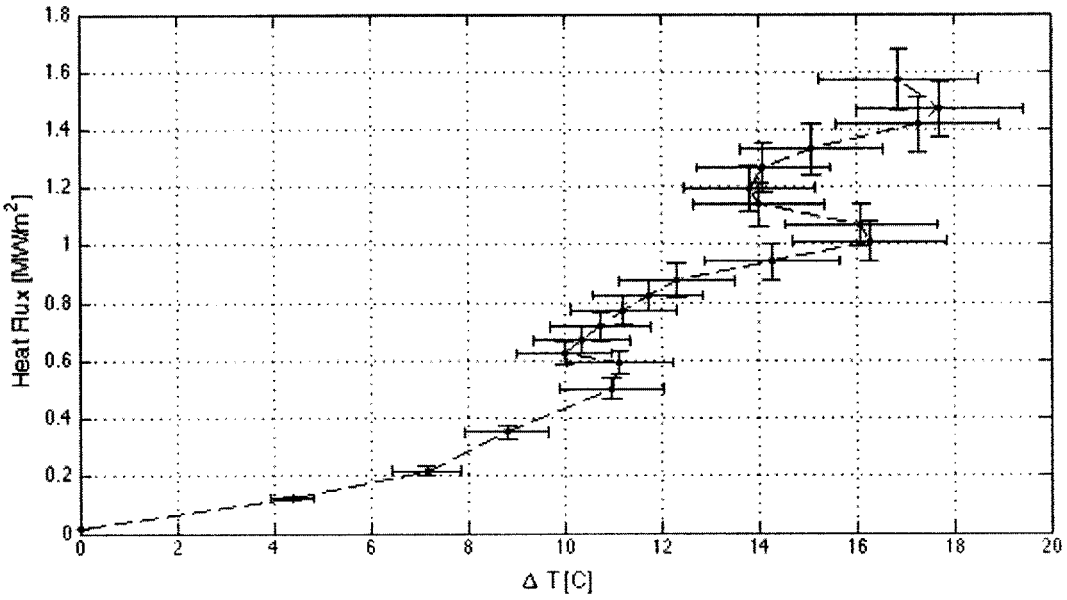

Figure B.2-1: Boiling curve for 1.0% alumina-pre-coated nickel wire in deionized water, 11/13 test 1. CHF occurred at 1.573 MW/m^2.

Figure B.2-2 shows the boiling curve from the alumina-pre-coated experiment conducted on 11/14. In this experiment, the wire radiated and broke at the solder. A CHF value of 1.474 ± 0.098 MW/m^2 was observed.

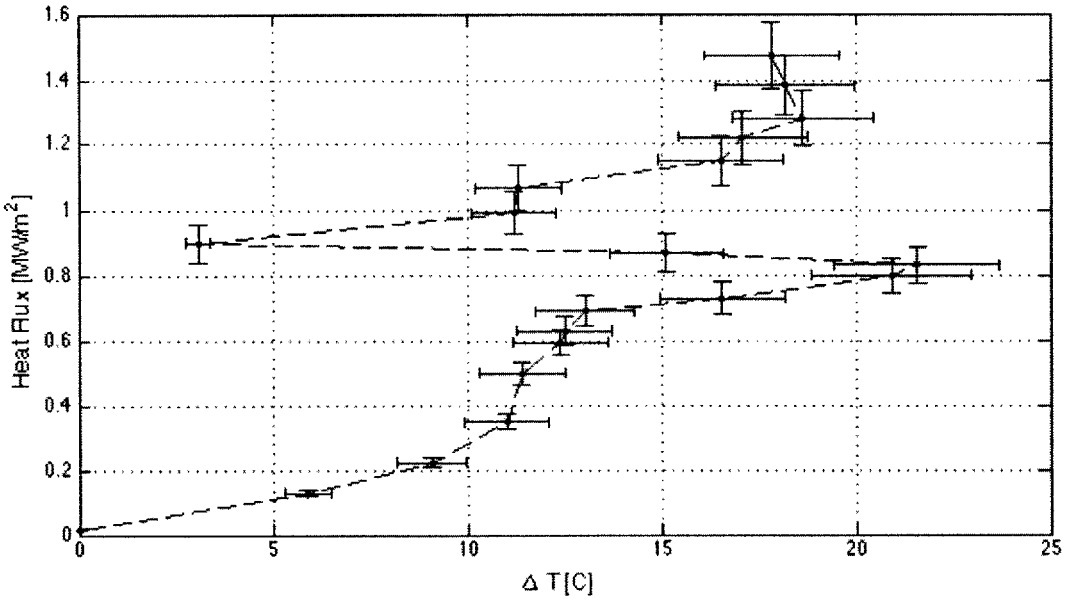

Figure B.2-2: Boiling curve for 1.0% alumina-pre-coated nickel wire in deionized water, 11/14 test 1. CHF occurred at 1.474 MW/m^2.

HTC analysis was conducted using data from 01/05 and 02/03. HTC curves from 11/13, 11/14, 11/18, and 01/06 exhibited deviations from linearity that can be seen in Figure B.2-3. Figure B.2-4 illustrates the curves of the HTC values used in calculations with corresponding error bars. As can be seen, the HTC curves used are all within error range of each other and the average values.

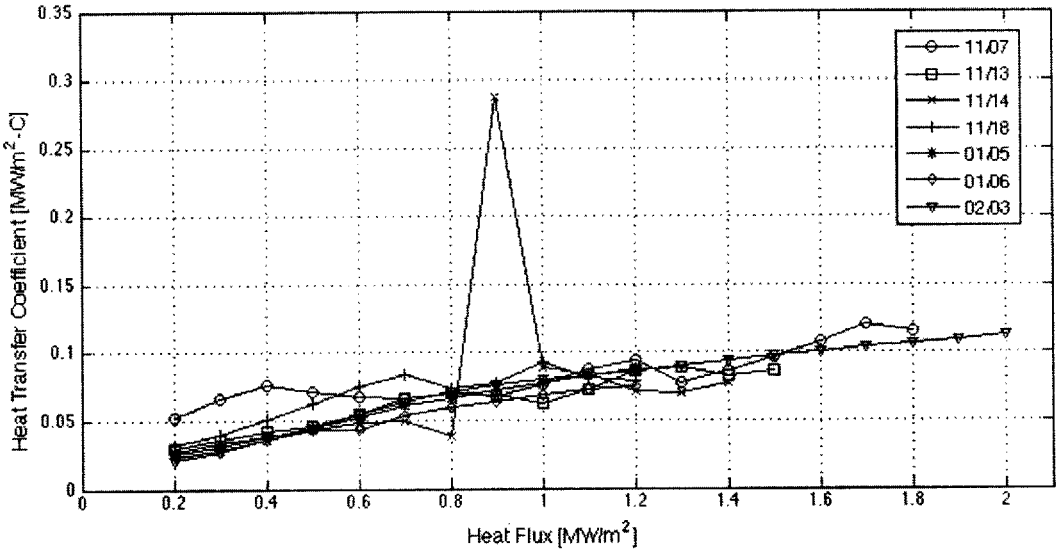

Figure B.2-3: Heat transfer coefficients versus heat flux for 1.0% alumina-pre-coated nickel wire in deionized water.

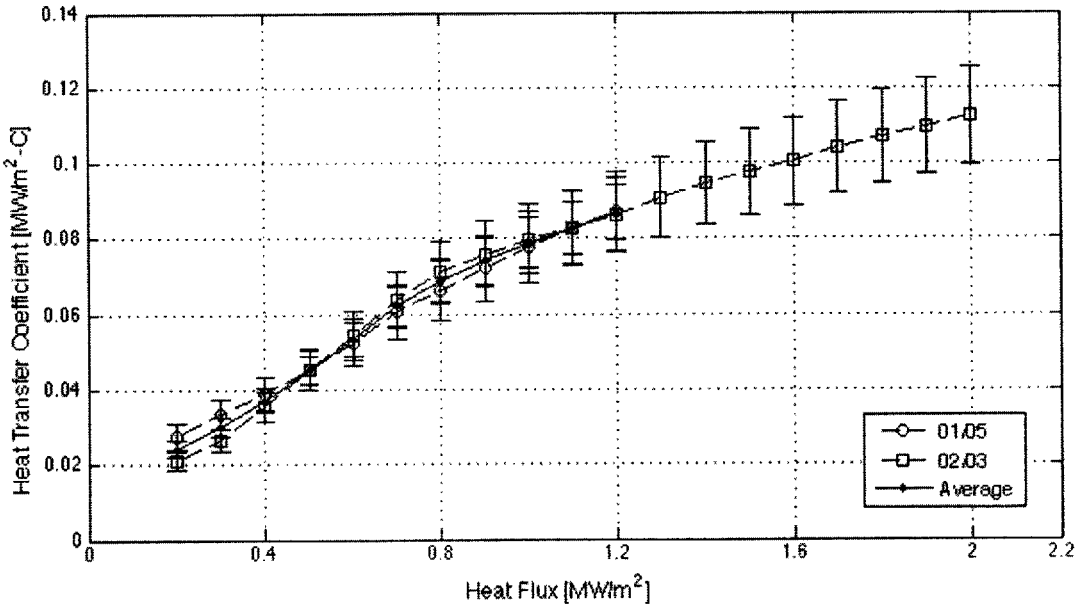

Figure B.2-4: Heat transfer coefficients versus heat flux for 1.0% alumina-pre-coated nickel wire in deionized water with corresponding error bars.

B.3 - 0.1% Alumina

HTC analysis was conducted using data from 02/05, 02/06-1, 02/09, and 02/10. HTC curves from 02/06-2, 02/11, and 02/13 exhibited deviations from linearity that can be seen in Figure B.3-1. Figure B.3-2 illustrates the curves of the HTC values used in calculations with corresponding error bars. As can be seen, the HTC curves used are all within error range of each

other and the average values.

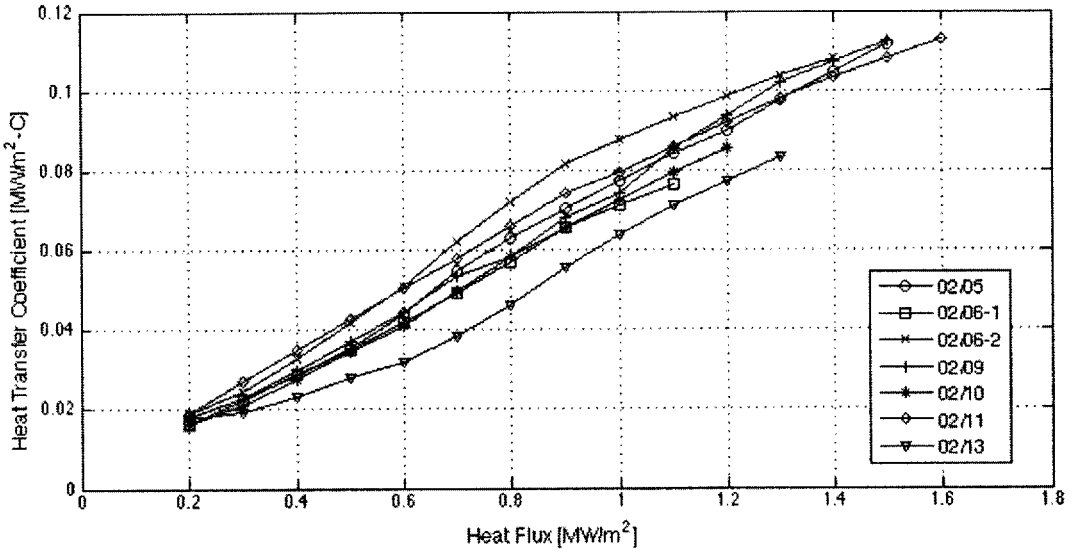

Figure B.3-1: Heat transfer coefficients versus heat flux for 0.1% alumina-pre-coated nickel wire in deionized water.

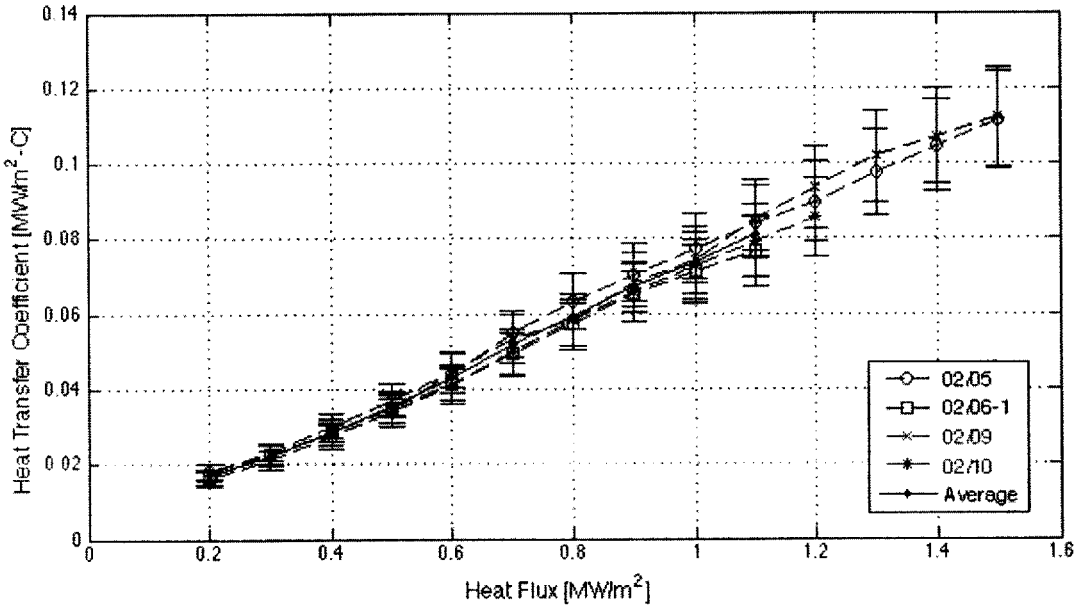

Figure B.3-2: Heat transfer coefficients versus heat flux for 0.1% alumina-pre-coated nickel wire in deionized water with corresponding error bars.

B.4 - Alumina + PAH

Experimental results from 01/08-2 were omitted from CHF calculations because the wire broke at the solder, indicating that CHF occurred due to end effects. HTC analysis was

conducted using data from 01/07, 01/08-2, 01/09, and 01/12. HTC curves from 01/08-1 and 01/14 exhibited deviations from linearity that can be seen in Figure B.4-1. Figure B.4-2 illustrates the curves of the HTC values used in calculations with corresponding error bars. As can be seen, the HTC curves used are all within error range of the average values.

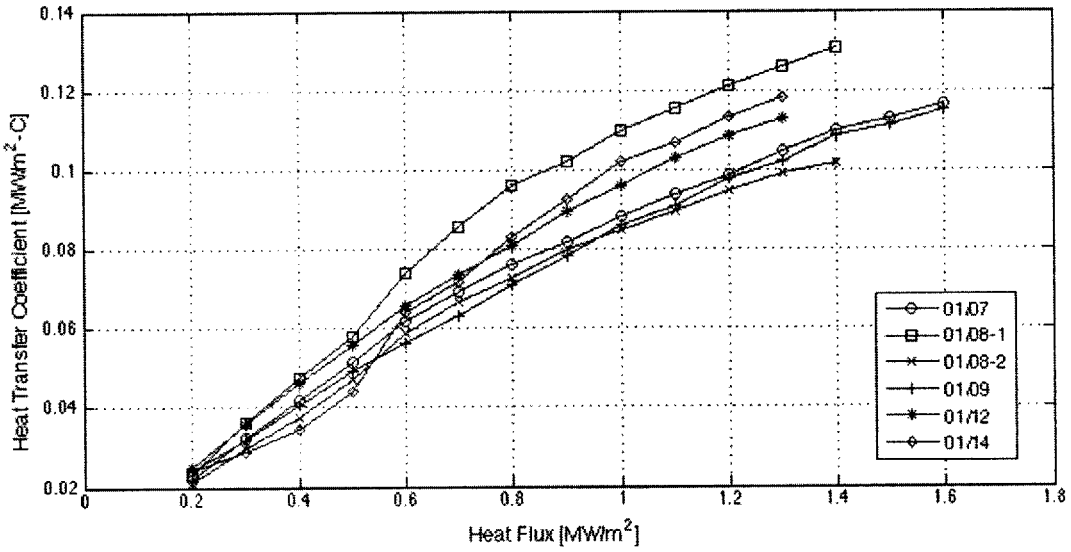

Figure B.4-1: Heat transfer coefficients versus heat flux for 0.1% alumina and 500ppm PAH-pre-coated nickel wire in deionized water.

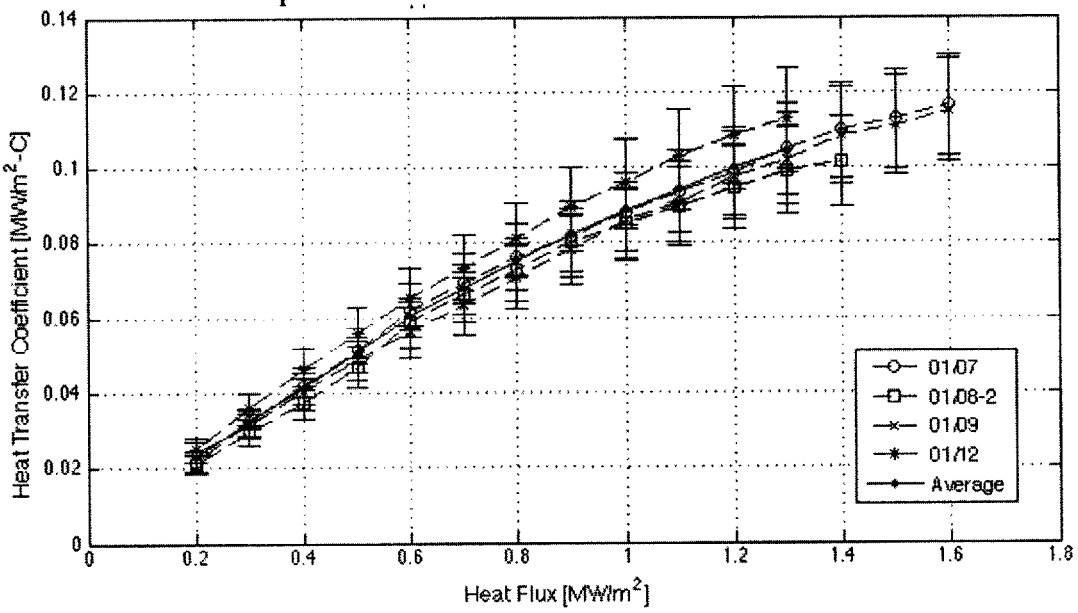

Figure B.4-2: Heat transfer coefficients versus heat flux for 0.1% alumina and 500ppm PAH-pre-coated nickel wire in deionized water with corresponding error bars.

B.5 - 500ppm PAH

Experimental results from 01/16, 01/20, and 01/22 test-2 were omitted from CHF calculations because the wire broke at the solder, indicating that CHF occurred due to end effects.

Figure B.5-1 shows the boiling curve from the first PAH-pre-coated wire experiment conducted on 01/16. In this experiment, the wire broke near the solder. A CHF value of 1.120 ± 0.075 MW/m^2 was observed.

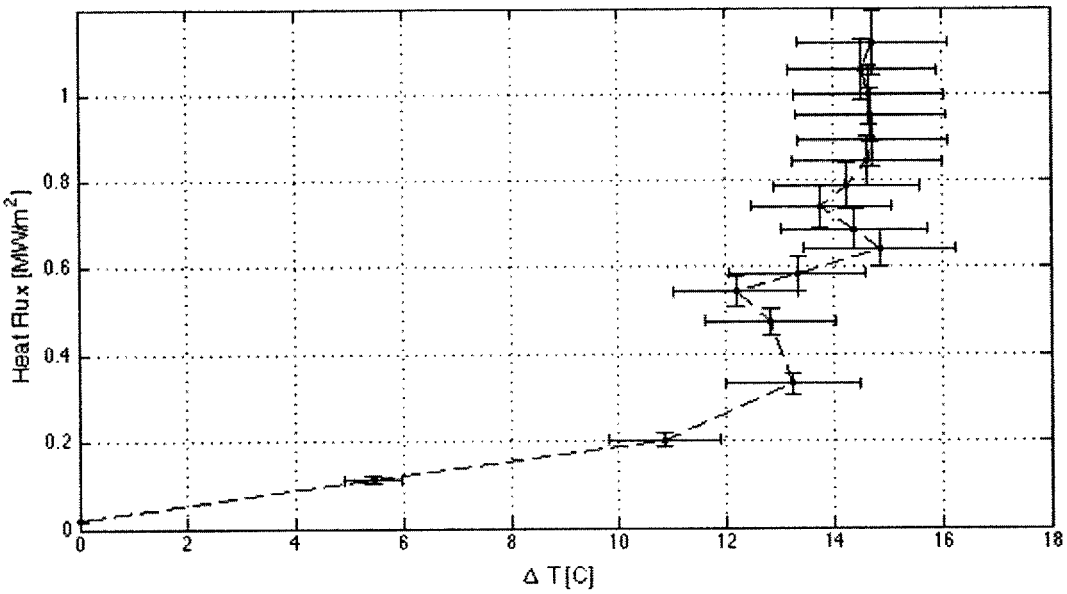

Figure B.5-1: Boiling curve for PAH-pre-coated nickel wire in deionized water, 01/16 test 1. CHF occurred at 1.120 MW/m^2.

Figure B.5-2 shows the boiling curve from the second PAH-pre-coated wire experiment conducted on 01/16. In this experiment, the wire broke near the solder. A CHF value of 0.972 ± 0.065 MW/m^2 was observed.

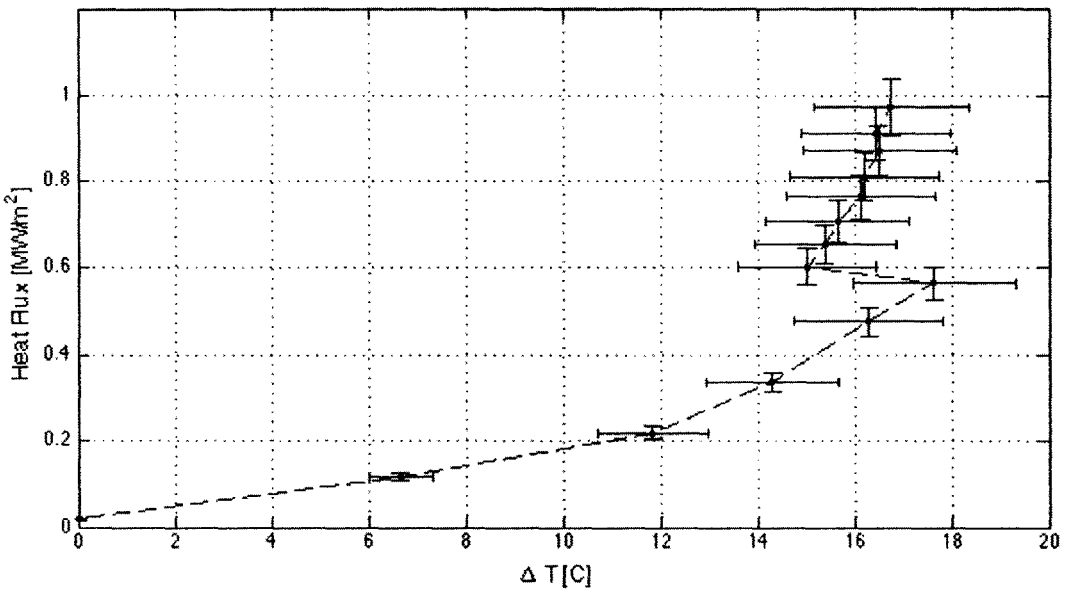

Figure B.5-2: Boiling curve for PAH-pre-coated nickel wire in deionized water, 01/16 test 2. CHF occurred at 0.972 MW/m^2.

HTC analysis was conducted using data from 01/20, 01/22, and 02/19. HTC curves from 01/16, 01/23, 02/24, and 03/03 exhibited deviations from linearity that can be seen in Figure B.5-3. Figure B.5-4 illustrates the curves of the HTC values used in calculations with corresponding error bars. As can be seen, the HTC curves used are all within error range of each other and the average values.

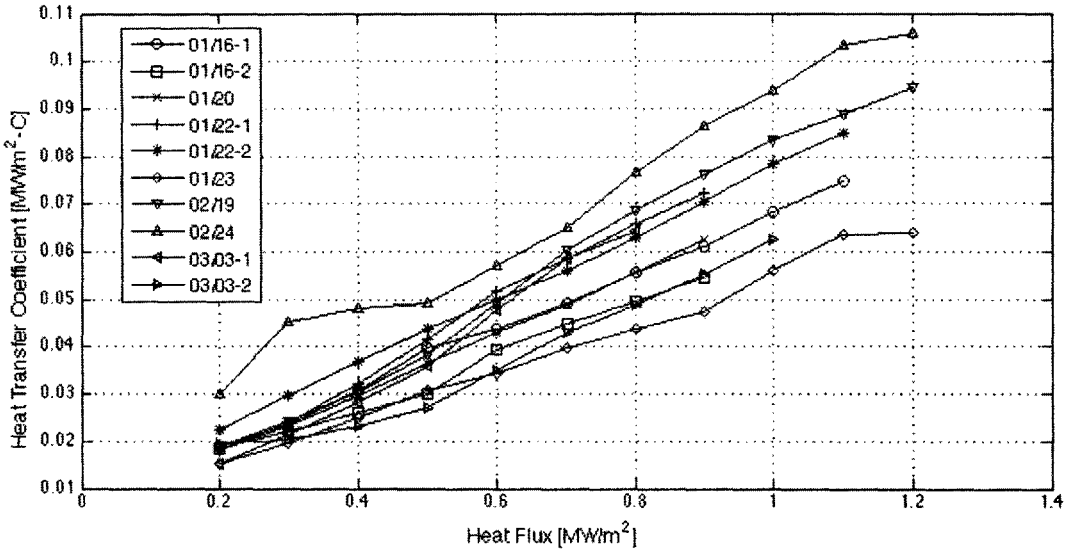

Figure B.5-3: Heat transfer coefficients versus heat flux for 500ppm PAH-pre-coated nickel wire in deionized water.

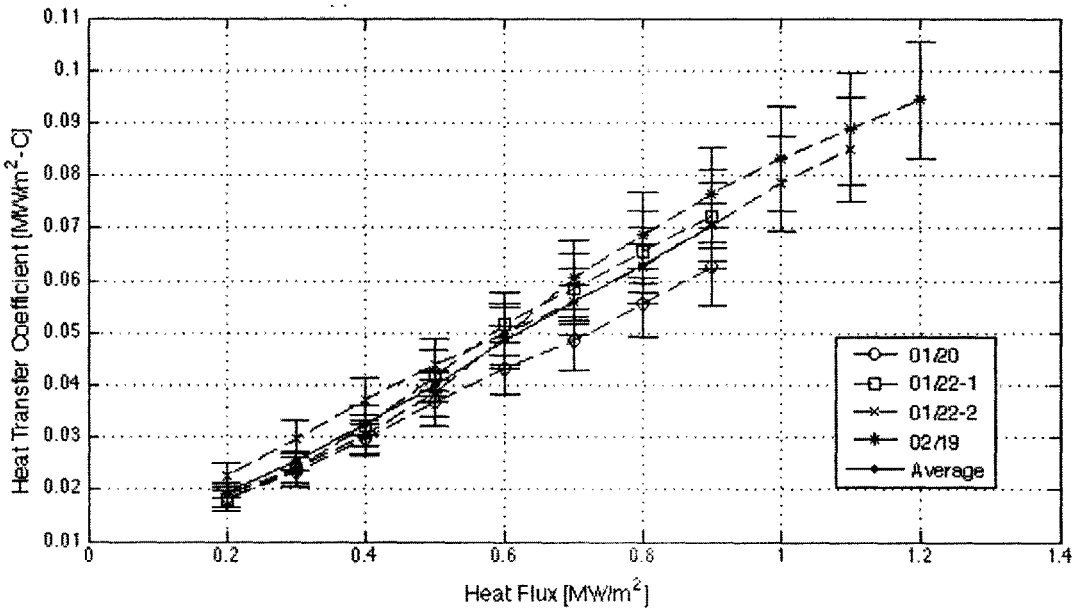

Figure B.5-4: Heat transfer coefficients versus heat flux for 500ppm PAH-pre-coated nickel wire in deionized water with corresponding error bars.

7 References

[1] B. Truong, L. W. Hu, J. Buongiorno, "Surface Modifications Using Nanofluids for Nucleate Boiling Heat Transfer and CHF Enhancements", *Proceedings of the Sixth International ASME Conference on Nanochannels, Microchannels and Minichannels*, 2008.

[2] J. Buongiorno, L. W. Hu, S. J. Kim, R. Hannink,B. Truong, E. Forrest, "Nanofluids for Enhanced Economics and Safety of Nuclear Reactors: An Evaluation of the Potential Features, Issues, and Research Gaps", *Nuclear Technology*, Vol. 162, 80-91, April 2008.

[3] X. Q. Wang, A. S. Mujumdar, "Heat transfer characteristics of nanofluids: a review", *International Journal of Thermal Sciences*, 2006.

[4] S. G. Kandlikar, "A Theoretical Model to Predict Pool Boiling CHF Incorporating Effects of Contact Angle and Orientation", *Journal of Heat Transfer*, Vol. 123, 1071-1079, 2001.

[5] S. J. Kim, I. C. Bang, J. Buongiorno, L. W. Hu, "Surface wettability change during pool boiling of nanofluids and its effect on critical heat flux", *International Journal of Heat and Mass Transfer*, Vol. 50, 4105-4116, 2007.

[6] B. G. Prevo, E. W. Hon, O. D. Velev, "Assembly and characterization of colloid-based antireflective coatings on multicrystalline silicon solar cells", *Journal of Materials Chemistry*, Vol. 17, 791-799, 2007.

[7] R. J. Klein, P. M. Biesheuvel, B. C. Yu, C. D. Meinhart, F. F. Lange, "Producing Super-Hydrophobic Surfaces with Nano-Silica Spheres", UCSB Microfluidics Laboratory, 2004.

[8] L. W. Hu, personal communication, 3 October 2008.

[9] B. Truong, personal communication, 24 October 2008.

[10] E. Forrest, personal communication, 23 October 2008.

[11] M.F. V. Silva, P. Hancock, J. R. Nicholls, "An Improved Three-Point Bending Method by Nanoindentation", *Surface & Coatings Technology*, Vol. 169, 748-752, 2003.

[12] J. J Lienhard IV, J. H. V. Lienhard, "A Heat Transfer Textbook: Third Edition", Phlogiston Press, Cambridge, 2008.

[13] N. E. Todreas, M. S. Kazimi, "Nuclear Systems I: Thermal Hydraulic Fundamentals",

Taylor & Francis Group, New York, 1990.

[14] M. Boustie, L. Berthe, T. de Ressegnier, M. Arrigoni, "Laser Shock Waves: Fundamentals and Applications", *1st Symposium on Laser Ultrasonics: Science, Technology, and Applications*, Montreal, 2008.

[15] R. Jacobs, J. Meneve, G. Dyson, D. G. Teer, N. M. Jennett, P. Harris, J. von Stebut, C. Comte, P. Feuchter, A. Cavaleiro, H. Ronkainen, K. Holmberg, U. BEck, G. Reiners, C. D. Ingelbrecht, "A Certified Reference Material for the Scratch Test", *Surface & Coatings Technology*, Vol. 174, 1008-1013, 2003.

[16] C. Bolis, L. Berthe, M. Boustie, M. Arrigoni, S. Barradas, M. Jeandin, "Physical Approach to Adhesion Testing Using Laser-Driven Shock Waves", *Journal of Physics D: Applied Physics*, Vol. 40, 3155-3163, 2007.

[17] Y. Xie, H. M. Hawthorne, "A Model for Compressive Coating Stresses in the Scratch Adhesion Test", *Surface & Coatings Technology*, Vol. 141, 15-25, 2001.

[18] A. V. Fedenev, S. B. Aleksheev, I. M. Goncharenko, N. N. Koval, E. I. Lipatov, V. M. Orlovskii, V. F. Tarasenko, M. A. Shulepov, "Laser Test of Adhesion of Thin Metal Films on Glass Substrate", *IEEE*, 2003.

[19] K. L. Mittal, ed., *Adhesion Measurement of Films and Coatings*, Vol. 2, VSP, 2001.

[20] D. Horkavcova, "Measurement of Adhesion of the Coating to Ti Substrates", Department of Glass and Ceramics, Institute of Chemical Technology, Prague, 2008.

[21] D. S. Rickerby, "A Review of the Methods for the Measurement of Coating-Substrate Adhesion", *Surface and Coatings Technology*, Vol. 36, 541-557, 1988.

[22] L. Wolf, M. S. Kazimi, N. E. Todreas, Note L.4: Introduction to Structural Mechanics, 2001.

[23] B. J. Skutnik, "New Silica Optical Fibers with Nano Porous Silica Cladding/ Coating", *Optical Fiber and Fiber Component Mechanical Reliability and Testing*, Proceedings of SPIE, Vol. 4215, 2001.

[24] R. Chen, M. C. Lu, V. Srinivasan, Z. Wang, H. H. Cho, A. Majumdar, "Nanowires for Enhanced Boiling Heat Transfer", *Nano Letters*, 2008.

[25] "Standard Test Methods for Mandrel Bend Test of Attached Organic Coatings", ASTM, 2001.

[26] H. Nagata, N. Mitsugi, "Failure Case Study for Optical Fiber Breaks in Metal Packages", *Optical Fiber Technology*, Vol. 5, 338-348, 1999.

[27] S. Kawabata, Y. Yamashita, A. Kido, K. Ueda, "Fatigue of Fiber Caused by Repeated Axial Compression", University of Shiga Prefecture.

[28] T. Ando, K. Kizu, Y. M. Miura, K. Tsuchiya, M. Matsukawa, H. Tamai, S. Ishida, N. Koizumi, K. Okuno, "Effective bending strain estimated from Ic test results of a D-shaped Nb3Al CICC coil fabricated with a react-and-wind process for the National Centralized Tokamak", *Fusion Engineering and Design*, Vol. 75-79, 99-103, 2005.

[29] S. G. Liter, M. Kaviany, "Pool-boiling CHF enhancement by modulated porous-layer coating: theory and experiment", *International Journal of Heat and Mass Transfer*, Vol. 44, 4287-4311, 2001.

[30] J. E. Shigley, C. R. Mischke, "Mechanical Engineering Design: 5th Edition", McGraw-Hill, Inc., New York, 1989.

[31] MatWeb: Material Property Data, Automation Creations, Inc., retrieved on 2/20/09 from: matweb.com.

[32] C. Li, G. P. Peterson, "Experimental Studies on CHF of Pool Boiling on Horizontal Conductive Micro Porous Coated Surfaces", *Space Technology and Applications International Forum*, American Institute of Physics, 2008.

[33] M. S. Sarwar, Y. H. Jeong, S. H. Chang, „Subcooled flow boiling CHF enhancement with porous surface coatings", *International Journal of Heat and Mass Transfer*, Vol. 50, 3649-3657, 2007.

[34] P. A. B. de Sampaio, J. L. H. Faccini, J. Su, "Modelling of stratified gas-liquid two-phase flow in horizontal circular pipes", *International Journal of Heat and Mass Transfer*, Vol. 51, 2752-2761, 2008.

[35] S. Wongwises, A. Pornsee, E. Siroratsakul, "Gas-Wall Shear Stress Distribution in Horizontal Statified Two-Phase Flow", *International Communications in Heat and Mass Transfer*, Vol. 26, No. 6, 849-860, 1999.

[36] J. S. Ahn, P. T. Hammond, M. F. Rubner, I. Lee, "Self-assembled particle monolayers on polyelectrolyte multilayers: particle size effects on formation, structure, and optical properties", *Colloids and Surfaces A: Physicochemical and Engineering Aspects*, Vol. 259, Issues 1-3, 45-53, May 2005.

[37] B. Truong, "Critical Heat Flux Enhancement via Surface Modification Using Colloidal Dispersions of Nanoparticles (Nanofluids)", Master Thesis, Nuclear Science and Engineering Department at the Massachusetts Institute of Technology, Cambridge, MA, May 2008.

[38] S. J. Kim, "Subcooled Flow Boiling Heat Transfer and Critical Heat Flux in Water-Based Nanofluids at Low Pressure," PhD Thesis, Nuclear Science and Engineering Department at the Massachusetts Institute of Technology, Cambridge, MA, June 2009.

[39] A. H-S. Ang, W. H. Tang, "Probability Concepts in Engineering: Emphasis on Applications in Civil and Environmental Engineering 2nd Edition", John Wiley & Sons, Inc., Massachusetts, 2007.

[40] E. Dörre, H. Hübner, "Alumina: Processing, Properties, and Applications", Springer-Verlag, New York, 1984.

[41] O. Mermut, J. Lefebvre, D. G. Gray, C. J. Barrett, "Structural and Mechanicals Properties of Polyelectrolyte Multilayer Films Studied by AFM", *Macromolecules*, Vol. 36, 8819-8824, 2003.

[42] V. V. Lulevich, D. Andrienko, O. I. Vinogradova, "Elasticity of polyelectrolyte multilayer microcapsules", *Journal of Chemical Physics*, Vol. 120, No. 8, 3822-3826, 2004.

[43] O. V. Lebedeva, B. S. Kim, K. Vasilev, O. I. Vinogradova, "Salt softening of polyelectrolyte multilayer microcapsules", *Journal of Colloid and Interface Science*, Vol. 284, 455-462, 2004.

[44] D. Collin, P. Lavalle, J. M. Garza, J. C. Voegel, P. Schaaf, P. Martinoty, "Mechanical Properties of Cross-Linked Hyaluronic Acid/Poly-(l-lysine) Multilayer Films", *Macromolecules*, Vol. 37, No. 26, 10195-10198. 2004.

[45] C. Jiang, S. Markutsya, V. V. Tsukruk, "Compliant, Robust, and Truly Nanoscale Free-Standing Multilayer Films Fabricated Using Spin-Assisted Layer-by-Layer Assembly", *Advanced Materials*, Vol. 16, No. 2, 157-161, 2004.

[46] ASTM D3359 – 08 Standard Test Methods for Measuring Adhesion by Tape Test, Book of Standards, Vol. 06.01, ASTM International, retrieved on 5/01/09 from: http://www.astm.org/Standards/D3359.htm.